PITCHING MOMENT PREDICTIONS ON WIND TURBINE BLADES USING THE BEDDOES-LEISHMAN MODEL FOR UNSTEADY AERODYNAMICS AND DYNAMIC STALL

by

Jeffrey Edward Minnema

A thesis submitted to the faculty of
The Universtiy of Utah
in partial fulfillment of the requirements for the degree of

Master of Science

Department of Mechanical Engineering

The University of Utah

June 1998

THE UNIVERSITY OF UTAH GRADUATE SCHOOL

SUPERVISORY COMMITTEE APPROVAL

of a thesis submitted by

Jeffrey Edward Minnema

This thesis has been read by each member of the following supervisory committee and by majority vote has been found to be satisfactory.

5/26/98 — Chair: A. Craig Hansen

26 May 98 — James K. Strozier

5/26/98 — William K. Van Moorhem

THE UNIVERSITY OF UTAH GRADUATE SCHOOL

FINAL READING APPROVAL

To the Graduate Council of the University of Utah:

I have read the thesis of Jeffrey Edward Minnema in its final form and have found that (1) its format, citations and bibliographic style are consistent and acceptable; (2) its illustrative materials including figures, tables and charts are in place; and (3) the final manuscript is satisfactory to the supervisory committee and is ready for submission to The Graduate School.

5/27/38
Date

A. Craig Hansen
Chair: Supervisory Committee

Approved for the Major Department

Robert B. Roemer
Chair/Dean

Approved for the Graduate Council

Ann W. Hart
Dean of The Graduate School

ABSTRACT

The Beddoes-Leishman model (with some modifications) for predicting pitching moment coefficients on airfoils operating under dynamic conditions has been added to the AeroDyn subroutines. These subroutines are used to determine aerodynamic loads on wind turbine blades in the ADAMS, YawDyn and DynStall computer programs, which model wind turbines and aid in their design.

This thesis explains the usefulness of pitching moment calculations for wind turbine blades, the methods used to calculate them and compares simulated pitching moment coefficients to test data for different airfoils under various operating conditions. Finally, torsional springs of various stiffnesses were added to an ADAMS model to investigate the effect of aerodynamic pitching moment on angle of attack, pitch angle, power and flap moment.

The implemented model predicted pitching moments with reasonable accuracy for all of the conditions that were investigated and is appropriate for use in the AeroDyn subroutines.

TABLE OF CONTENTS

ABSTRACT iv

LIST OF SYMBOLS vii

ACKNOWLEDGEMENTS x

INTRODUCTION 1

History 1
Benefits of Wind Energy 2
The Future of Wind Energy 3
Computer Modeling 3
Dynamic Stall 5
Pitching Moments 6
Goals 12

METHODS 14

The Method for Determining Pitching Moments 14
C_{MI} and C_{MQ} 15
C_{MF} 18
Calculating the trailing edge separation point 18
Using the dynamic angle of attack to locate C_{MF} 20
C_{MV} 22
C_M 23
Static Airfoil Table Requirements 27
Determining Drag Coefficients 28
Extending the Range of C_M, C_L, and C_D Values 29
Determining $C_{n\text{-}stall}$ 34

TIME CONSTANT RESULTS 43

T_p and T_f 44
T_α 44
T_v 48
T_{vl} 48

TWO-DIMENSIONAL WIND TUNNEL DATA SIMULATION RESULTS 51

NACA 4415 Airfoil 53
NASA LS(1)-0417 Airfoil 63
NREL S809 Airfoil 72

COMBINED EXPERIMENT ROTOR DATA COMPARISON RESULTS.....80

Conclusion 89

ADAMS MODEL OF THE CER WITH PITCHING DEGREE OF FREEDOM RESULTS 94

CONCLUSION.....105

Topics for Future Work 106

APPENDICES

A: DYNSTALL COMPUTER PROGRAM.....108

B: SAMPLE AIRFOIL FILE.....132

C: 2-D WIND TUNNEL SIMULATIONS WITH Re OF 1.5 MILLION.....135

D: YAWDYN.IPT FILE.....147

REFERENCES 149

LIST OF SYMBOLS

a	Induction factor
A	Planform area
APRP	Adjusted value of PRP
c	Chord length
C_D	Drag coefficient
C_L	Lift coefficient
C_{Lmax}	Maximum lift coefficient
C_M	Pitching moment coefficient
C_{MF}	Non-linear moment force coefficient which is associated with trailing edge flow separation
C_{MI}	Impulsive pitching moment coefficient due to a step change in angle of incidence
C_{MQ}	Impulsive pitching moment coefficient due to a step change in pitching rate
C_{MV}	Vortex induced pitching moment coefficient
C_N	Normal force coefficient
C_{NI}	Impulsive normal force coefficient due to a change in the angle of incidence
C_{NQ}	Impulsive normal force coefficient due to a change in pitching rate
C'_N	First order lagged normal force coefficient
$C_{n\text{-}stall}$	Normal force coefficient at stall
$C_{N\alpha}$	Normal force curve slope at zero C_N

CP_v	Vortex induced center of pressure
C^v_N	Vortex induced normal force coefficient
D_{fn}	Deficiency function
$D_{\alpha n}$	Deficiency function
f	Trailing edge separation point
f'	Modified separation point
f''	Final unsteady trailing edge separation point
I	Area moment of inertia
k	Reduced frequency
K_n	Coefficients for pitching moment curve fits
K_I	Time constant = 0.75
k_s	Spring constant
M	Mach number
M	Pitching moment
p	per rotor revolution
PRP	Reduced time rate of change of angle of attack
R	Radius
Re	Reynold's number
S	Distance in semi-chords
t	Time
$\hat{t}$	Nondimensionalized time
T_f	Time constant of first order lag applied to motion of the separation point

T_p	Time constant for first order lag in pressure due to unsteady flow
T_v	Time constant that governs the strength of the dynamic stall vortex
T_{vl}	Nondimensional time of transit for the vortex moving across the airfoil surface
T_α	Time constant used to find α''
V	Local wind velocity
x	Distance from the leading edge to the point of flow separation
α	Angle of attack
α'	Effective angle of attack
α''	Dynamic angle of attack
α_{stall}	Stall angle of attack
ρ	Air density
τ_v	Nondimensional position of dynamic stall vortex
ω	Oscillation frequency or angular velocity
ω_n	Natural frequency

ACKNOWLEDGEMENTS

The National Renewable Energy Laboratory (NREL) sponsored this work. I would like to thank my advisor, Dr. Craig Hansen for all of his guidance, technical knowledge, even temperament and patience throughout this research. I am also very grateful to Kirk Pierce, Dave Laino, Dean Davis, Dr. Strozier and Dr. Van Moorhem for the time and expertise they have contributed to this work. Finally, I would like to thank my best friend, Julia Batten, for the love, understanding and assistance she has provided.

INTRODUCTION

History

Windmills have been used in the United States for more than a century (Spera, 1994). Examples of early windmill technology in the United States include the "American Windmill" and a windmill erected by inventor Charles Brush. The "American Windmill" was a five-meter diameter mill, capable of producing approximately one horsepower in a 7 m/s wind; enough to support most of a farms' water pumping needs. In 1888, inventor Charles Brush erected the first windmill to generate electricity. This windmill had a 17-meter diameter, high solidity rotor with a rated power output of 12 kW.

Significant advancements in windmill technology, however, did not occur until the 1970's (Gipe, 1995). Between 1973 and 1978 there was a dramatic rise in the price of oil. These increases, in addition to concerns about over-reliance on fossil fuels and the need to reduce carbon-dioxide (CO_2) emissions, renewed interest in alternative energy sources, in particular, wind energy.

At present, the most popular designs are two- or three-bladed, horizontal axis wind turbines. These modern machines vary in power production from a few watts to over three megawatts.

Benefits of Wind Energy

Wind energy is an ideal source of electricity for several reasons. First, wind energy produces virtually no CO_2 emissions (San Martin, 1989). Second, wind energy is cost-competitive in some markets. The cost of wind generated electricity has dropped sharply since 1980, when it cost $0.35 per kW-hr (Acona et al., 1996). Today wind generated electricity costs less than $0.05 per kW-hr. Thus, today's cost is already competitive with some conventional energy sources and will become even less expensive as wind power technology advances. Third, wind energy offers other economic benefits that make it more competitive in the long term including less dependence on fossil fuels and greatly reduced environmental impact.

Finally, wind power has diverse applications including:

- Remote power generation. Where there are no power lines present or the cost of running power lines is too expensive (Note: It costs approximately $90,000 per mile to run a power line in Southern California) a wind turbine can supply power. Often times wind turbines are combined with solar panels and diesel generators to form a hybrid system.
- Wind farm applications that connect many wind turbines together to form a power plant such as the Buffalo Ridge site in southwestern Minnesota. Northern States Power Company operates this wind farm which contains over 70 Kenetech 33-MVS (250 kW) wind turbines.
- Supplemental power uses such as in Traverse City, Michigan which recently installed a Vestas 600-kilowatt wind turbine in order to keep up with its need for more electrical energy. Some growing communities are using wind power

as an alternative to other energy sources such as coal or natural gas. They find it to be a cleaner solution to their escalating energy needs.

The Future of Wind Energy

Although wind energy has many economic advantages and diverse applications, the rest of the world is currently installing wind power at a much faster rate than the United States (US) (Ancona et al., 1996). The US had 36% of the world's total installed wind power capacity of 4900 megawatts at the end of 1995. This is a significant reduction from the US's 50% stake posted in 1994 and its 90% share in 1988. Europe had 2500 MW of installed wind capacity at the end of 1995. This is nearly three times its capacity in 1992. World wide, wind power has a bright future.

Wind power capacity is growing at an average annual rate of 20%. Conventional fuel sources are only growing at a 3% or less rate annually. The American Wind Energy Association (AWEA) predicts that over 18,000 MW of new wind power capacity will be installed around the world by 2005 including 2700 MW to be installed in the US (AWEA, 1996).

In order to accelerate wind energy's contribution to generating electricity in the United States, development of low-cost, technologically advanced wind turbines must be a goal. Fortunately, the use of computer modeling has enabled turbine manufacturers to make significant advances toward this goal.

Computer Modeling

Computer models of wind turbines have the potential to save considerable time and money. One no longer needs to design, build and test a prototype in order to

discover whether it will do its intended job. Instead, computer models can do most of the design and test work in a more timely and cost effective manner.

In order for computer models to be most useful, they must accurately represent the wind turbine and the environment to which it is exposed. The model must be compared to test data collected and processed in a thorough and accurate manner. Once a model accurately predicts test results, the code is considered to be valid. A validated code can be used as a tool to predict future events. It can predict dynamic loading, fatigue life, power, stress, yaw behavior, etc. The interplay of all of these factors allows one to change components of an integral design in order to optimize the wind turbine's performance.

Currently, there are a few computer codes that predict the dynamic behavior of wind turbines. FAST was developed at Oregon State University and uses up to 14 degrees of freedom to predict loads on the wind turbine blades, tower, and gear box shaft (Wilson et al., 1996). It also predicts power generated by the turbine as well as yaw motions (of passive yaw systems).

BLADED was developed by Garrad-Hassan and Partners, Ltd. of the United Kingdom (Quarton, D.C., 1996). It performs many of the same functions of FAST. Over the past six years, BLADED has been validated against test data from over one dozen wind turbines of various size and configurations.

Two computer codes were developed at the University of Utah to analyze horizontal axis wind turbines. They are ADAMS (with the AeroDyn subroutines, referred to as ADAMS) and YawDyn. ADAMS is able to incorporate hundreds of degrees of freedom in the wind turbine model. ADAMS models can be accurately built

but require a lot of time to construct and to run. YawDyn, on the other hand, is a much simpler code to use. YawDyn is especially helpful in the early stages of a design since models are easy to alter and run quickly on a personal computer.

Both ADAMS and YawDyn utilize a series of aerodynamic subroutines called the AeroDyn subroutines. These subroutines determine all of the aerodynamic loads that act on the wind turbine blades. It has been shown that wind turbine blades are subject to dynamic stall which occurs as a result of unsteady airfoil motion (Leishman and Beddoes, 1986, McCrosky, 1981, Pierce, 1996).

Dynamic Stall

Dynamic stall causes delayed stall (from the static stall value), increased maximum lift coefficient, $C_{L\ max}$ and hysterisis in the lift, drag and moment coefficients. Thus, the aerodynamic forces are not unique for a given angle of attack as they are in steady aerodynamic situations. This is very important from the standpoint of computer modeling. Dynamic stall must be included in these models in order to accurately represent what is actually occurring (Pierce, 1996, Pierce and Hansen, 1995).

Because of the great effect that dynamic stall has on wind turbine rotors, Pierce (1996) added dynamic stall calculations to the AeroDyn subroutines. By using the Beddoes - Lieshman (1986; 1989) model to calculate lift and drag, Pierce's models showed a significant increase in accuracy when compared to the same model that used only static data.

Dynamic stall affects the rotor in many ways by accounting for a time delay in stall. Dynamic stall is represented in the computer models by an effective angle of attack, which can be quite different from the actual (instantaneous) angle of attack. The

lift, drag and moment coefficients are all different from their static values as a result. This affects other factors such as aerodynamic loads on the blades and power production from the wind turbine's generator. Although all of the aforementioned computer codes perform some dynamic stall calculations on the blades, none of them considers the dynamic stall effects associated with the pitching moments of the blades.

Pitching Moments

Pitching moments are one of the three loads generally referred to when speaking of airfoils. The others are lift and drag. The common point of application of these forces is at the quarter chord point on the airfoil, c/4. See Figure 1.1 for an illustration. This paper focuses on the pitching moments. Pitching moments are generated due to change in air pressure around an airfoil. The pitching moment, PM, is represented by:

$$PM = C_M(1/2\rho V^2)cA \tag{1}$$

where C_M is the pitching moment coefficient, ρ is the air density, V is the local flow velocity, c is the chord length and A is the planform (projected) area.

Dynamic pitching moments can vary drastically from the static pitching moment depending on the airfoil shape, angle of attack range, Reynold's number and reduced frequency. The nondimensionalized reduced frequency, k is:

$$k = 2\pi\omega c/(2V) \tag{2}$$

where ω is the oscillation frequency in Hertz, c is the chord of the airfoil section and V is the wind speed relative to the airfoil.

Figures 1.2 and 1.3 illustrate the stages of dynamic pitching and dynamic flow and how they affect the normal force coefficient and pitching moment coefficient.

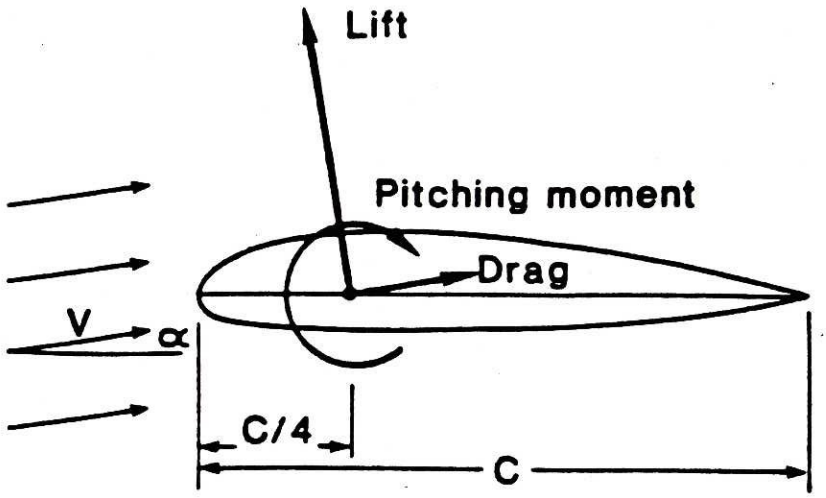

Figure 1.1: An airfoil with lift and drag forces and pitching moment acting on it at the one quarter chord (c/4) location. The local air velocity is V and the angle of attack is α.

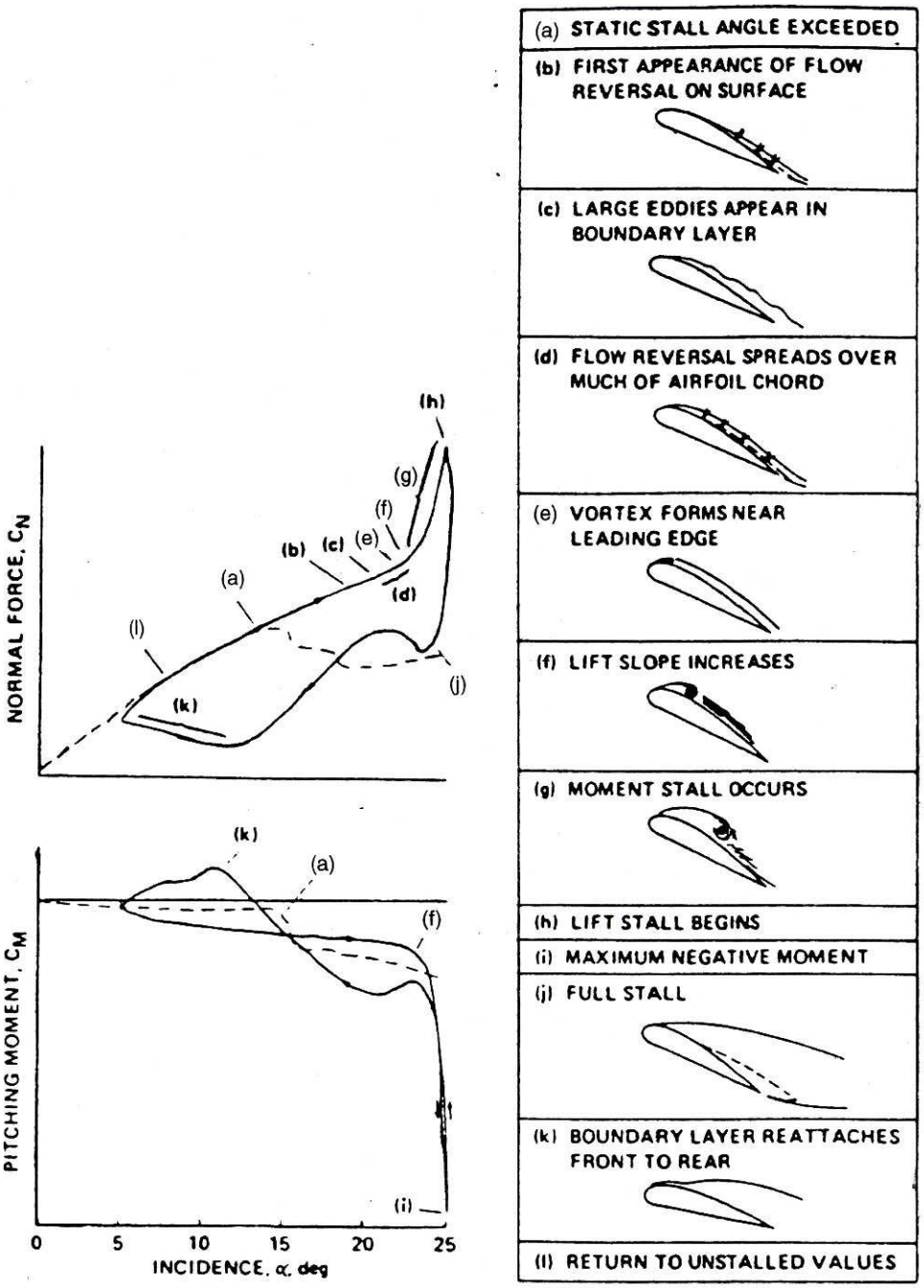

Figure 1.2: Dynamic stall on an NACA 0012 airfoil, from Carr (1988).

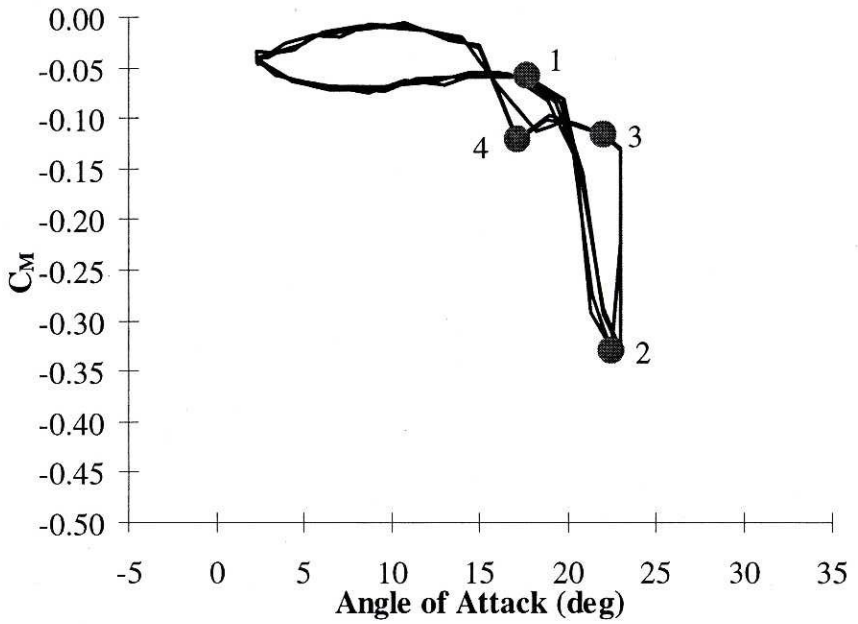

Figure 1.3: Typical representation of pitching moment coefficient vs. angle of attack for an airfoil experiencing dynamic stall. 1- vortex detaches; 2-vortex reaches the trailing edge of the airfoil; 3-full flow separation; 4-start of flow reattachment.

Figure 1.4 shows an NREL S809 airfoil tested under two conditions. One line in the figure represents the static C_M values. The other represents the dynamic values, which are obtained when oscillating the airfoil at a reduced frequency of 0.026. Figure 1.5 shows the same airfoil operating under exactly the same conditions except with a reduced frequency of 0.080. Notice that the higher value of reduced frequency associated with Figure 1.5 causes more dynamic stall and a more open hysterisis loop. In fact, the dynamic response shown in Figure 1.4 is slow enough that it is virtually identical to the static data.

Figure 1.5 also illustrates how dynamic stall allows for a large variance in C_M values for a given angle of attack. For example, at an angle of attack of 22 degrees, the C_M value can be -0.34 (for an increasing angle of attack) or -0.15 (for a decreasing angle of attack).

Until recently, pitching moment information was considered to be unnecessary. Wind turbine blades had virtually no torsional movement. Blades were very stiff, particularly in torsion. However, some current turbines, such as the Carter machines, incorporate a very soft set of blades. Stoddard (1988) found that soft blades (such as the Carter 300 blade) exhibit a great deal of live "elastic twist" which greatly affects power output and blade loads. He also observed that this can cause considerable discrepancies between model predictions (which do not account for dynamic pitching moment effects) and measured power curves. According to the National Renewable Energy Laboratory's (NREL) predictions for future trends in wind turbines, lighter, more flexible machines will become increasingly popular (Thresher, et al. 1994). Jack Cadogan and his colleagues at the U.S. Department of Energy (Cadogan, et al. 1996) believe that by the

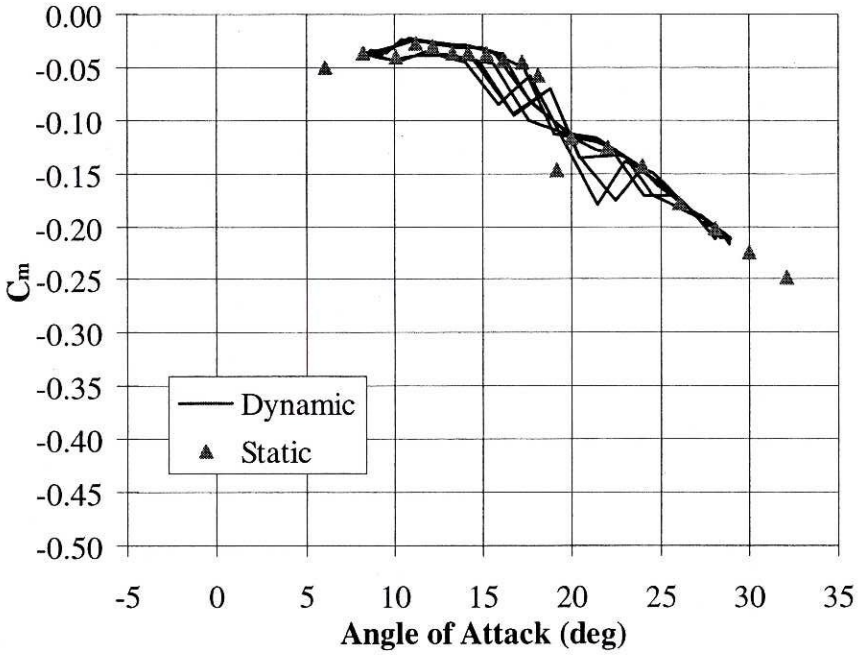

Figure 1.4: Comparison between static and dynamic (with k = 0.026) C_M.

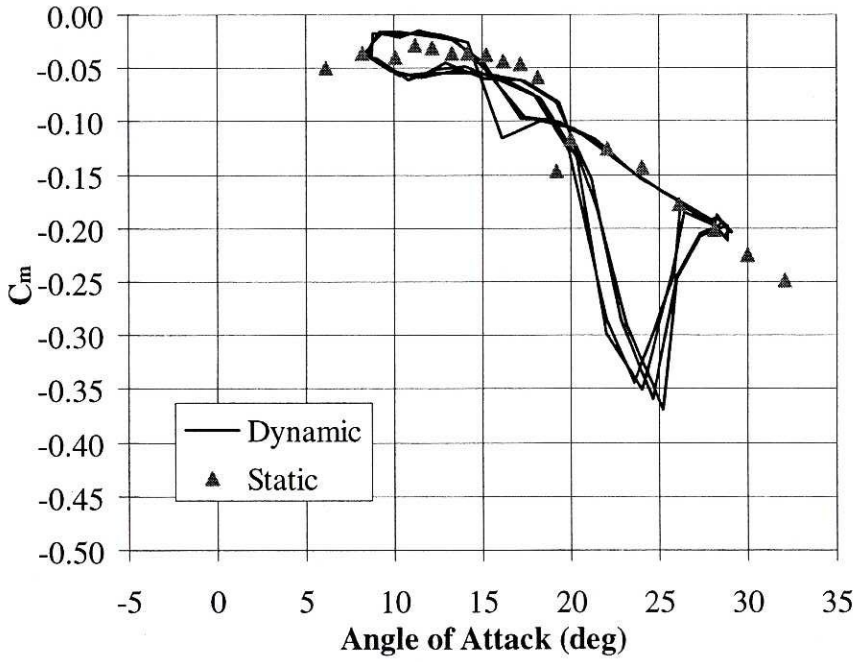

Figure 1.5: Comparison between static and dynamic (with k = 0.080) C_M.

year 2005, systems will be very different from today's turbines. Two of the predicted changes are flexible turbine systems and lighter systems.

Pitching moment calculations are also very helpful in the case of machines that employ pitch control. Torsional movement can occur as the result of a soft pitch control system. This condition occurs when the pitch control system becomes sloppy due to age, wear or poor design.

Goals

The goal of this thesis was to implement an accurate model of pitching moments into the AeroDyn subroutines. The YawDyn and ADAMS codes (which incorporate the AeroDyn Subroutines) would then be run to determine if a significant difference existed from previous codes.

The steps taken to achieve these goals are as follows:

1. Static C_M data were added to their respective airfoil tables and the AeroDyn subroutines were changed to output static C_M values for a given angle of attack.
2. AeroDyn was then changed to account for dynamic stall effects and C_M output from DynStall (which also utilizes AeroDyn) was compared to 2-D test data.
3. After getting satisfactory results for three commonly used wind turbine airfoils (NACA 4415, NREL S809 and the LS1-0417), YawDyn simulations were compared to field test data from the Combined Experiment Rotor (CER) wind turbine.
4. Finally, an ADAMS model of the CER was run with various torsional blade stiffnesses to determine if the implemented pitching moment calculations had

a substantial or negligible effect on the computer model predictions of pitch angle, angle of attack, power and flap moment.

METHODS

This chapter describes how dynamic pitching moment calculations are performed in the AeroDyn subroutines and the information required to make these calculations.

The Method for Determining Pitching Moments

The AeroDyn subroutines (which are used by DynStall, YawDyn and ADAMS) were changed in order to calculate dynamic pitching moments. The basic method of calculating dynamic pitching moments is described by Leishman and Beddoes (1986, 1989) and Leishman (1988, 1989).

Pierce (1996) successfully used the Beddoes-Leishman models (with some modifications) to predict dynamic lift coefficients (C_L) and drag coefficients (C_D) in YawDyn and ADAMS. Pierce gives a brief description of Beddoes and Leishman's methods as well as the modifications made to their techniques.

A detailed description of the unsteady aerodynamic behavior and dynamic stall using the indicial method is given in the aforementioned writings of Leishman and Beddoes. (Note: an indicial function is the response to a disturbance which is applied instantaneously at t=0 and held constant thereafter (i.e., a step function disturbance)). In these papers, Beddoes and Leishman discuss methods for finding C_L, C_D and C_M.

The present work uses some of Pierce's methods, the methods of Beddoes and Leishman and some modifications to the Beddoes-Leishman models to calculate dynamic

pitching moments and pitching forces. What follows is a description of the processes used.

The model analyzes four flow states. Each flow state accounts for a component of the total pitching moment coefficient, C_M. The flow states are:

1. Impulsive pitching moment coefficient due to a step change in angle of incidence, C_{MI}.
2. Impulsive pitching moment coefficient due to a step change in pitching rate, C_{MQ}.
3. Nonlinear moment force coefficient associated with trailing edge flow separation, C_{MF}.
4. Vortex induced pitching moment coefficient, C_{MV}.

These four flow states are described in detail in the following paragraphs. For a given time step, these individual coefficients are additive. When summed together, they represent the pitching moment coefficient at a given blade element location for a given time.

$$C_M = C_{MI} + C_{MQ} + C_{MF} + C_{MV} \tag{3}$$

<u>C_{MI} and C_{MQ}</u>

Impulsive loading relates to the loads an airfoil encounters as a result of an instantaneous change in incidence (i.e., angle of attack) or pitch rate. There are two moment coefficient terms that are correlated with impulsive loading. First, there is the impulsive pitching moment coefficient due to a step change in angle of incidence, C_{MI}. Second is the impulsive pitching moment coefficient due to step change in pitching rate,

C_{MQ}. A unit step change in incidence causes a relatively high initial value of C_{MI} which decays exponentially with time. The instantaneous value of C_{MI} is expressed as:

$$C_{MI}(\hat{t}) = (-1/M)\exp(-\hat{t}/K_I) \tag{4}$$

where K_I is an empirically derived time constant equal to 0.75. $\hat{t}$ is nondimensionalized time, $\hat{t} = tV/c$. M is the Mach number.

C_{MQ} also decays exponentially with time. However, the equation that represents its instantaneous value requires two exponential decay terms:

$$C_{MQ}(\hat{t}) = (0.25/M)\exp(-\hat{t}/K_I) - (1/(3M))\exp(-\hat{t}/K_I^2) \tag{5}$$

For an explanation of the terms in these equations, see Leishman and Beddoes (1986). Figure 2.1 and 2.2 illustrate the exponential decay that is associated with $C_{MI}(\hat{t})$ and $C_{MQ}(\hat{t})$ due to a step change in the incidence or pitch rate of an airfoil.

Leishman and Beddoes (1986) devised an effective model that responds to the continuously varying incidence and pitch rates encountered by rotating blades. At each time step, the model adds a new instantaneous term to terms from previous time steps (which are decaying). By continuously updating these terms, Leishman and Beddoes established the following equations for C_{MI} and C_{MQ}:

$$C_{MI} = -C_{NI}/4 \tag{6}$$

$$C_{MQ} = (-C_{NQ}/4) - (K_I^2 T_I / 3M)(D_{qn} - D''_{qn}) \tag{7}$$

The impulsive normal force coefficient due to a change in the angle of incidence is C_{NI}. The impulsive normal force coefficient due to a change in pitching rate is C_{NQ}. As before, Leishman and Beddoes (1986) explain the terms in these equations in full detail.

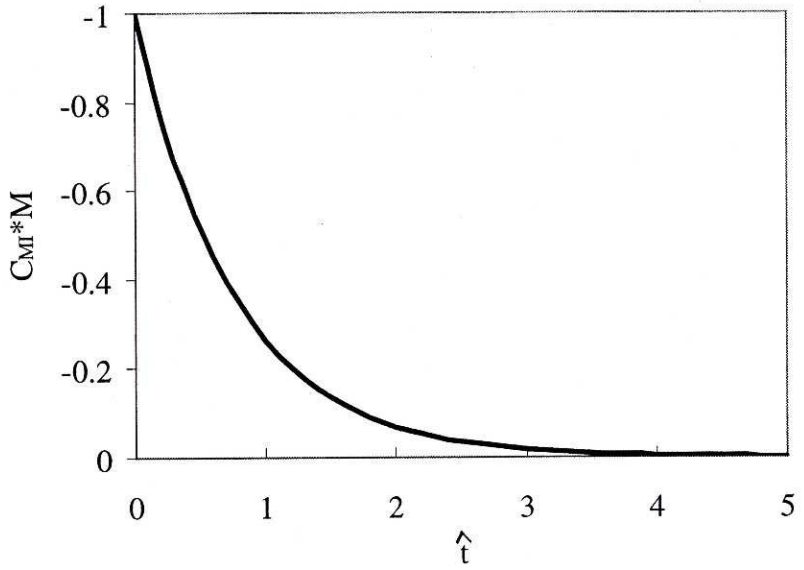

Figure 2.1: Exponential decay of C_{MI} as a function of $\hat{t}$ and M.

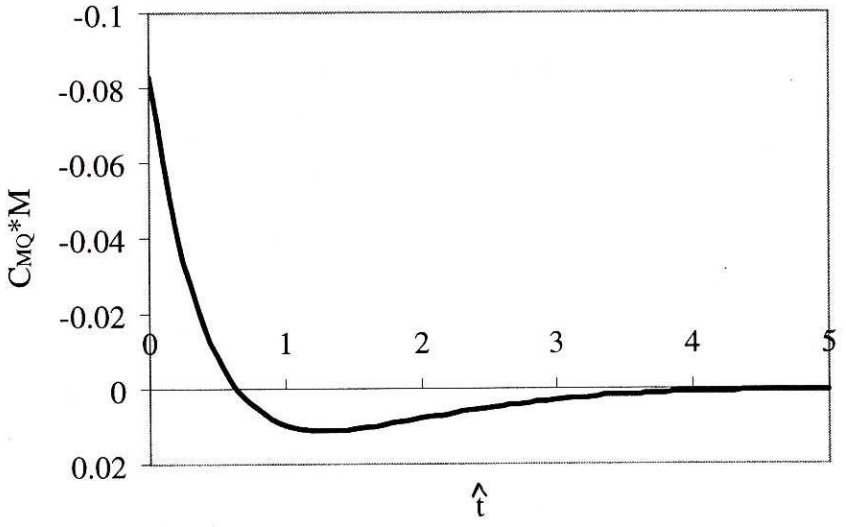

Figure 2.2: Exponential decay of C_{MQ} as a function of $\hat{t}$ and M.

C_{MF}

The nonlinear pitching moment coefficient associated with trailing edge flow separation, C_{MF}, is another term that contributes to the total moment coefficient. Determining C_{MF} requires trailing edge separation point and dynamic angle of attack information.

Calculating the trailing edge separation point. C_{MF} includes both circulatory and noncirculatory components of C_M. The circulatory component is dependent on the trailing edge separation point, f which is defined as:

$$f = x/c \tag{8}$$

where x is the distance from the leading edge to the point of flow separation and c is chord length of the airfoil. The approximate separation point location is calculated using the Kirchhoff theory of simple flow trailing edge separation (Thwaits, 1960).

$$f = \pm\left[2\sqrt{C_N/(\alpha C_{N\alpha})} - 1\right]^2 \tag{9}$$

The sign, + or -, of equation 9 is selected to match the sign of quantity in brackets. C_N is the static normal force coefficient for a given angle of attack, α, and $C_{N\alpha}$ is the slope of the normal force versus angle of attack curve. Equation 9 defines f for all angles of attack even though Kirchhoff's theory was developed for airfoils operating in a limited range of angles of attack. When used this way, f does not literally represent the separation point location and f can be a negative number as is illustrated in Figure 2.3. Using equation 9 to calculate the separation point assumes that f is represented by this equation throughout the entire range (360 degrees) of angles of attack.

Note that this method of finding the trailing edge separation point is a modification to the Beddoes – Lieshman method. They use an empirical equation that works for a limited range of angles of attack and therefore is not acceptable for wind turbine applications, which require aerodynamic data for the entire 360 degree range of angles of attack.

For unsteady flow, there exists a modified separation point, f', due to the temporary effects on the airfoil pressure distribution and the boundary layer response. By using the effective angle of attack, α', as the locator, f' is retrieved from a "look-up table." Leishman and Beddoes give an equation for calculating an effective angle of attack, α', which is defined as:

$$\alpha' = C_N' / C_{N_\alpha} \tag{10}$$

where C_N' is the first order lagged normal force coefficient.

Furthermore, additional effects presented by the unsteady boundary layer response are modeled by applying a first order lag to f'. The result is the final unsteady trailing edge separation point, f'', which represents the effective separation point for an airfoil experiencing unsteady (dynamic) flow. f'' is defined as:

$$f'' = f' - D_{fn} \tag{11}$$

D_{fn} is a deficiency function described by Leishman and Beddoes (1986). If the flow is steady, then the values of f, f' and f'' are all identical and C_{MF} is equal to the static C_M value at the given angle of attack.

Pierce (1996) used equations 23 and 25 from Leishman and Beddoes (1989) to get C_N and C_C values as functions of f''. Subsequent values of C_L and C_D were calculated

directly from C_N and C_C at the equivalent angle of attack, α'. However, to find the value of the nonlinear moment coefficient, C_{MF}, Leishman and Beddoes suggest fitting a curve to the data using a polynomial of the following form:

$$C_{MF} = (K_0 + K_1(1- f'') + K_2\sin(\pi(f'')^m))C_N + C_{M0} \quad (12)$$

This equation contains four constants (K_0, K_1, K_2 and m) which are different for each airfoil and need to be determined through curve fitting. This poses the problem of coming up with each constant for a given airfoil and changing these constants every time the airfoil shape changes. This process would be very time consuming and tedious. Even if one did do this, the equation works well for only a limited angle of attack range. It does not work for the wide range of angles of attack that are of interest for wind turbine blades.

Using the dynamic angle of attack to locate C_{MF}. An alternative to the curve fit method, as a way to come up with C_{MF}, is to use a "look up table" which correlates angle of attack with nonlinear moment coefficient and separation point. This would also run the computer code faster than a curve fit calculation. However, the final unsteady separation point can not be used to locate the angle of attack from the "look-up table" because the separation point values are not unique throughout the entire 360 degree range of alpha values (as seen from Figure 2.3). One would also be unsuccessful retrieving C_{MF} values from a known separation point value. This point is illustrated in Figure 2.4, which shows multiple moment coefficient values for each f value. Therefore, a method of calculating the dynamic angle of attack was devised. The general form of equation 11 was used however, f values were replaced by angles of attack so that:

$$\alpha'' = \alpha' - D_{\alpha n} \quad (13)$$

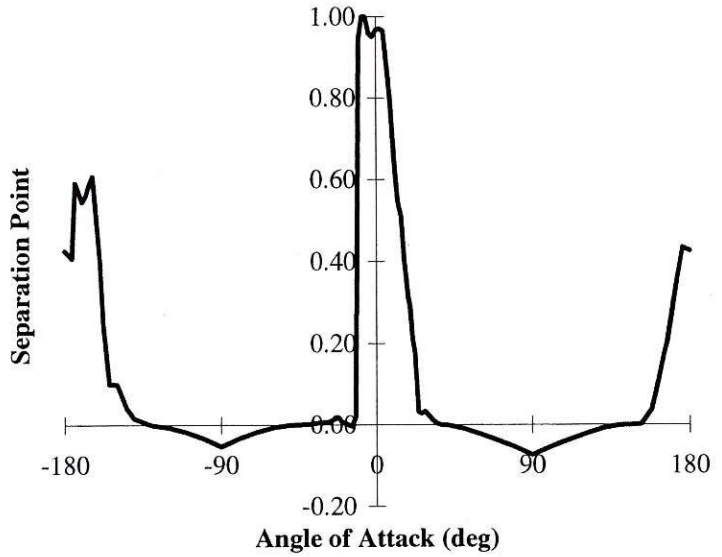

Figure 2.3: Separation point versus angle of attack for an NACA 4415 airfoil.

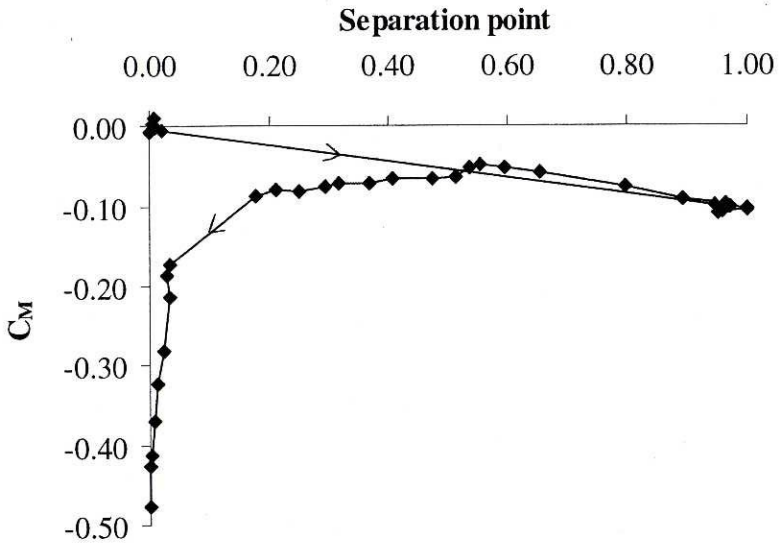

Figure 2.4: Moment coefficient versus separation point for an NACA 4415 airfoil for $-20^0 < \alpha < 40^0$. The arrow goes in the direction of increasing α.

The deficiency function, $D_{\alpha n}$, is similar to the deficiency function from equation 11 such that: $D_{\alpha n} = D_{\alpha(n-1)}\exp(\Delta S/T_\alpha) + (\alpha'_n - \alpha'_{n-1})\exp(\Delta S/(2T_\alpha))$. ΔS is the change in distance traveled by the airfoil in semichords. The value of T_α is to be determined from experimental data and is discussed further in the Time Constants Results section. Note that this exponential decay is assumed by analogy with the separation point deficiency function. The validity of this method will be shown when comparing the values of C_M derived from the AeroDyn subroutines to corresponding test data. Such comparisons are discussed in the Time Constant Results and Two-Dimensional Wind Tunnel Data Simulations Results sections.

C_{MV}

The formation and shedding of vortices also contributes to C_M. The increment of the pitching moment due to an aft-moving center of pressure, C_{MV} is formulated as:

$$C_{MV} = -CP_v C_N^v \tag{14}$$

where CP_v is the vortex-induced center of pressure ($= 0.20(1 - \cos(\pi\tau_v / T_{vl}))$) and C_N^v is the vortex induced normal force coefficient. Leishman and Beddoes (1989) explain equation 14 in full detail. The vortices have little effect on the pitching moment until they are close to the trailing edge of the airfoil. τ_v tracks the position of the vortices such that $\tau_v = 0$ at the onset of separation and $\tau_v = T_{vl}$ when the vortex is located at the trailing edge. The vortex strength decays exponentially as it leaves the trailing edge of the airfoil and $\tau_v > T_{vl}$. T_{vl} represents the amount of time it takes for the vortex to

convect across an airfoil. Higher numbers represent an increase in convection time. T_{vl} is discussed further in the Time Constants Results section.

C_M

As stated in equation 3, the final value of the pitching moment coefficient is the sum of the four components discussed above: $C_M = C_{MI} + C_{MQ} + C_{MF} + C_{MV}$.

These four components of the pitching moment coefficient along with the final value of C_M are illustrated in Figures 2.5-2.9. All of the aforementioned figures are for an NACA 4415 airfoil at a Reynolds number of one million and a reduced frequency of 0.096 (except Figure 2.6, which has a reduced frequency of 0.031). Figure 2.5 represents C_{MF}. The prominence of the hysterisis would decrease if the reduced frequency decreased. This point is illustrated in Figure 2.6, which has a reduced frequency of 0.031. Also note that the hysterisis witnessed in C_{MI} and C_{MV} would be less prominent if the reduced frequency decreased. Figure 2.7 shows both C_{MI} and C_{MQ}. C_{MQ} is virtually zero because the change in pitch rate is nearly zero. C_{MI} on the other hand is prominent because the pitch angle is changing. For the case shown in Figure 2.7, it is an elliptically shaped curve centered about the x-axis with a maximum value of 0.027. C_{MV} is shown in Figure 2.8. It clearly shows that the vortex has no effect on the pitching moment unless the angle of attack is increasing and greater than the stall angle. Under these conditions, the force of the vortex increases as it convects across the airfoil. It reaches its maximum value when the vortex reaches the trailing edge of the airfoil and then decays as the vortex is shed. Finally, Figure 2.9 represents the value of C_M. It is the sum of Figures 2.5, 2.7 and 2.8.

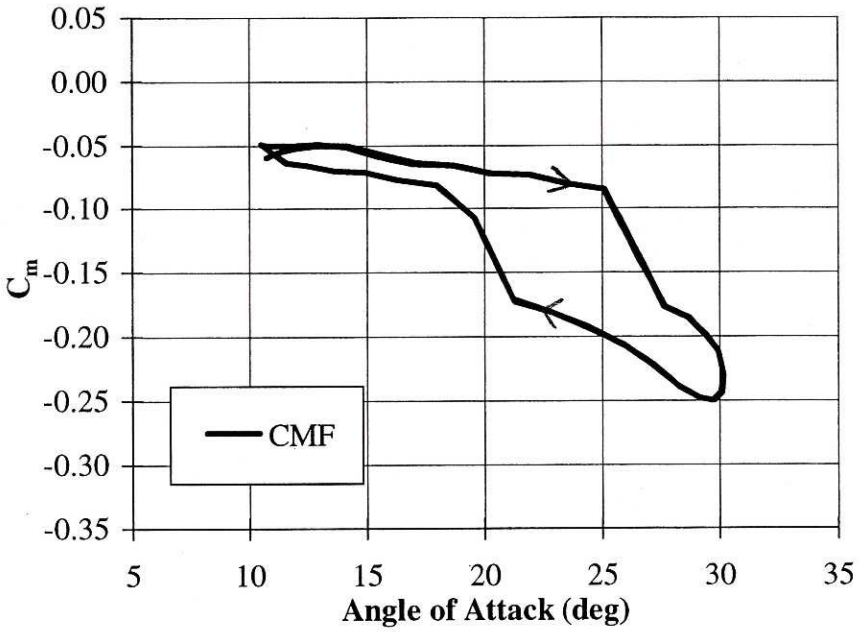

Figure 2.5: NACA 4415 component of the moment coefficient which is asssociated with trailing edge flow separation versus angle of attack. $\alpha=20+10\sin\omega t$, $k=0.096$, $Re=0.9\times10^6$.

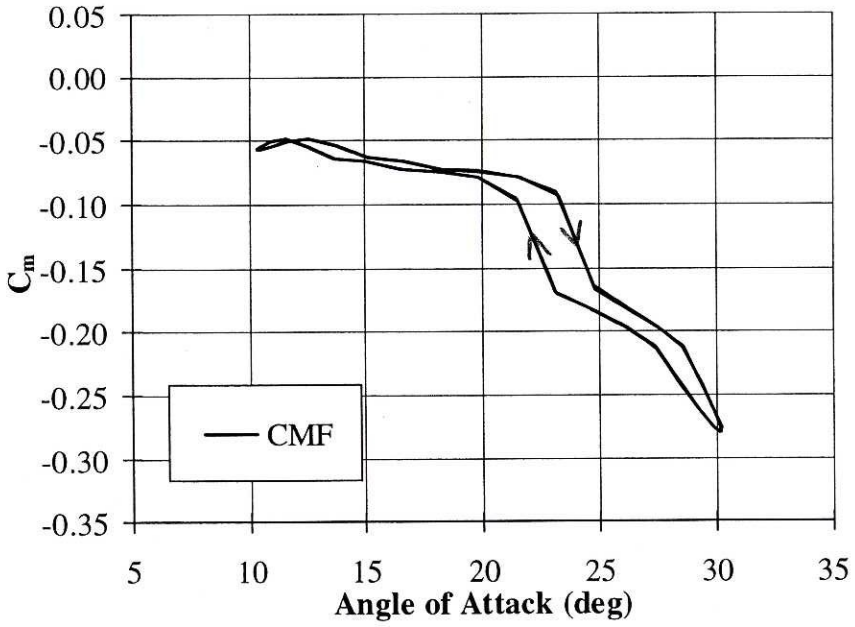

Figure 2.6: NACA 4415 component of the moment coefficient which is asssociated with trailing edge flow separation versus angle of attack. $\alpha=20+10\sin\omega t$, $k=0.031$, $Re=0.9\times10^6$.

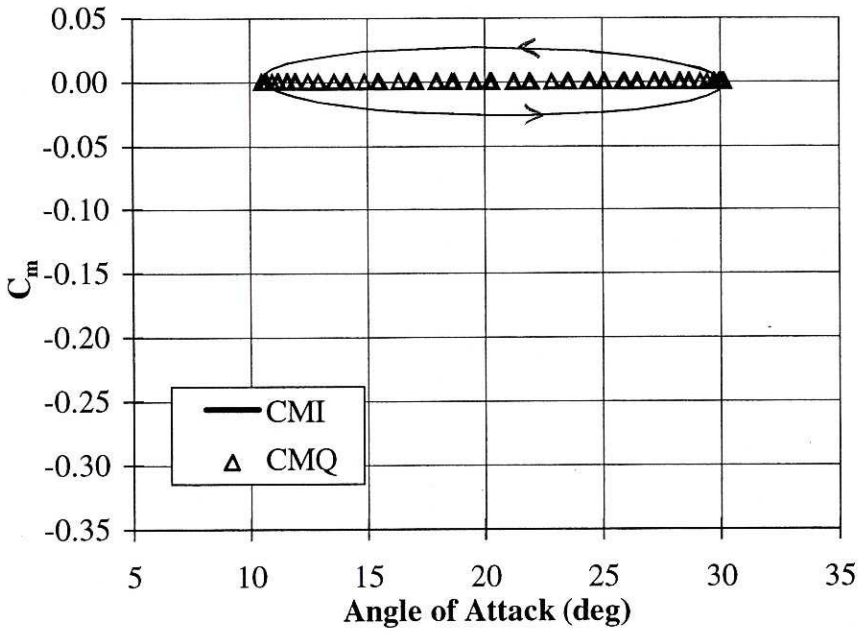

Figure 2.7: NACA 4415, C_{MI} and C_{MQ} versus angle of attack. $\alpha=20+10\sin\omega t$, k=0.096, $Re=0.9x10^6$.

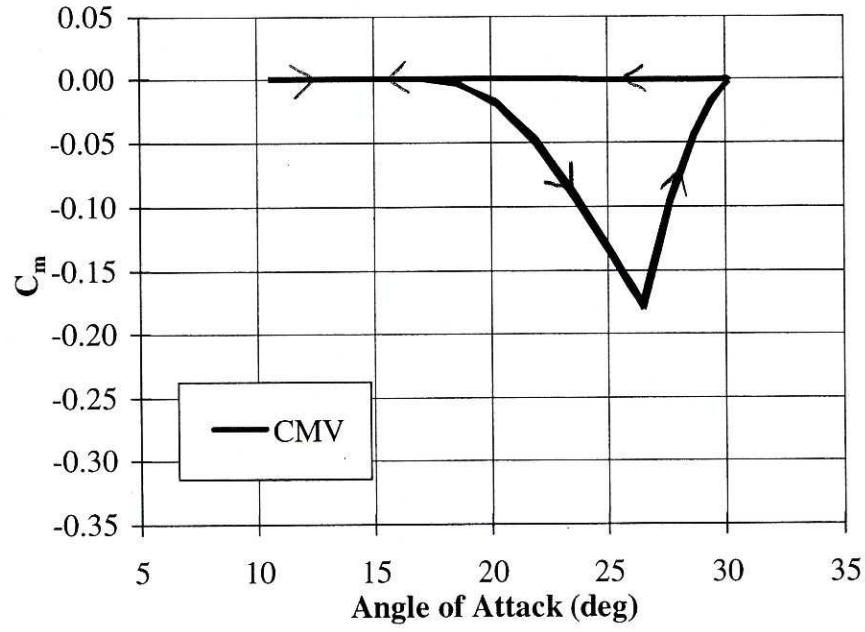

Figure 2.8: NACA 4415, C_{MV} versus angle of attack. $\alpha=20+10\sin\omega t$, k=0.096, $Re=0.9x10^6$.

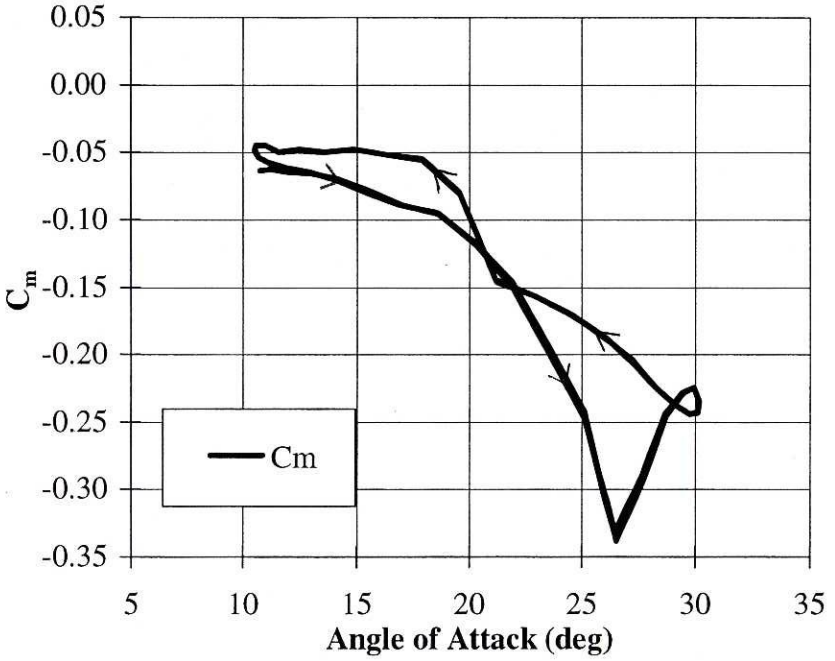

Figure 2.9: NACA 4415, Pitching moment coefficient versus angle of attack. $\alpha=20+10\sin\omega t$, k=0.096, Re=0.9×10^6

As stated earlier (in equation 2), the pitching moment, PM, is equal to $C_M(1/2\rho V^2)cA$.

Static Airfoil Table Requirements

Static airfoil information is necessary in order to run YawDyn, ADAMS and DynStall (see Appendix A) computer models. A sample airfoil table is illustrated in Appendix B. For each airfoil used in a given model, a separate airfoil table must exist. Airfoil tables must be built accurately in order to have a reliable computer model. Constructing accurate static airfoil table requires careful examination, manipulation and extrapolation of the available data. Some of the steps necessary to build airfoil tables are discussed in the following paragraphs.

This research uses static data that were compiled at the Ohio State University (OSU) by Gregorek and Reuss (1994). Three airfoils were examined: NACA 4415, NASA LS1-0417, and the NREL S809. Gregorek and Reuss also ran tests using these airfoils under dynamic situations oscillating sinusoidally at various frequencies and angle of attack ranges. All wind tunnel data gathered by Gregorek and Reuss are referred to as OSU test data.

By using the static airfoil data and the input parameters (time, angle of attack and wind velocity) of the dynamic tests, the computer program (code) DynStall is able to predict the dynamic pitching moments. DynStall, originally written by Pierce (1996), was updated in the present work to account for pitching moments. The output of DynStall is compared to the dynamic pitching moments from the OSU tests. This topic is discussed

further in the Two-dimensional Wind Tunnel Data Simulation Results section of this thesis.

Determining Drag Coefficients

The static OSU data includes pressure drag and wake drag for each angle of attack. Figure 2.10 illustrates an example of these values for an NREL S809 airfoil. This figure shows that the pressure drag value is very low between -5 and 8 degrees. In fact, at some angles of attack it is zero, values too low to be believed. OSU used pressure taps located along the airfoil surface in order to measure the pressure and then calculate a drag coefficient. As can be seen from Figure 2.10, this method does not work well when the absolute value of the angle of attack is less than approximately 10 degrees. The majority of the drag force in this region is due to viscous drag, which can not be measured by pressure taps. Viscous drag forces are parallel to the surface of the airfoil while the pressure taps are only able to measure pressure which is perpendicular to the airfoil surface.

In order to get a more accurate value for the drag coefficient in this region, OSU compiled wake drag values. The wake drag (of a particular airfoil at a steady angle of attack) is calculated using momentum balance of the upstream and downstream flow within a control volume (for specific information consult Batchelor, 1988). This method works well at low angles of attack and low wind speeds. However, this method fails when there is too much turbulence in the wake of the airfoil. Therefore, the wake drag values are used for resultant drag coefficient values between -7 and 8 degrees. All other resultant drag coefficient values are taken from the pressure drag values. Combining the

wake drag and pressure drag values in this manner results in a drag coefficient which is more accurate. The values are always positive and the curves are smooth. The resultant drag coefficients for the NREL S809 are illustrated in Figures 2.10 and 2.11.

Extending the Range of C_M, C_L and C_D Values

It is necessary to have lift, drag and pitching moment data for a range of angles of attack from approximately -5 to 35 degrees in order to compare the models to dynamic test data. However, the OSU static airfoil table data for the NASA LS(1)-0417 and the NREL S809 is incomplete for a Reynold's number (Re) of $1.5x10^6$. OSU only specifies values associated with angles of attack up to approximately 20 degrees. Therefore, it was necessary to extend this static data to 35 degrees in order for it to be used for DynStall comparisons. The procedure for doing this is as follows. First, the NACA 4415 data were examined since it is complete over the necessary angle of attack range for both Re of 1 million and Re of 1.5 million. Figure 2.12 show the moment coefficient comparison for these two cases. From this comparison, it is shown that the static C_M values are nearly identical at high angles of attack.

Next, the NACA 4415 static C_M data are compared to dynamic data at a low oscillation frequency (both of which are at $Re=1.5x10^6$) and high angle of attack range. This comparison (see Figure 2.13) shows that the dynamic data generally circles (and in this case the hysterisis is so small that it is virtually non-existent) around the static data. These comparisons were used as general rules when extending the airfoil data for the NASA LS(1)-0417 and the NREL S809 into the higher angle of attacks (for Re of 1.5 million). See Figures 2.14-2.17 for illustrations of the extended data for these airfoils.

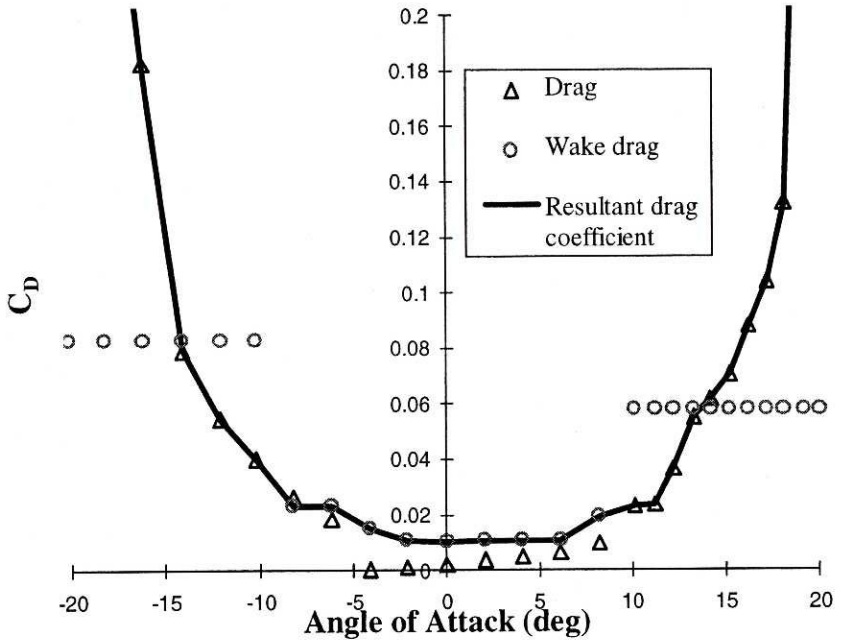

Figure 2.10: NREL S809 drag coefficient versus angle of attack.
The resultant drag coefficient is a combination of the drag and the wake drag.

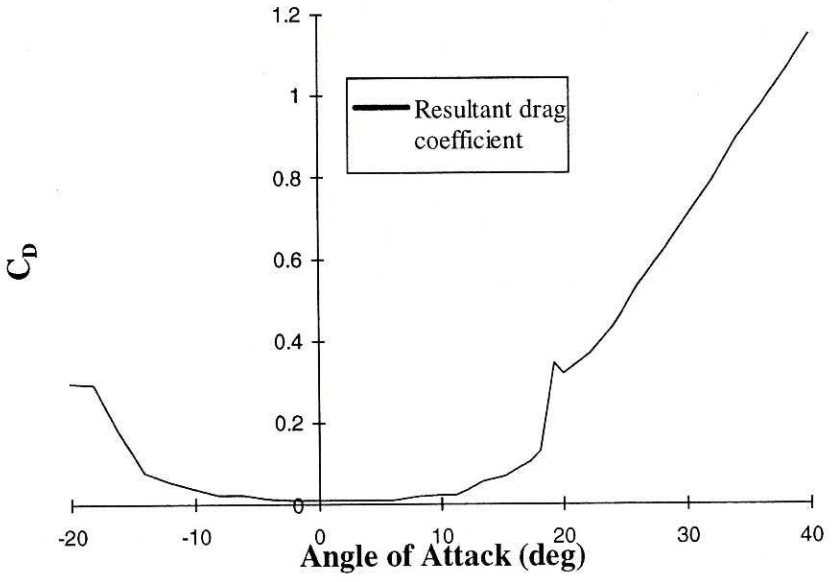

Figure 2.11: NREL S809 drag coefficient versus angle of attack.
The resultant drag coefficient over a large angle of attack range.

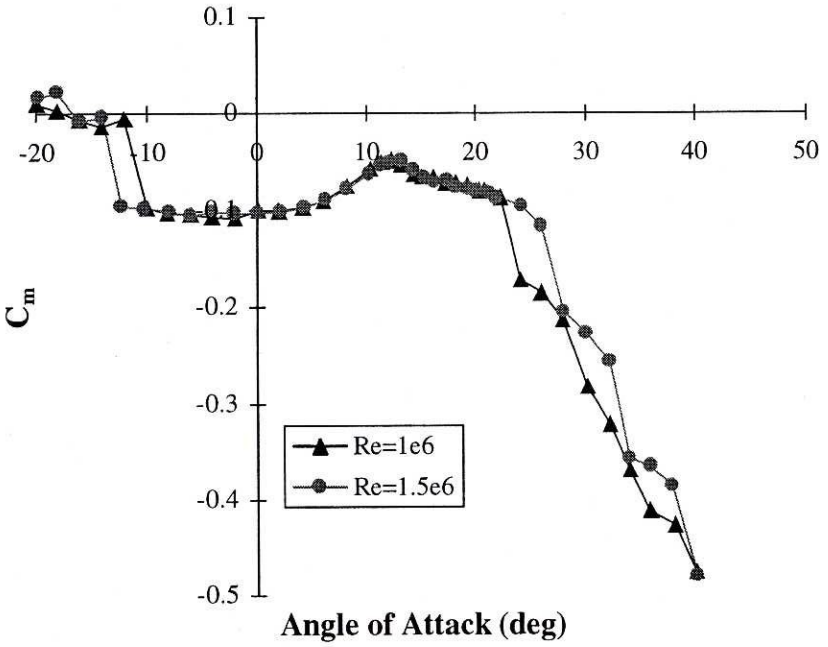

Figure 2.12: NACA 4415 moment coefficient versus angle of attack. Static data for Re=1.0x10^6 and Re=1.5x10^6.

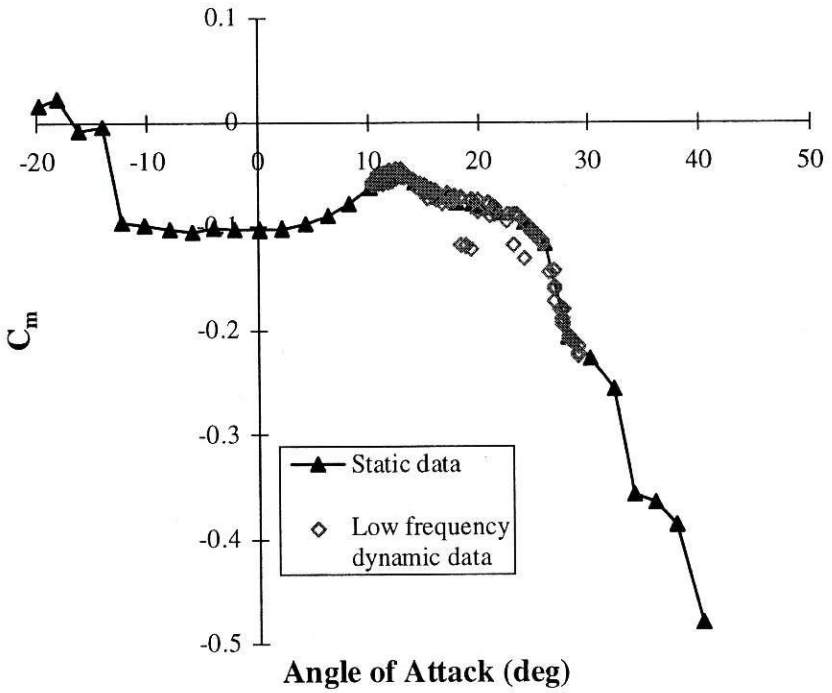

Figure 2.13: NACA 4415 moment coefficient versus angle of attack. Static data versus low frequency dynamic data at Re=1.5x10^6.

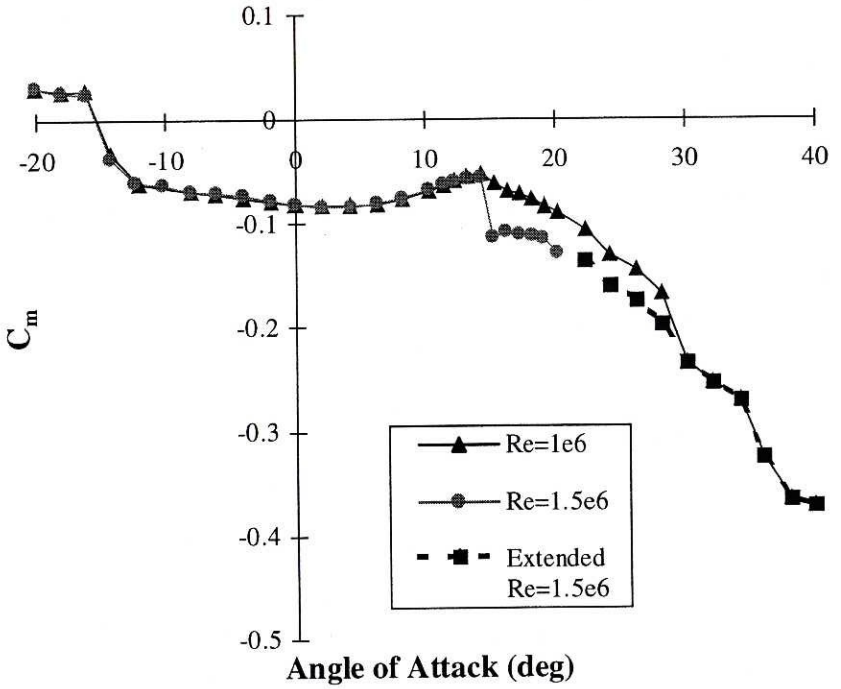

Figure 2.14: NASA LS(1)-0417 moment coefficient versus angle of attack. Static data for Re=1.0x10^6 and Re=1.5x10^6. Extended static data for Re=1.5x10^6.

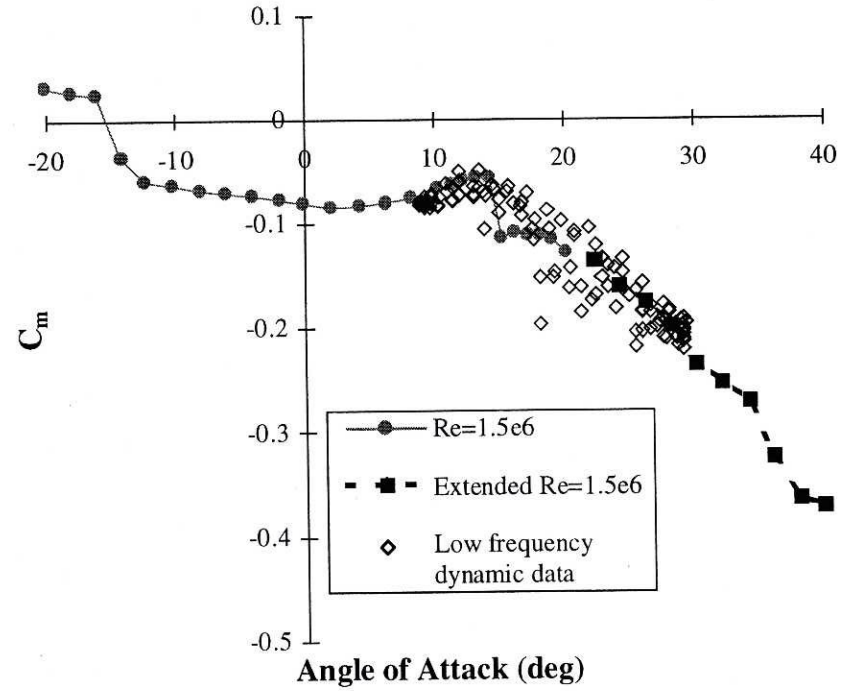

Figure 2.15: NASA LS(1)-0417 moment coefficient versus angle of attack. Static data, extended static data and low frequency dynamic data for Re=1.5x10^6.

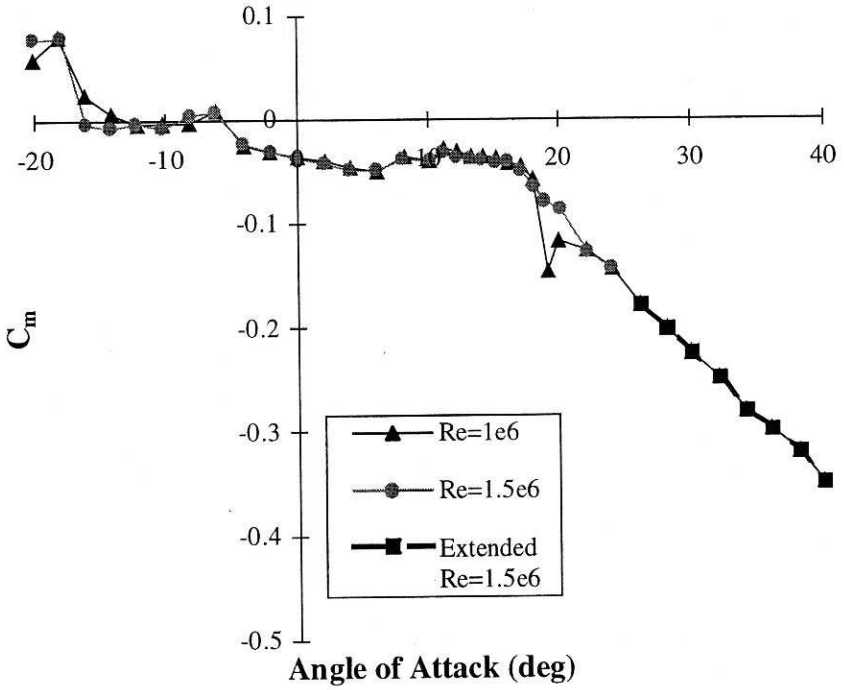

Figure 2.16: NREL S809 moment coefficient versus angle of attack.
Static data for Re=1.0x10^6 and Re=1.5x10^6. Extended static data for Re=1.5x10^6.

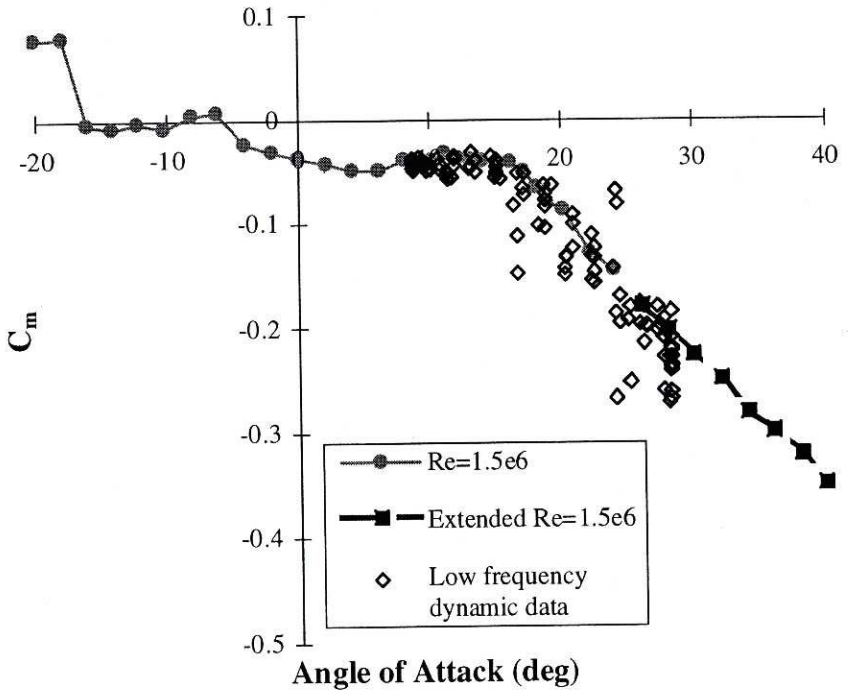

Figure 2.17: NREL S809 moment coefficient versus angle of attack.
Static data, extended static data and low frequency dynamic data for Re=1.5x10^6.

Similar analyses were also used to extend the drag and lift coefficients. Figures 2.18-2.21 illustrate the extensions of these coefficients. It is also useful to compare low frequency dynamic data at Reynolds number of one million and one and a half million when extending the lift coefficient data. There is a large amount of hysterisis, even in low frequency cases, thus making it difficult to predict the static values in this region (see Figure 2.22). The hysterisis loops of these two conditions are so close that the static C_L data can also be assumed to be virtually identical.

Determining $C_{n\text{-}stall}$

Other input parameter constants are needed to build an airfoil table for a given airfoil at a given Reynolds number. See Pierce (1996) for an explanation of some of these constants. One of the most difficult parameters to define is the value of the normal force coefficient at stall ($C_{n\text{-}stall}$). This parameter is ambiguous for airfoils that do not encounter hard stall (such as the NACA 4415 and the NREL S809). This point is illustrated in Figures 2.23-2.24. These figures show that C_N does not reach its maximum value and then drop off sharply as it does for the NASA LS(1)-0417 shown in Figure 2.25. Instead, it reaches a maximum C_N value that is very similar to the value for data points at the previous and next few angle of attacks (i.e. a rather flat C_N peak). When this situation occurs, it is best to choose the stall angle (α_{stall}) at the middle of the relatively flat section of the curve (as is shown in the following paragraphs). Therefore, the stall angles of the NACA 4415 and the NREL S809 are 17 and 15 degrees, respectively.

Because of the presence of dynamic stall and hysterisis, the value of $C_{n\text{-}stall}$ is not the maximum C_n value taken from the static table. Instead it is found as illustrated in

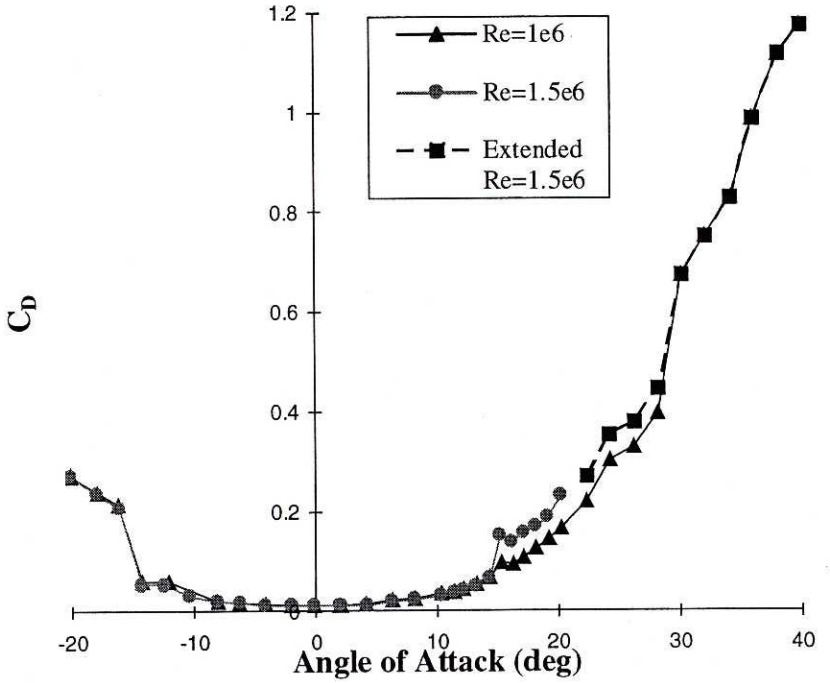

Figure 2.18: NASA LS(1)-0417 drag coefficient versus angle of attack.Static data for Re=1.0x10^6 and Re=1.5x10^6. Extended static data for Re=1.5x10^6.

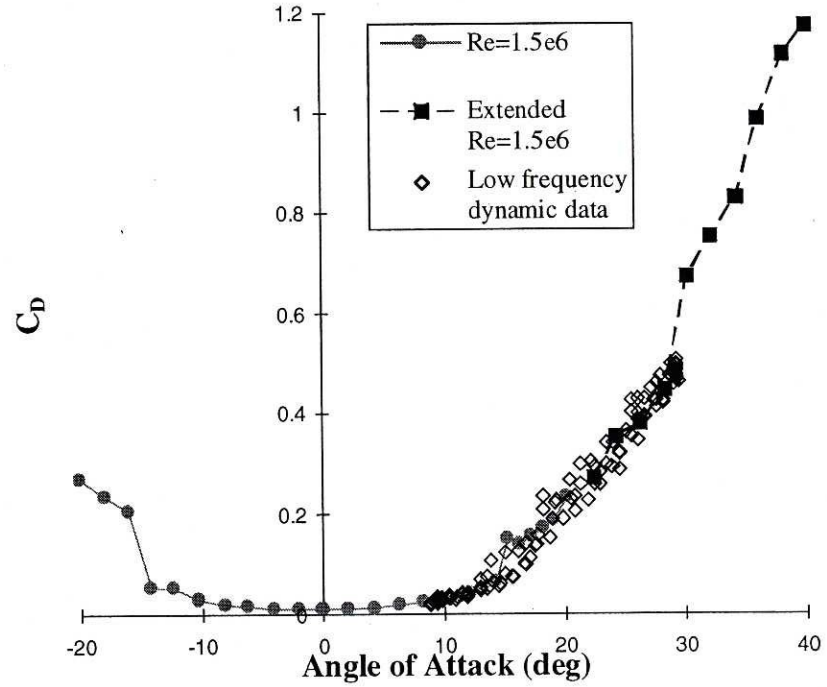

Figure 2.19: NASA LS(1)-0417 drag coefficient versus angle of attack. Static data, extended static data and low frequency dynamic data for Re=1.5x10^6.

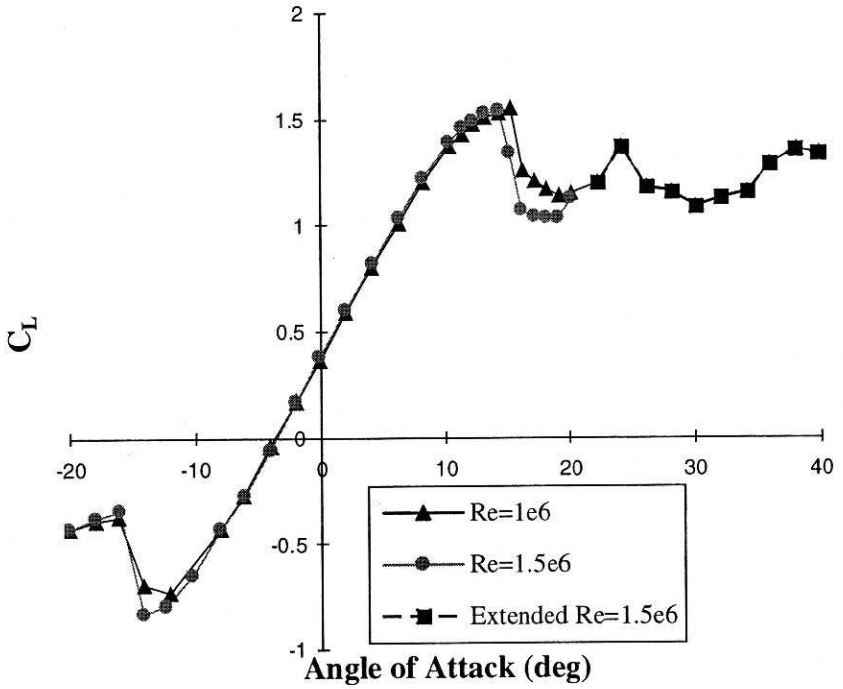

Figure 2.20: NASA LS(1)-0417 lift coefficient versus angle of attack.
Static data for Re=1.0x10^6 and Re=1.5x10^6. Extended static data for Re=1.5x10^6.

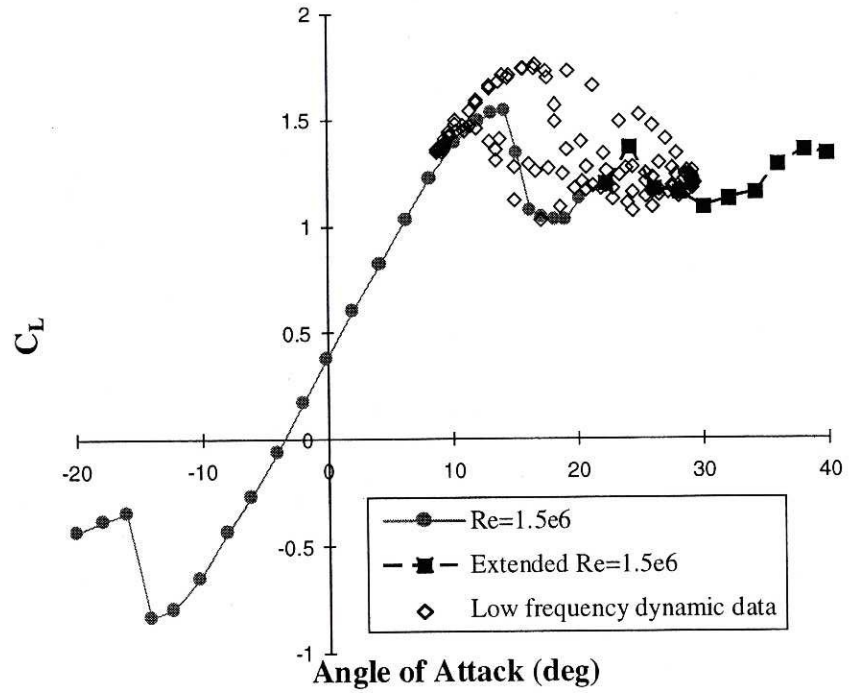

Figure 2.21: NASA LS(1)-0417 lift coefficient versus angle of attack.
Static data, extended static data and low frequency dynamic data for Re=1.5x10^6.

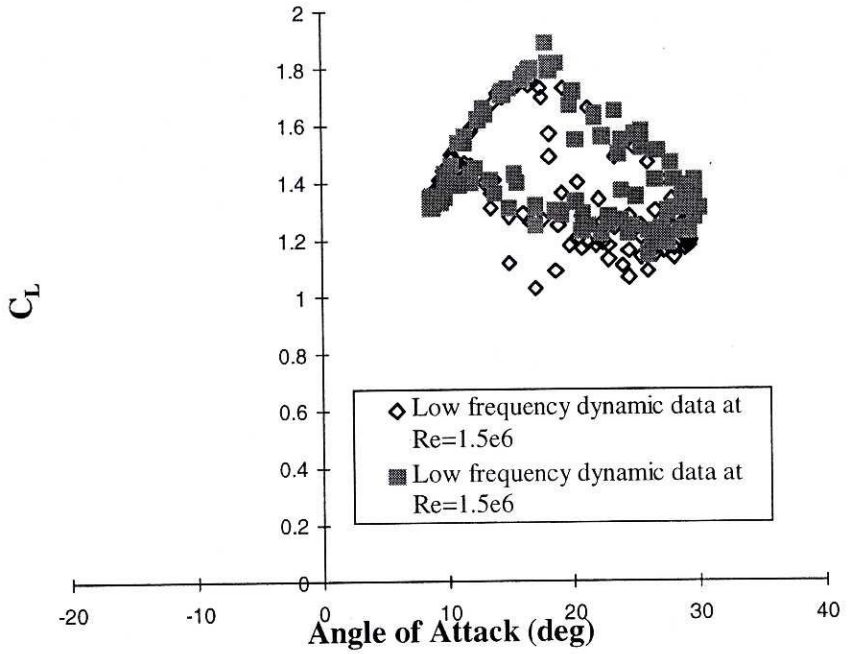

Figure 2.22: NASA LS(1)-0417 lift coefficient versus angle of attack. Low frequency dynamic data for Re=1.0x10^6 and Re=1.5x10^6.

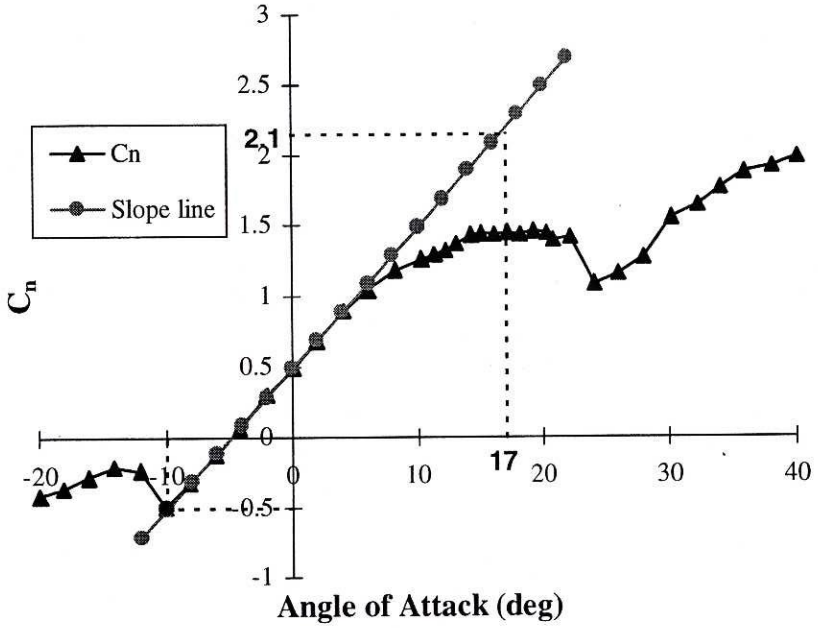

Figure 2.23: NACA 4415 normal force coefficient versus angle of attack.

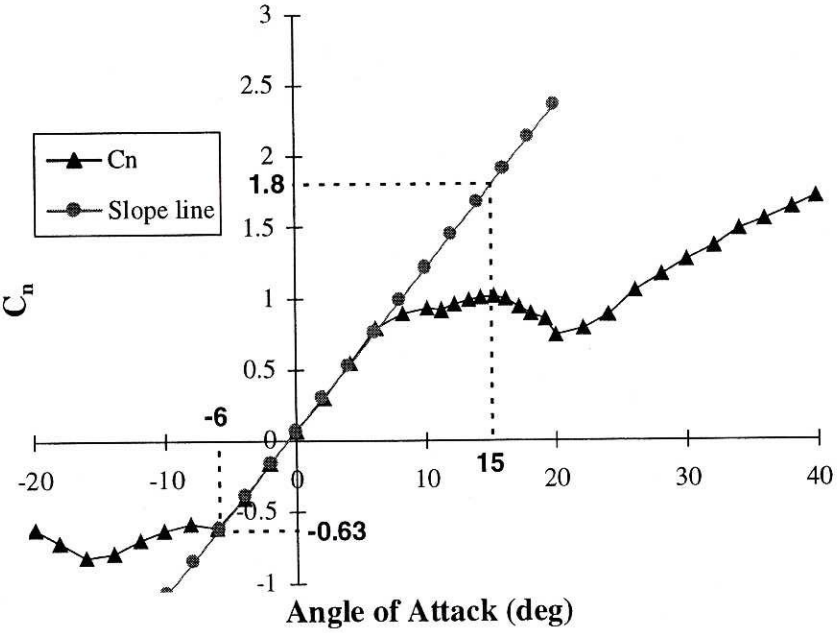

Figure 2.24: NREL S809 normal force coefficient versus angle of attack.

Figures 2.23, 2.24 and 2.25. The $C_{n\alpha}$ line is extended until it intersects the α_{stall} line. From this point, the value of $C_{n\text{-}stall}$ is read from the plot. $C_{n\text{-}stall}$ is 2.1 for the NACA 4415 and 1.8 for the NREL S809.

Choosing the correct value of $C_{n\text{-}stall}$ is very important. In order to illustrate this point, the NACA 4415 was analyzed at three different conditions for the case when $\alpha=14+10\sin\omega t$, $k=0.086$ and $Re=1.0x10^6$. Condition #2 uses the aforementioned method of determining the values of stall angle and $C_{n\text{-}stall}$. Condition #1 under predicts and condition #3 over predicts these numbers. These three conditions are listed in Table 2.1.

Figures 2.26-2.28 graphically show these three conditions (note that the data point at 26 degrees is a bad point). Notice how drastically different these plots are. Although they are all nearly identical and very much in agreement with the data as the angle of attack decreases from its maximum value of 24 degrees to its minimum value of 4 degrees, they are very different from each other as the angles of attack increase.

The condition #1 flow simulation is excellent for the attached flow from 4 degrees until the onset of vortex detachment at 12 degrees. The model predicts that the vortex builds too early, dissipates too fast and that the vortex reaches the trailing edge of the airfoil when the angle of attack is 20 degrees. It then sheds off the back of the airfoil and a secondary vortex builds at 22 degrees and reaches the trailing edge at the maximum angle of attack, 24 degrees.

Condition #2 does a very good job of predicting the data. The prediction is excellent from the minimum angle of attack at 4^o all the way to the onset of the vortex contribution at 17 degrees. The model continues to accurately predict the data as the vortex builds and reaches the trailing edge of the airfoil at 23 degrees. At the maximum

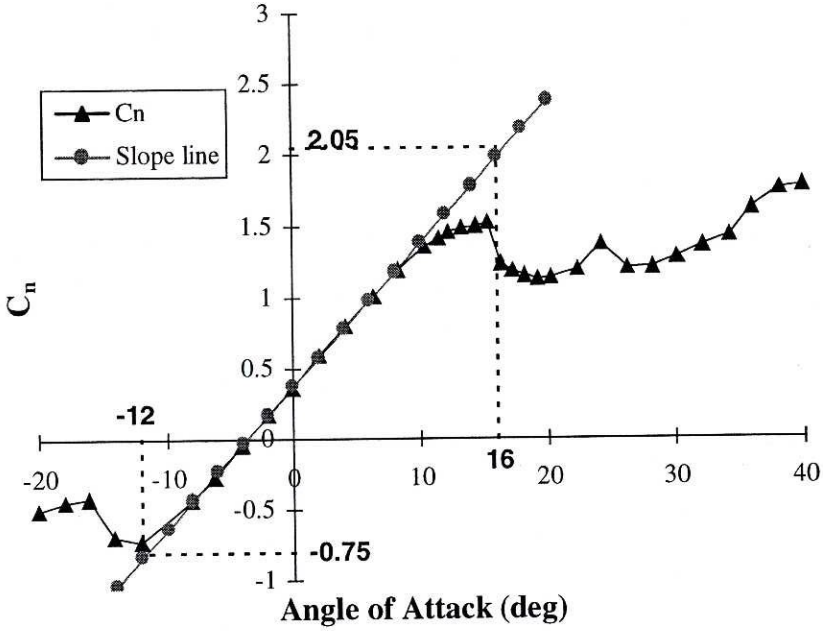

Figure 2.25: NASA LS(1)-0417 normal force coefficient versus angle of attack.

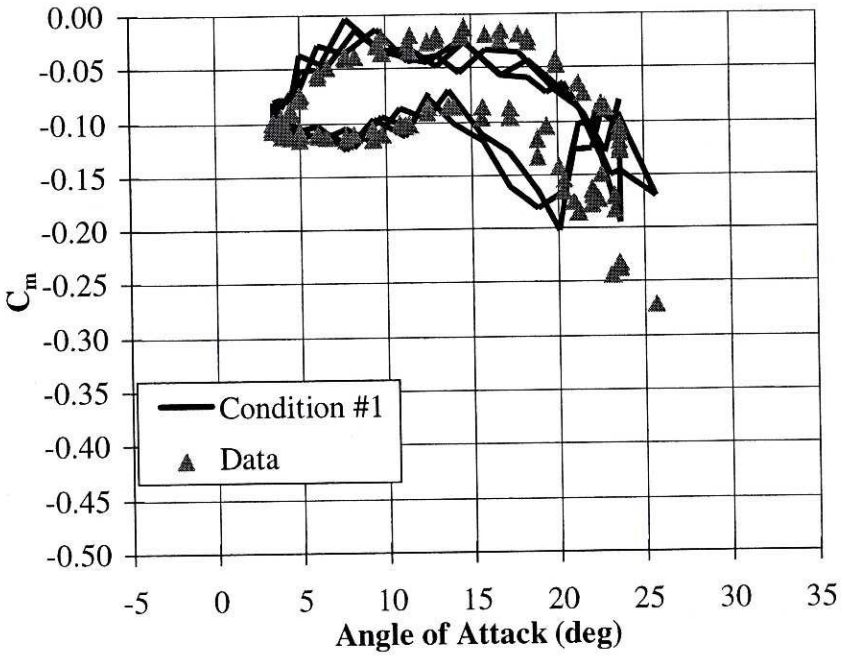

Figure 2.26: NACA 4415 moment coefficient versus angle of attack. Simulated using condition #1 from Table 2.1. $\alpha=14+10\sin\omega t$, $k=0.086$, $Re=1.0\times10^6$.

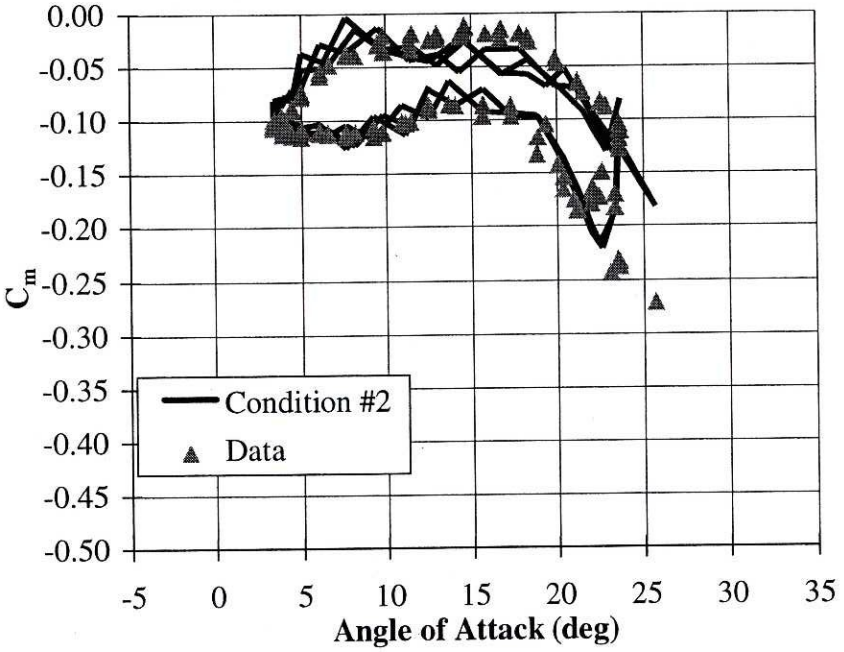

Figure 2.27: NACA 4415 moment coefficient versus angle of attack. Simulated using condition #2 from Table 2.1. $\alpha=14+10\sin\omega t$, k=0.086, Re=1.0x10^6.

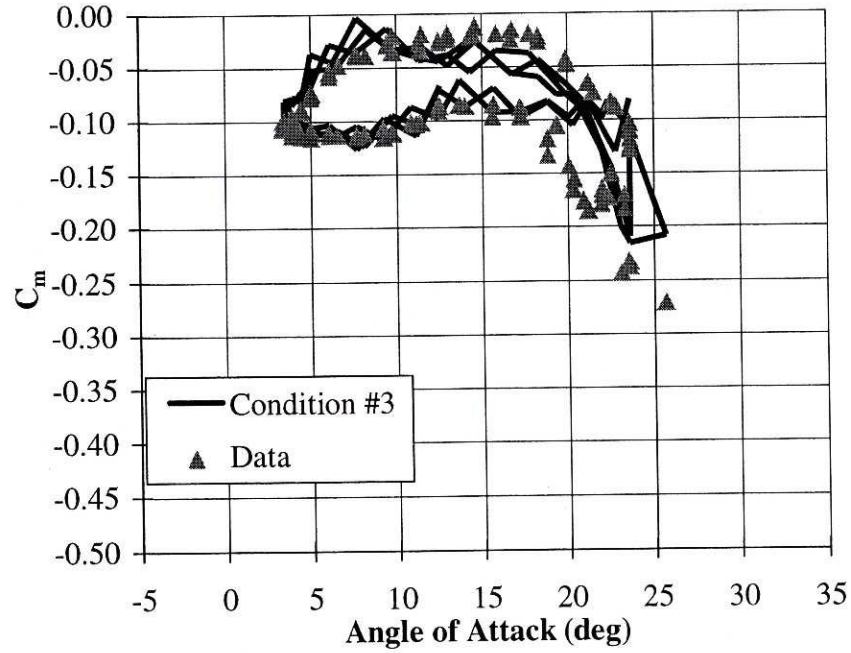

Figure 2.28: NACA 4415 moment coefficient versus angle of attack. Simulated using condition #3 from Table 2.1. $\alpha=14+10\sin\omega t$, k=0.086, Re=1.0x10^6.

Table 2.1: α_{stall} and $C_{n\text{-}stall}$ at three test conditions.

Condition number	α_{stall}	$C_{n\text{-}stall}$
1	10	1.5
2	17	2.1
3	22	2.7

angle of attack, 24 degrees, the data show a higher nose down pitching moment coefficient than the model prediction. The model's prediction of C_M is approximately 0.02 less than the data at this point. Overall, the shape and magnitude of C_M predictions using condition #2 is excellent.

Condition #3 does well but the vortex contribution does not commence until 22 degrees, which is five degrees later than the data indicates. The magnitude of the maximum nose down pitching moment is 0.03 less than the data.

TIME CONSTANTS RESULTS

The Methods section described the four components of pitching moment (C_{MI}, C_{MQ}, C_{MF} and C_{MV}) that are summed to form the pitching moment coefficient, C_M. The formulas used to calculate C_{MF} and C_{MV} require the use of time constants.

There are five time constants associated with the Beddoes-Leishman dynamic stall model. They are listed in Table 3.1 along with their recommended values using different reference sources. Leishman and Beddoes (1986) and Leishman (1989) recommend time constants found empirically when testing the NACA 0012 at Mach numbers of 0.3 and 0.4 respectively. However, they recommend altering the time constants to identify those that best fit the model. For example, Pierce (1996) borrowed from these sources in order to identify time constants that accurately predicted dynamic lift and drag for the same three airfoils tested in this thesis.

Table 3.1: Time constants.

Time constant	Leishman & Beddoes (1986)	Leishman (1989)	Pierce (1996)	Minnema (1998)
T_p	1.7	2.0	1.7	1.7
T_f	3.0	2.5	3.0	3.0
T_α	-	-	-	0.3
T_v	6.0	6.0	6.0	6.0
T_{vl}	7.0	11.0	11.0	11.0

In this research (referred to as Minnema, 1998 in Table 3.1) several different time constant combinations were tested to predict pitching moment coefficients. When a variety of data sets which incorporate different airfoils, reduced frequencies and Reynolds numbers were evaluated it was concluded that the combination used provided accurate predictions. Note that the time constant, T_α, was not used prior to this research. The following paragraphs discuss how the time constants were varied and their subsequent results.

T_p and T_f

T_p is a time constant that is used to get the deficiency function D_{pn} (equation 14 from Leishman and Beddoes, 1989). D_{fn} subsequently helps determine α'. T_f is an empirically derived time constant that is used to determine the deficiency function D_{fn}. D_{fn} is a term in equation 11 (which determines the effective separation point, f''). Altering these time constant values within the ranges in Table 3.1 had very little effect on the outcome of the C_M values.

T_α

T_α, the time constant used to find $D_{\alpha n}$ and α'' (see equation 13), was developed for this research project. It is needed to locate C_{MF} from a "look-up table." To determine T_α different dynamic cases were run in the computer code DynStall and C_M outputs were compared to wind tunnel test data. DynStall is described in the Two-Dimensional Wind Tunnel Data Simulation Results section. A T_α value of 0.3 gave the closest agreement

with the Ohio State University wind tunnel test data. Many different values (including 3.0, 1.5, 0.3 and 0.003) were tested before 0.3 was decided upon.

Figures 3.1 and 3.2 show an extreme example of how the shape of the C_M curve changed when a T_α value of 3.0 (Figure 3.1) was used compared to using 0.3 (Figure 3.2). These two plots are for the NACA 4415 airfoil at a reduced frequency, k, of 0.096 (the highest k value of all the dynamic wind tunnel data studied in this research).

Under most of the situations tested, changing T_α from 3.0 to 1.5 or 0.3 made only a slight difference. Figures 3.3 and 3.4 are typical examples. Both are for the NASA LS(1)-0417 airfoil with k=0.077. In Figure 3.3 the C_M curves are virtually identical for 3.0, 1.5 and 0.3 throughout the test cycle except near the end of the cycle when the flow starts to reattach. This is the range of angles of attack starting at approximately 8 degrees and extending back (as the angle of attack decreases) to the smallest angle of attack value of this test (about -4 degrees). The plots are virtually identical as the airfoil increases in angle of attack from -4 degrees to its greatest value of 18 degrees. The plots continue to be the same as the angle of attack decreases until the airfoil is once again at approximately 8 degrees.

Figure 3.4 illustrates that a T_α value of 0.3 produces identical results to a value of 0.003. This implies that the deficiency function (see equation 13), $D_{\alpha n}$, is basically zero in both cases. In other words, $\alpha'' = \alpha'$. However, (as shown in Figures 3.1 and 3.2) T_α has much more of an effect on $D_{\alpha n}$ and C_M at higher reduced frequencies.

Pierce (1996) concluded that the Combined Experiment Rotor (CER) wind turbine operates in environments below reduced frequencies of 0.1 the majority of the time (not including the times when a blade is passing through the tower's shadow). Thus,

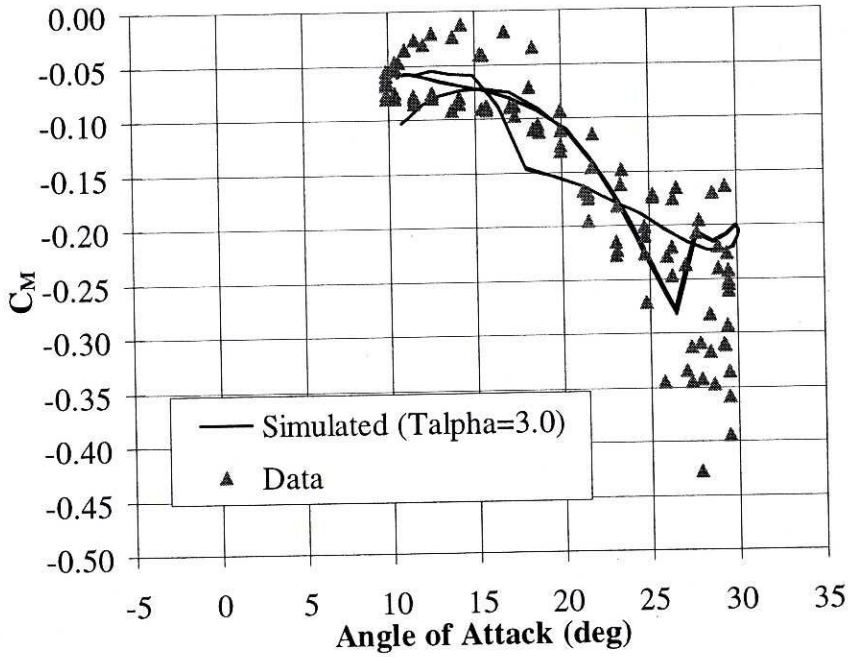

Figure 3.1: C_M vs. α with $T_\alpha = 3.0$ for the deficiency function, $D_{\alpha n}$ calculation.

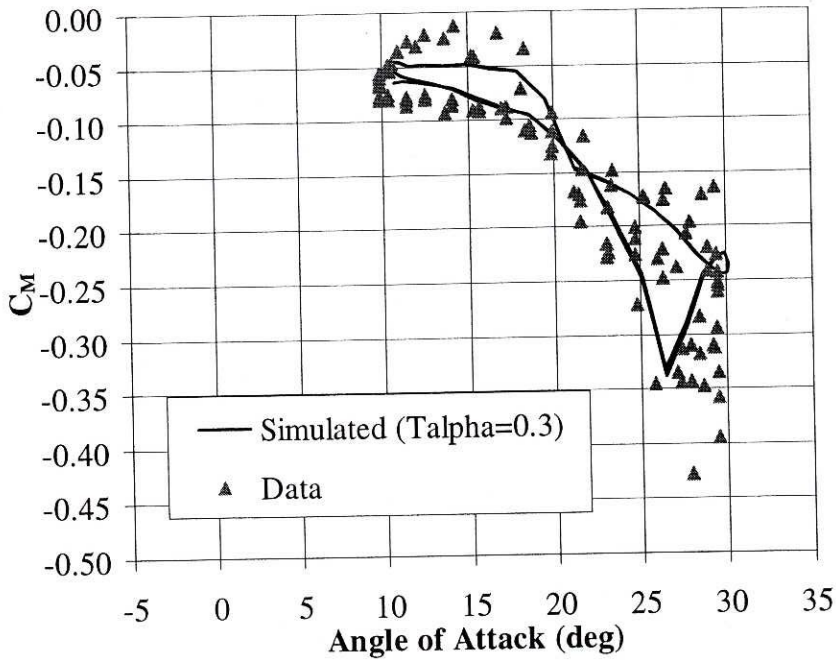

Figure 3.2: C_M vs. α with T_α =0.3 in the deficiency function, $D_{\alpha n}$ calculation.

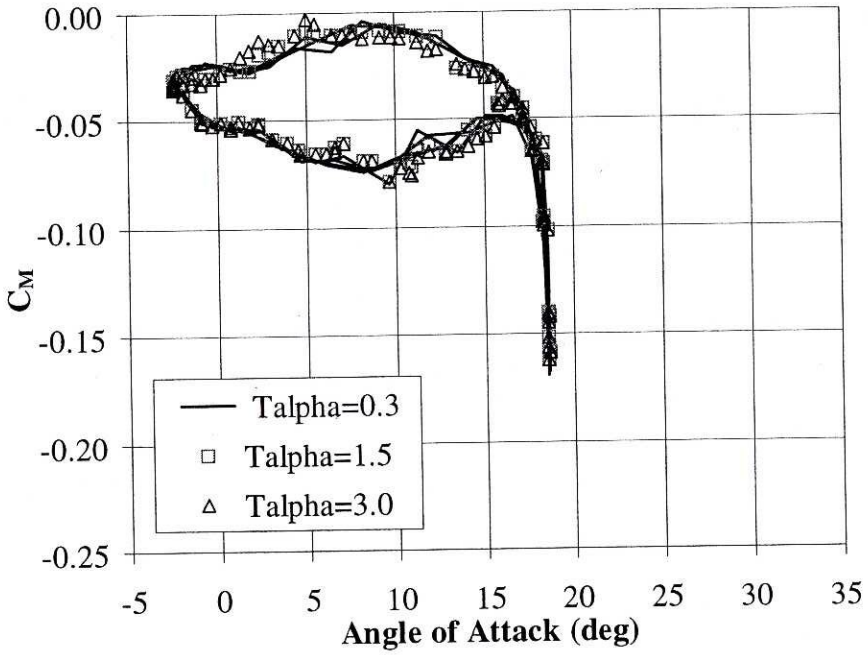

Figure 3.3: Moment coefficient versus angle of attack for a NASA LS(1)-0417 (k=0.077) airfoil with different T_α values.

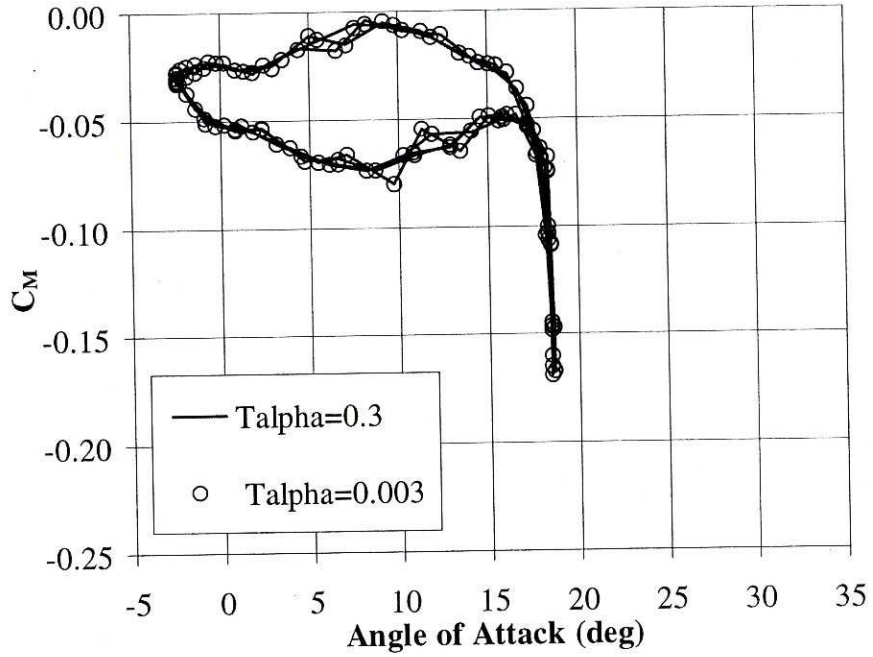

Figure 3.4: Moment coefficient versus angle of attack for a NASA LS(1)-0417 (k=0.077) airfoil with different T_α values.

a T_α of 0.3 should give reasonable predicted results of C_M values for this wind turbine and others operating with k less than 0.1. However, if analyzing data that are at a higher reduced frequency, T_α may have to be adjusted in order to reflect this change.

T_v

T_v is the time constant that controls the strength of the vortex. Figure 3.5 illustrates the effect of increasing the value of T_v from its standard value of 6 to 9 and 12. The strength of the vortex changes considerably from a minimum of –0.33 (with $T_v = 6$) to –0.44 (with $T_v = 12$). For this particular test condition, $T_v = 12$ gives the closest representation of the test data. However, other test cases show 6 to be better than 12. Figure 3.5 clearly illustrates that increasing T_v increases the effect of the vortex. This, in turn, increases the nose down pitching moment coefficient (i.e., C_M becomes more negative) when the vortex is at or near the trailing edge of the airfoil.

T_{vl}

T_{vl} is the nondimensional time of transit for the vortex moving across the airfoil surface. T_{vl} is equal to a constant value of 11.0. Figure 3.6 illustrates the effect that this time constant has on the DynStall prediction of C_M. When the T_{vl} value is equal to 5, the vortex moves quickly across the airfoil. It builds quickly, has the same magnitude (as the 11 and 15 simulations), and dissipates quickly. As the value of T_{vl} becomes higher, the vortex moves more slowly and has a more lasting effect. Figure 3.6 shows that when T_{vl} is 5, the vortex detaches at 19 degrees, the maximum nose down pitching moment coefficient is at 23 degrees and the vortex effect is gone at a 25 degree angle of attack. On the other hand, when T_{vl} is equal to 15, the vortex detaches at 20 degrees, the

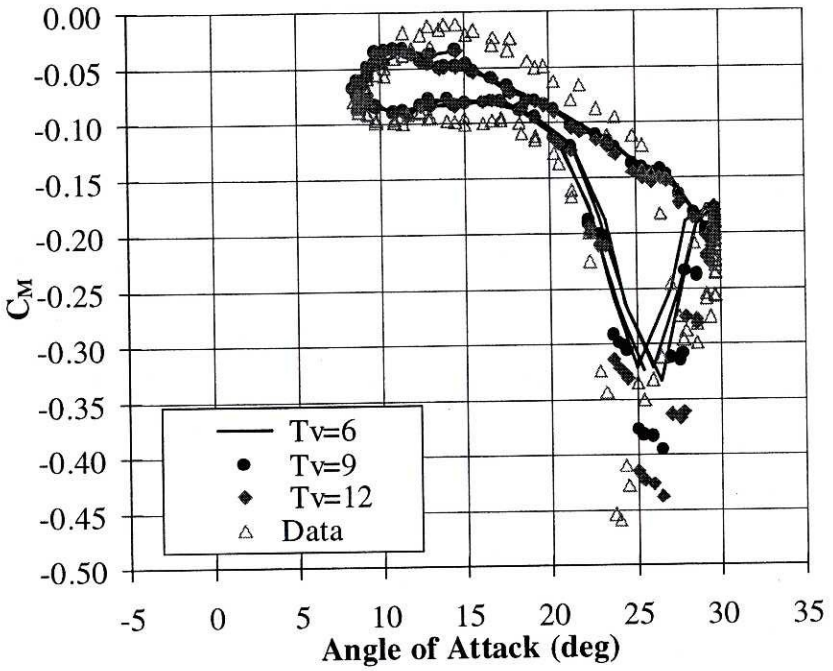

Figure 3.5: NASA LS(1)-0417 moment coefficient versus angle of attack. $\alpha=20+10\sin\omega t$, $k=0.081$, $Re=1.0\times10^6$. The effect that Tv has on the simulated values of C_M.

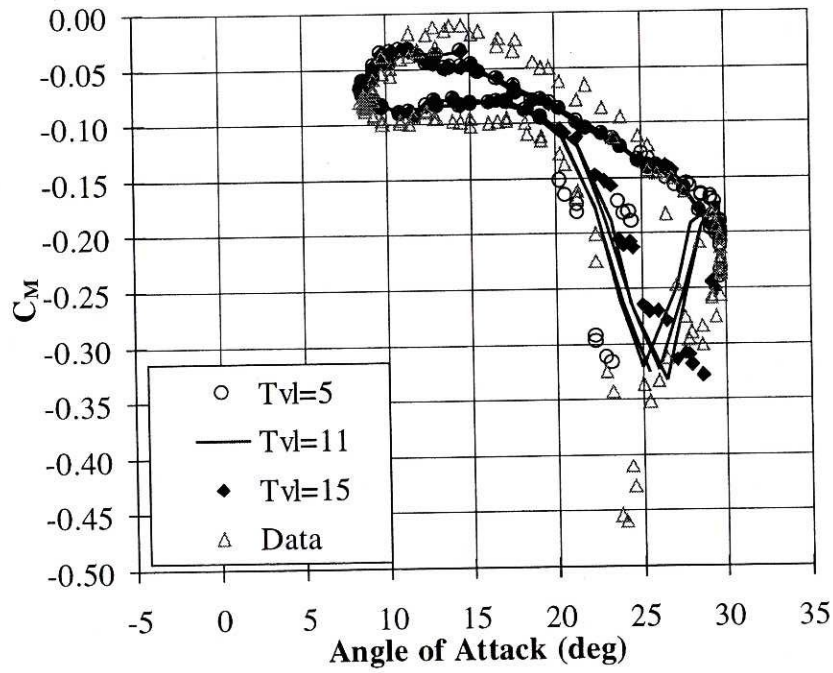

Figure 3.6: NASA LS(1)-0417 moment coefficient versus angle of attack.
$\alpha=20+10\sin\omega t$, $k=0.081$, $Re=1.0\times10^6$.
The effect that Tvl has on the simulated values of C_M.

maximum nose down pitching moment coefficient is at 28 degrees and the vortex effect remains until a 30 degree angle of attack is reached. In fact, in this case it would have remained longer if the airfoil had reached a higher of attack during the test.

TWO-DIMENSIONAL WIND TUNNEL DATA

SIMULATION RESULTS

This chapter compares pitching moment coefficients from two-dimensional (2-D) dynamic wind tunnel data (obtained from Gregorek and Reuss, 1994) to C_M's from the DynStall computer program. DynStall (see Appendix A) utilizes the AeroDyn subroutines and requires static airfoil data as well as a time history of wind velocity, V and angle of attack, α, values (identical to the dynamic wind tunnel data) as inputs. Comparisons were conducted on three airfoils at three reduced frequencies operating under 3 angle of attack ranges and two Reynolds numbers for a total of 54 comparisons.

OSU (Gregorek and Reuss, 1994) conducted wind tunnel tests on three different airfoils that are commonly used for wind turbine applications: NACA 4415, NASA LS(1)-0417 and the NREL S809. Figure 4.1 illustrates the general shapes of these airfoils. The tests were done at static conditions over a range of angles of attack from -20 to 40 degrees (except when noted otherwise) and under dynamic conditions with reduced frequencies from approximately 0.02 to 0.10.

The airfoil analyses that follow pertain to smooth airfoils operating at a Reynolds number of approximately one million. Comparisons at Reynolds numbers of 1.5 million are in Appendix C. All comparisons are calculated as outlined in the Methods section and incorporate the time constants listed under Minnema in Table 3.1. In order to

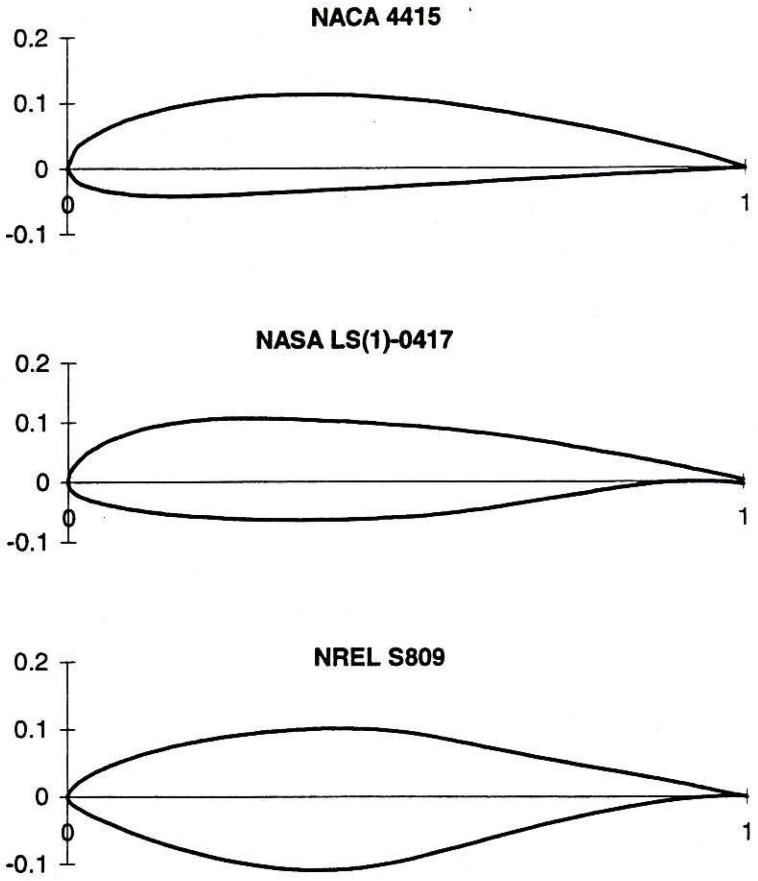

Figure 4.1: Airfoils used for unsteady aerodynamic C_M comparisons, from Pierce (1996).

facilitate comparisons, all plots use a C_M scale from –0.25 to 0.00 or –0.50 to 0.00 (unless a wider range is necessary). All plots use angle of attack scales from –5 to 35 degrees.

NACA 4415 Airfoil

Figures 4.2-4.10 compare the predicted and measured C_M for the NACA 4415 airfoil. Three angle of attack ranges were analyzed: $8+3.5\sin\omega t$, $14+10\sin\omega t$ and $20+10\sin\omega t$ degrees. Each was analyzed at three different reduced frequencies. These reduced frequencies were approximately 0.03, 0.06 and 0.09. Therefore, there are a total of nine data sets that are compared to model predictions.

The following comment made by Pierce (1996) with respect to simulating the lift and drag coefficients also holds true for the moment coefficient: "Multiple lines occur in the predictions since the measured angle of attack from the data were used as input to the Beddoes subroutines." These subroutines, written in FORTRAN, are part of the DynStall program in Appendix A. "The measured angle of attack does not follow an exact sine wave, and the measurements are somewhat sparse resulting in the multiple prediction lines." This phenomenon is illustrated later in this section for the case of $\alpha=14+10\sin\omega t$ at $k=0.086$.

For the cases with a mean angle of attack of 8 degrees (Figures 4.2-4.4), both the magnitudes and shapes of the simulated curves accurately represent the data. The angle of attack does not get large enough for a vortex to form during any of these simulations. Nearly the entire dynamic value of C_M is due to the circulatory and non-circulatory components (i.e., C_{MF}). The case of the reduced frequency being 0.089 (Figure 4.4) is the poorest representation of the three cases. It underpredicts the nose down pitching

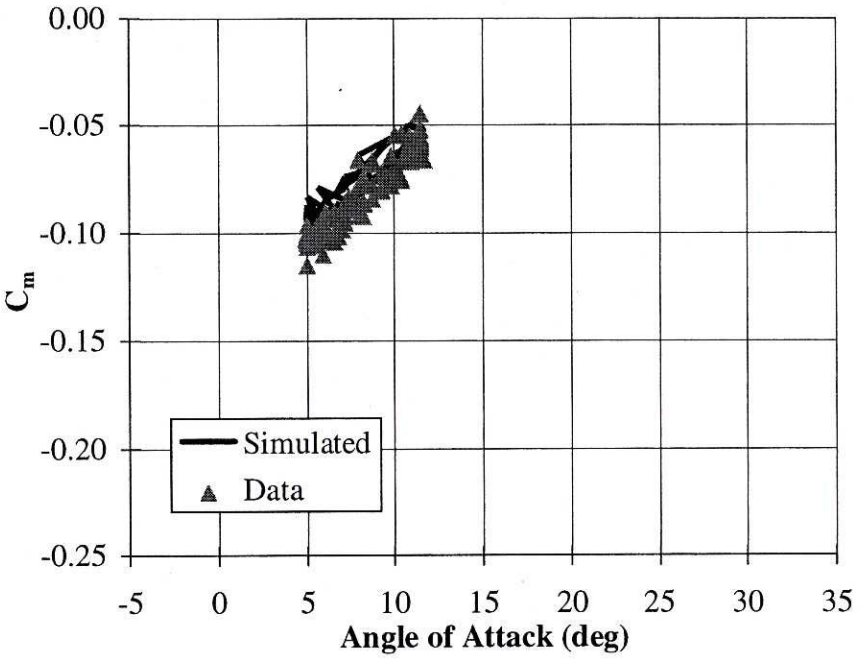

Figure 4.2: NACA 4415 moment coefficient versus angle of attack.
$\alpha=8+3.5\sin\omega t$, k=0.029, Re=1.0x10^6.

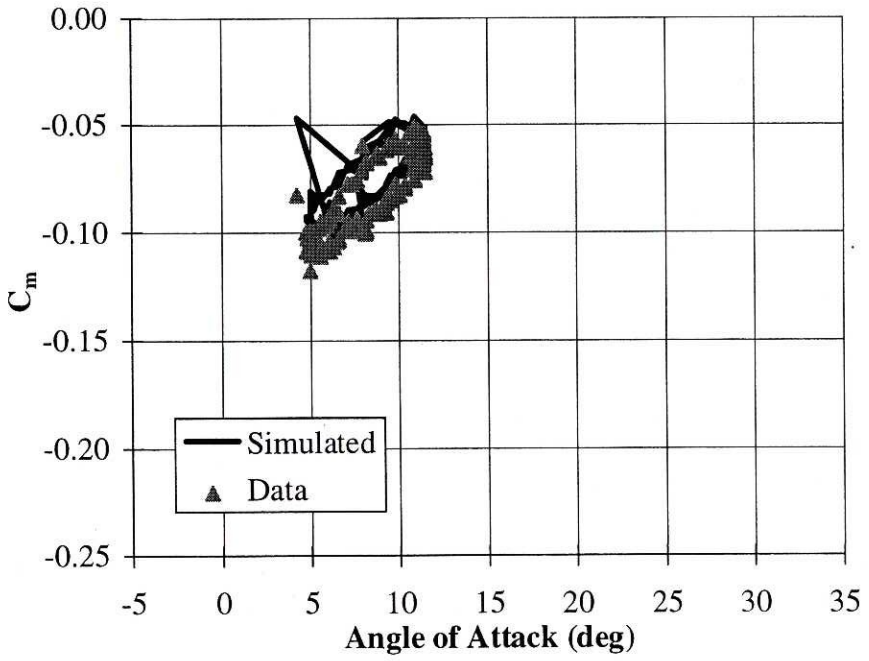

Figure 4.3: NACA 4415 moment coefficient versus angle of attack.
$\alpha=8+3.5\sin\omega t$, k=0.059, Re=1.0x10^6.

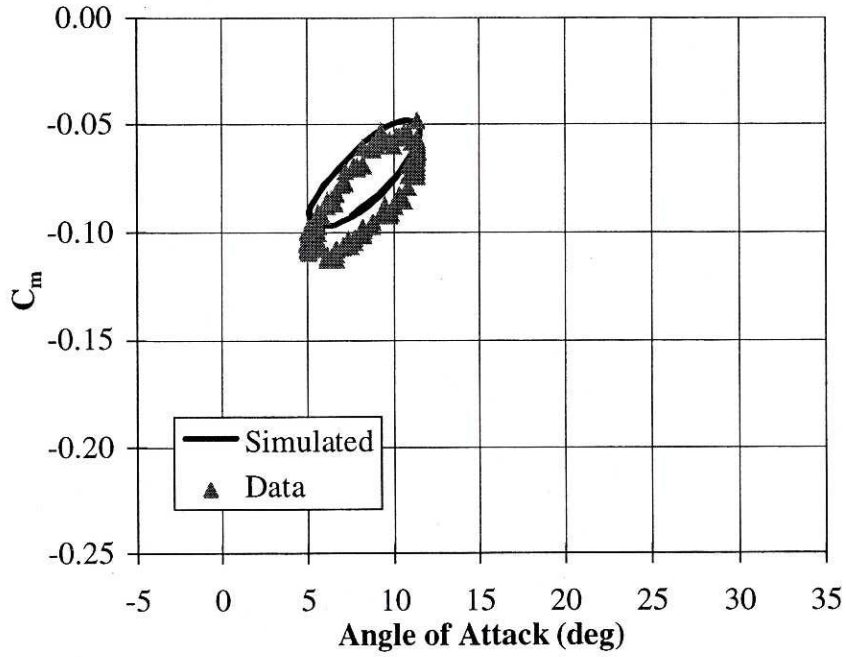

Figure 4.4: NACA 4415 moment coefficient versus angle of attack. $\alpha=8+3.5\sin\omega t$, k=0.089, Re=1.0x10^6.

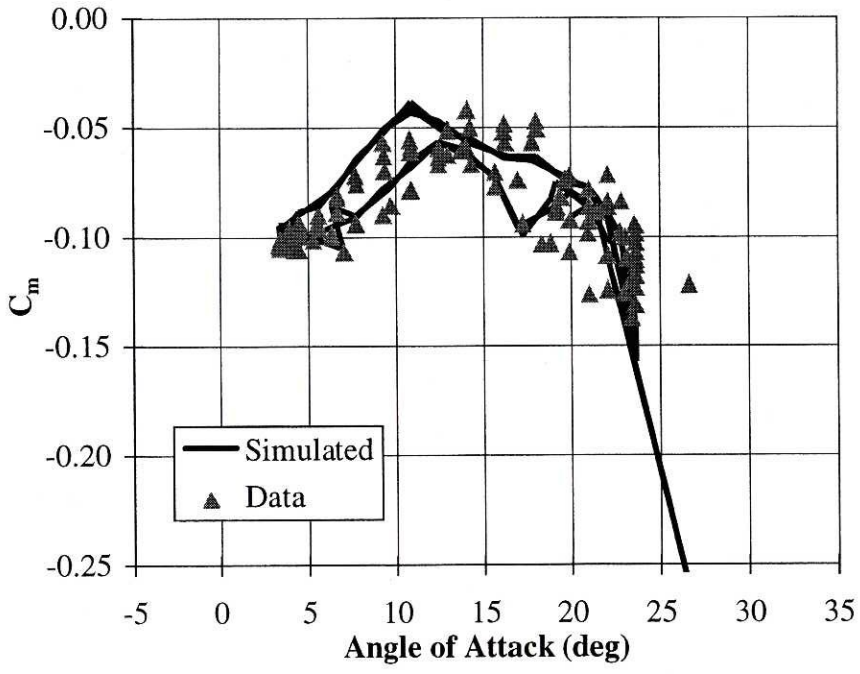

Figure 4.5: NACA 4415 moment coefficient versus angle of attack. $\alpha=14+10\sin\omega t$, k=0.029, Re=1.0x10^6.

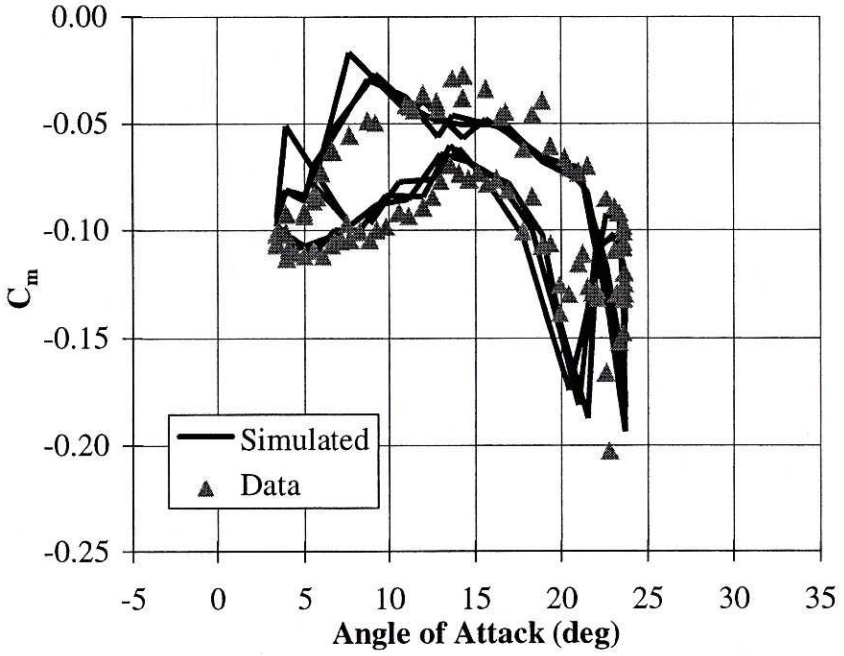

Figure 4.6: NACA 4415 moment coefficient versus angle of attack. $\alpha=14+10\sin\omega t$, k=0.056, Re=1.0x10^6.

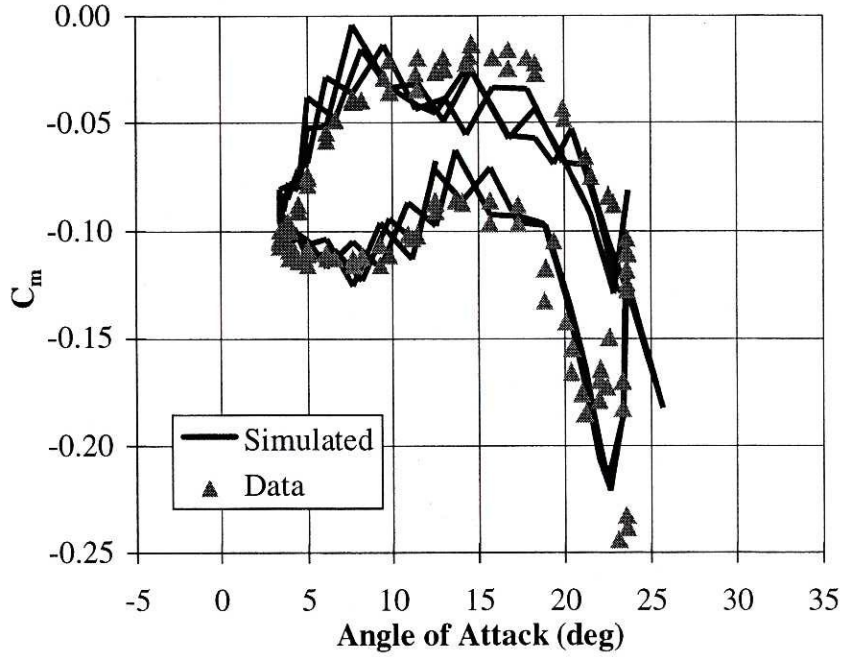

Figure 4.7: NACA 4415 moment coefficient versus angle of attack. $\alpha=14+10\sin\omega t$, k=0.086, Re=1.0x10^6.

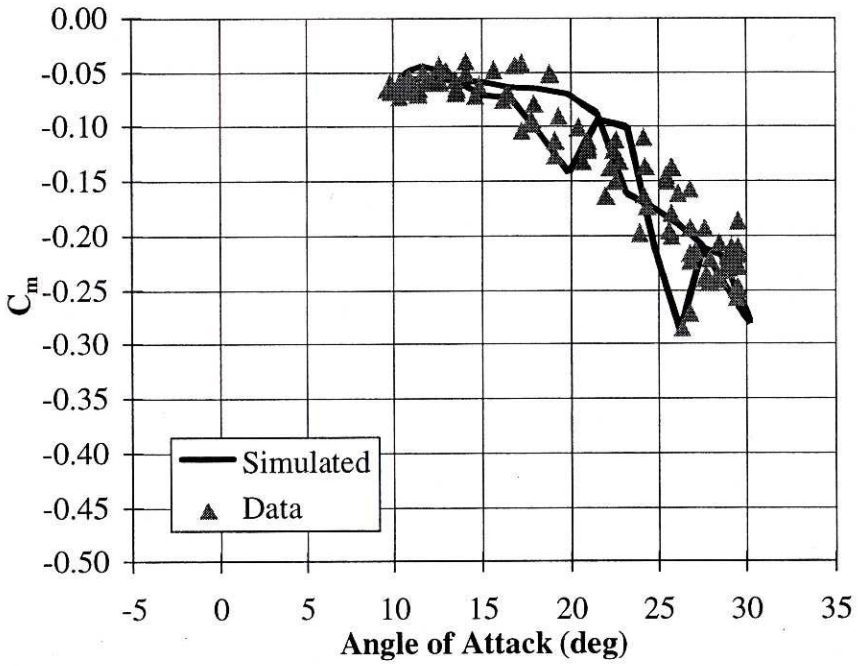

Figure 4.8: NACA 4415 moment coefficient versus angle of attack. $\alpha=20+10\sin\omega t$, k=0.031, Re=0.9x10^6.

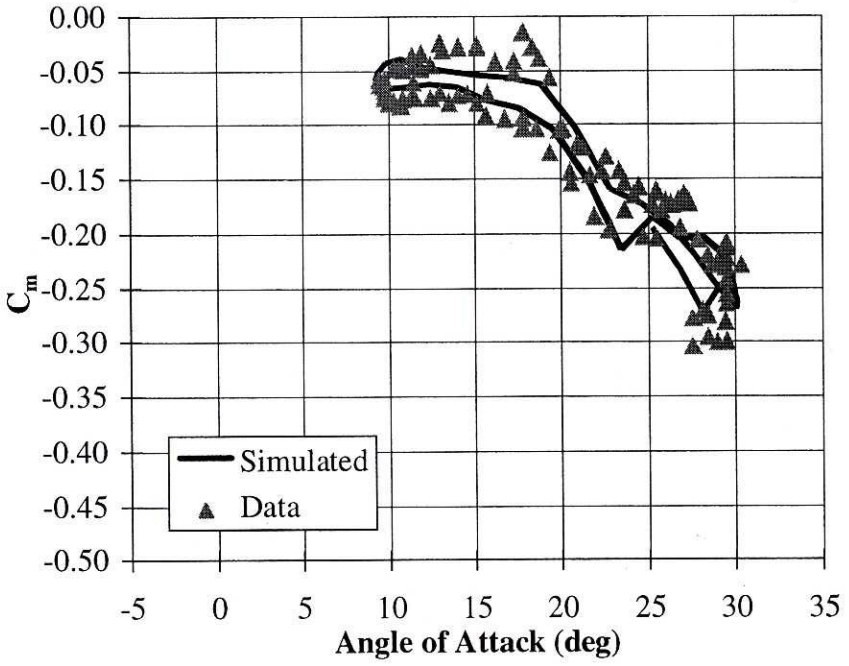

Figure 4.9: NACA 4415 moment coefficient versus angle of attack. $\alpha=20+10\sin\omega t$, k=0.064, Re=0.9x10^6.

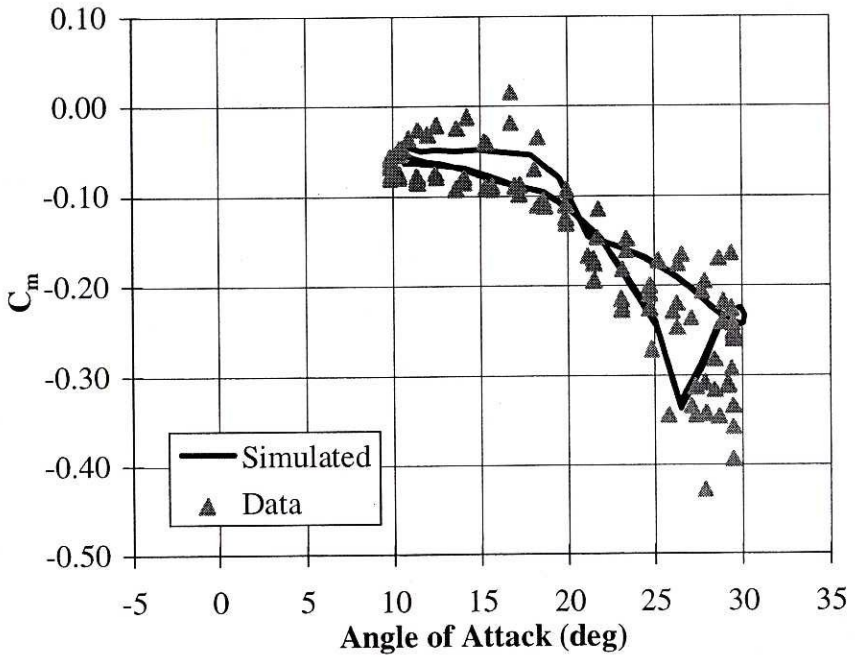

Figure 4.10: NACA 4415 moment coefficient versus angle of attack. $\alpha=20+10\sin\omega t$, k=0.096, $Re=0.9x10^6$.

moment by as much as 0.03. Note that there is a wayward data point on Figure 4.3. This is likely due to an angle of attack instrumentation error that occurred while the data were recorded.

When the mean angle of attack is increased to 14 degrees and the amplitude increased to 10 degrees, the vortex begins to influence $C_{M.}$. Figure 4.5 represents the case where k=0.029. The simulation accurately represents the data throughout the cycle (except for the wayward point at 27 degrees). The simulation bisects the jittery data as the angle of attack increases from 4 degrees up to the point were the first vortex detaches at 16 degrees. The simulation approximates the static data until a weak secondary vortex develops at 22 degrees and is shed at the maximum angle of attack, 24 degrees. As the airfoil pitches back to its minimum angle of attack, the model underpredicts the pitching moment coefficient until the pitch is 14 degrees. From this point back to the minimum value of 4 degrees the simulation agrees well with the data. The simulation predicts the maximum and minimum C_M values very closely. It is difficult in this case, and in some of the cases that follow, to know how accurate the simulation is because the data are scattered and inconsistent.

Figure 4.6 predicts all events from 4 degrees up to the onset of the vortex contribution at 16 degrees and to the point were the vortex reaches the trailing edge of the airfoil at 22 degrees. The simulation then produces a fast secondary vortex that starts at 23 degrees and ends at the maximum angle of attack, 24 degrees. It is difficult to determine how the data are responding at these high angles of attack since it is not consistent with each cycle.

Figure 4.7 has one vortex contributing to the pitching moment coefficient. It begins to build at 16 degrees, reaches the trailing edge at 22 degrees and is shed as the airfoil begins to reverse its angle of attack at 24 degrees. The simulation is especially jittery in Figure 4.7. As mentioned earlier, this is because the angle of attack does not follow an exact sine wave over time.

Figure 4.11 illustrates the angle of attack versus time history for this case as well as for the case of a perfect sine wave. It is evident from this figure that the data are erratic and that there is also a wayward data point at 0.5 seconds and 26 degrees. Of the four components that are summed to equal C_M, C_{MI} is most sensitive to unsteady sine wave input. Figure 4.12 illustrates this effect by comparing C_{MI} values when using the data input versus the sinusoidal input. Figure 4.13 shows the simulated C_M curve when using the data input versus the sinusoidal input. The sinusoidal input is smooth and repeats for each of the three cycles that are simulated.

Figures 4.8 through 4.10 are for the case of a mean angle of attack of 20 degrees and 10 degrees of oscillation. Although the data are jittery for these three cases, the simulations represent them well. Figure 4.8 has a primary vortex forming at 17 degrees, reaching the trailing edge at 20 degrees and dissolving at 22 degrees. A secondary vortex commences at 23 degrees, reaches the trailing edge at 26 degrees and is fully separated at 27 degrees. The C_M values then return to the separated flow values (which are close to the static values) until the maximum angle of attack is reached at 30 degrees. They continue to be at the separated flow values all the way back to the minimum angle of attack of 10 degrees.

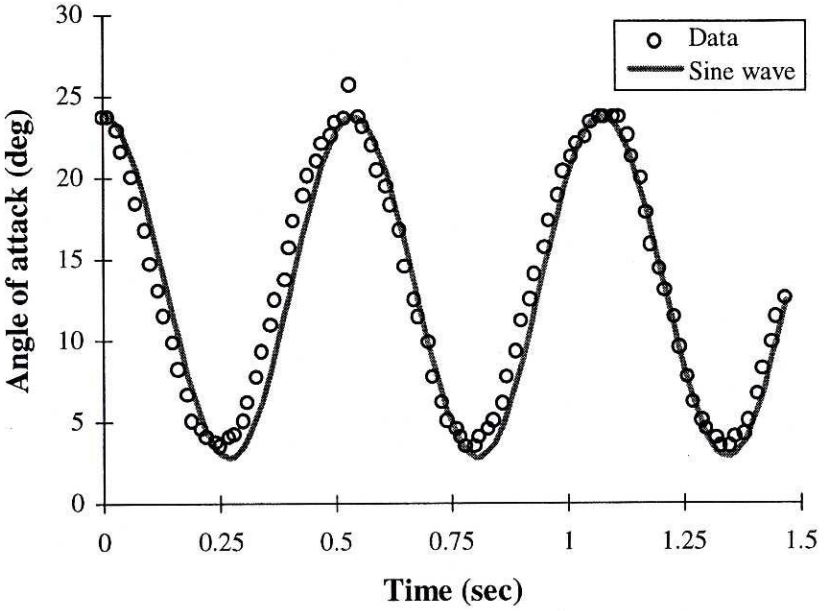

Figure 4.11: NACA 4415 angle of attack versus time.
Comparison of the data to a sine wave.

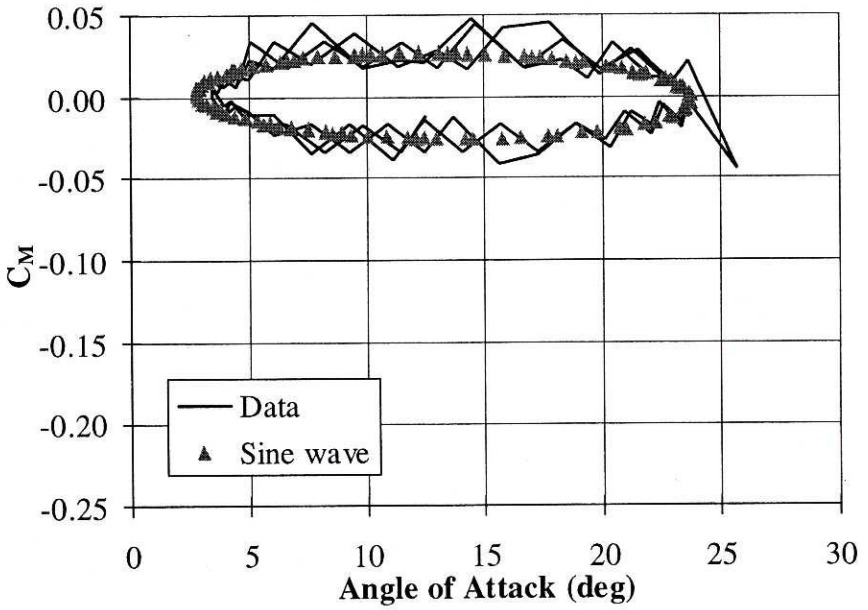

Figure 4.12: NACA 4415 moment coefficient versus angle of attack.
Comparison of the predicted C_{MI} using measured angles of attack and sine wave angles of attack.

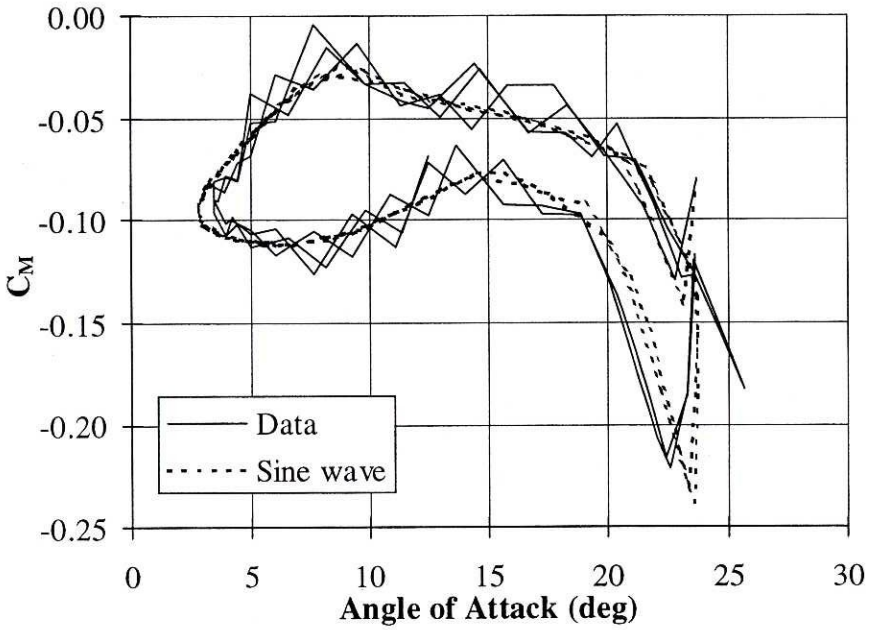

Figure 4.13: NACA 4415 moment coefficient versus angle of attack. Comparison of the predicted C_M using measured α data and sine wave α.

Figure 4.9 also contains contributions from two vortices. The primary vortex begins to build at 17 degrees, reaches the trailing edge at 23 degrees and is fully separated at 28 degrees. The secondary vortex commences at 25 degrees, reaches the trailing edge at 27 degrees and is gone at 30 degrees. Thus, both vortices contribute to the pitching moment coefficient when the angle of attack is between 25 degrees and 28 degrees. The primary vortex is decaying while the secondary vortex is building.

Figure 4.10 is similar to the previous two figures except it contains only one vortex. This vortex is stronger and stays on the airfoil over a greater range of angles of attack. The vortex contribution begins at 17 degrees, is a maximum at 26 degrees and is fully gone at 30 degrees. This simulation does not represent the data as accurately as the previous two figures. However, the data in Figure 4.10 do not repeat well over the three cycles, especially in the range of angle of attacks from 25 to 30 degrees.

NASA LS(1)-0417 Airfoil

Figures 4.14 through 4.22 compare predicted to measured values of C_M for the NASA LS(1)-0417 airfoil during dynamic conditions. The comparisons were made at three different mean angles of attack: 8 degrees, 14 degrees and 20 degrees with an amplitude of oscillation of 10 degrees. Each of the three aforementioned oscillatory cases was analyzed at three different reduced frequencies: 0.03, 0.06 and 0.09, resulting in nine different comparisons.

For a mean angle of attack of 8 degrees the results are impressive. The simulated C_M values are mainly composed of the separated flow values except at the higher angles of attack where the vortex contributes greatly. Figures 4.14 and 4.15 represent the data at reduced frequencies of 0.026 and 0.052 respectively. As the angle of attack of the airfoil

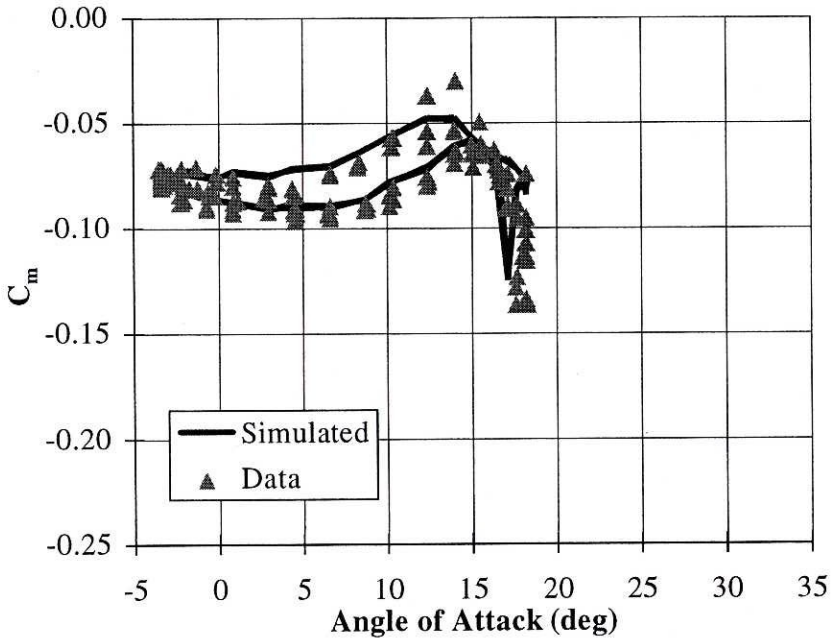

Figure 4.14: NASA LS(1)-0417 moment coefficient versus angle of attack. $\alpha=8+10\sin\omega t$, k=0.026, Re=1.0x10^6.

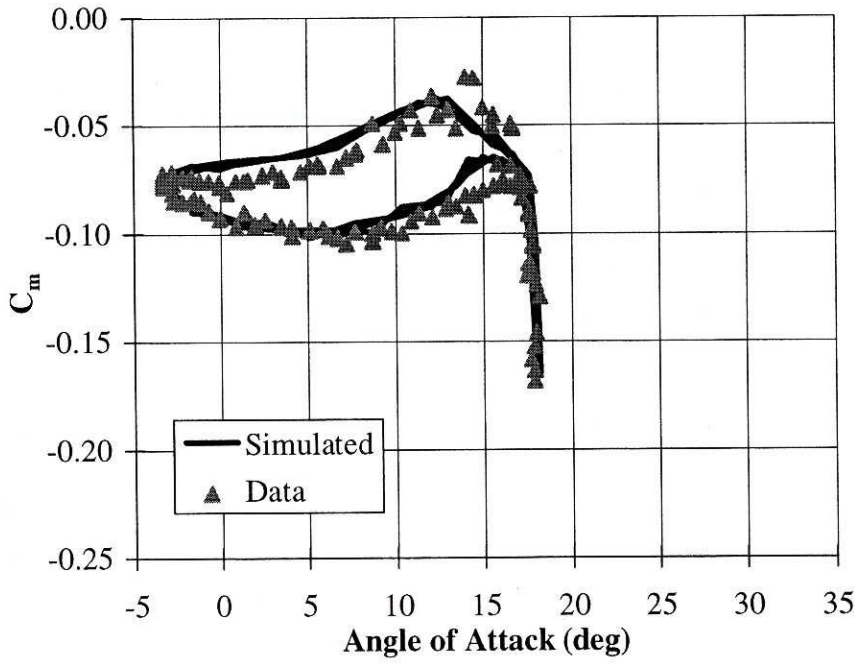

Figure 4.15: NASA LS(1)-0417 moment coefficient versus angle of attack. $\alpha=8+10\sin\omega t$, k=0.052, Re=1.0x10^6.

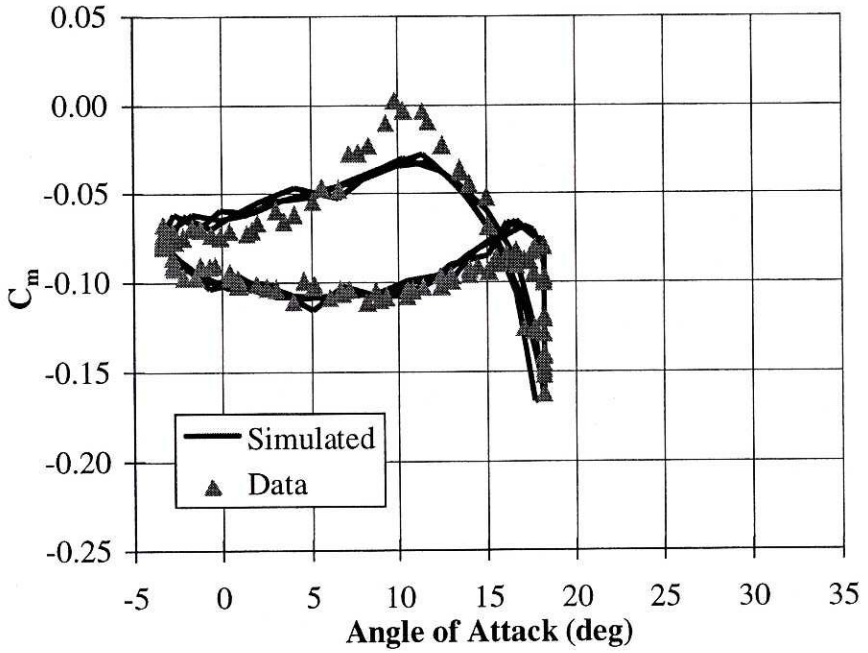

Figure 4.16: NASA LS(1)-0417 moment coefficient versus angle of attack. $\alpha=8+10\sin\omega t$, $k=0.082$, $Re=1.0\times10^6$.

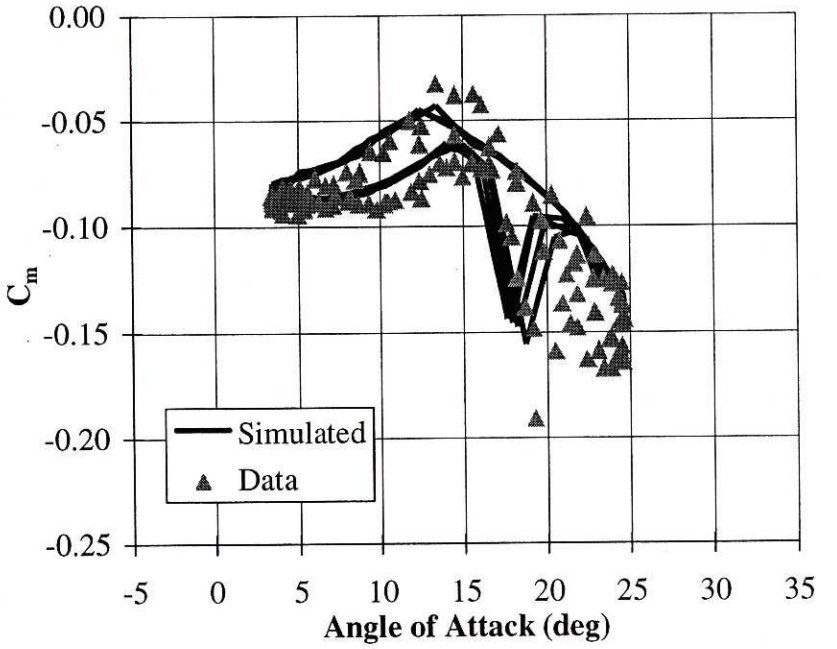

Figure 4.17: NASA LS(1)-0417 moment coefficient versus angle of attack. $\alpha=14+10\sin\omega t$, $k=0.026$, $Re=1.0\times10^6$.

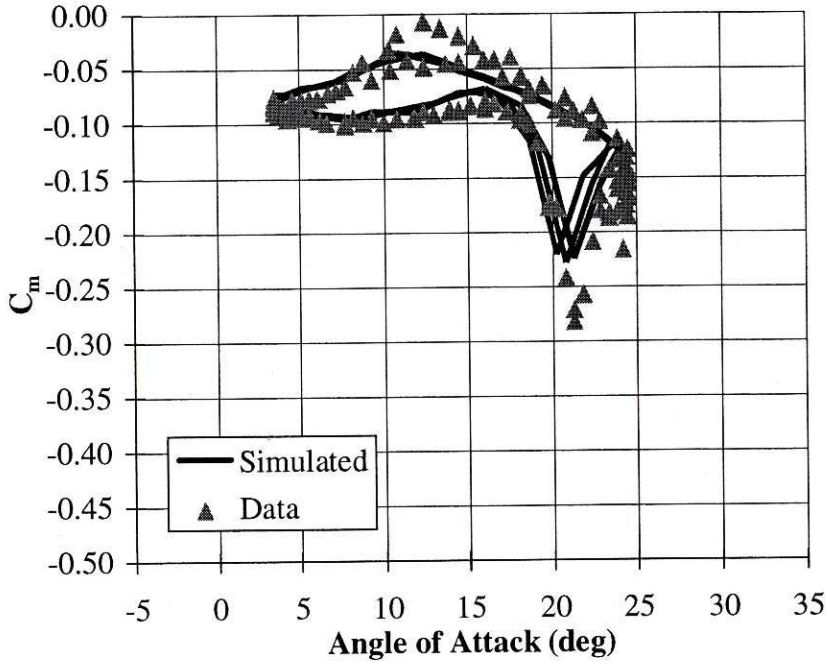

Figure 4.18: NASA LS(1)-0417 moment coefficient versus angle of attack. $\alpha=14+10\sin\omega t$, k=0.052, Re=1.0x10^6.

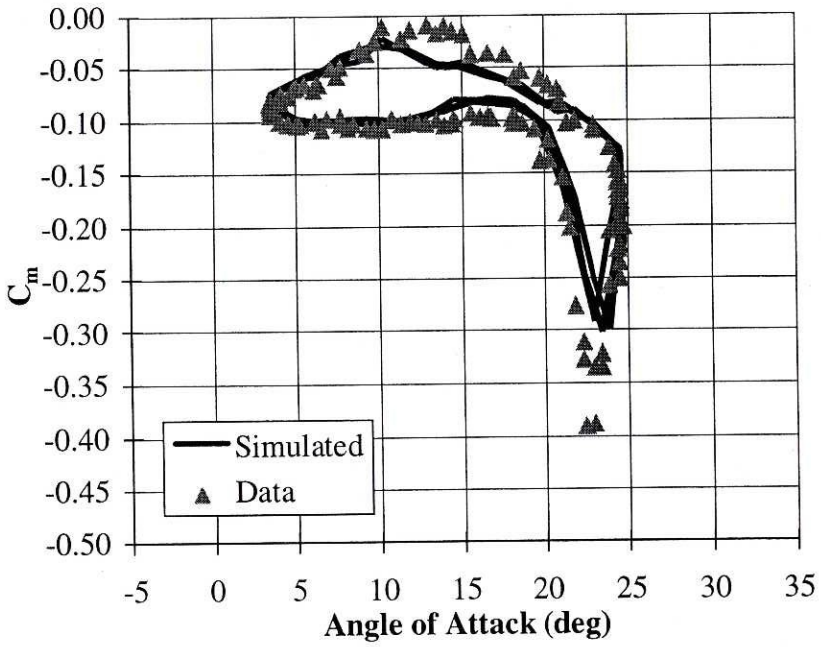

Figure 4.19: NASA LS(1)-0417 moment coefficient versus angle of attack. $\alpha=14+10\sin\omega t$, k=0.079, Re=1.0x10^6.

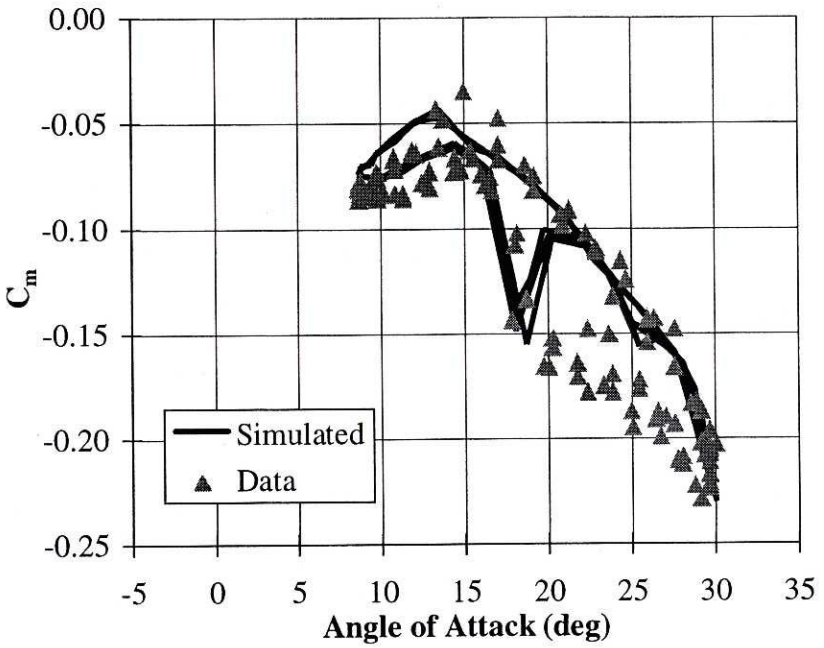

Figure 4.20: NASA LS(1)-0417 moment coefficient versus angle of attack. $\alpha=20+10\sin\omega t$, k=0.027, Re=1.0×10^6.

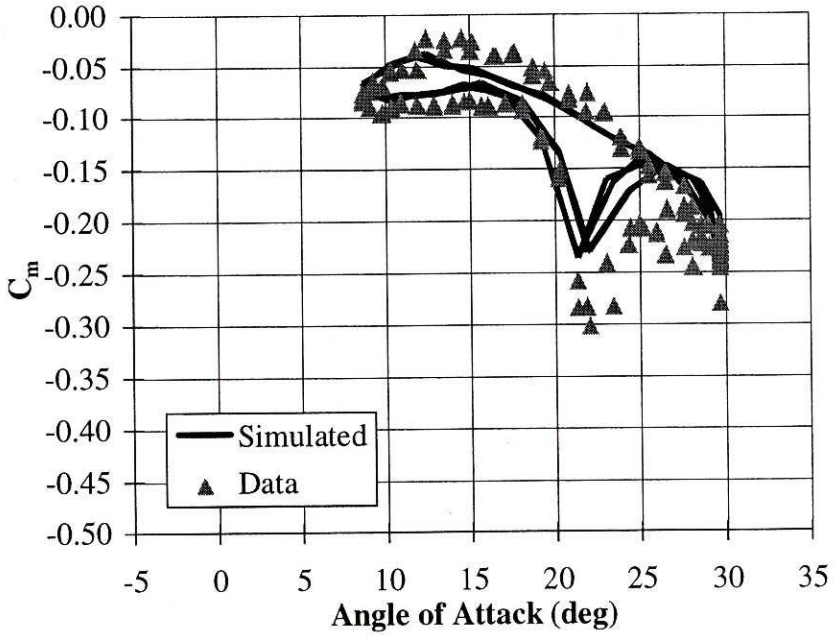

Figure 4.21: NASA LS(1)-0417 moment coefficient versus angle of attack. $\alpha=20+10\sin\omega t$, k=0.055, Re=1.0×10^6.

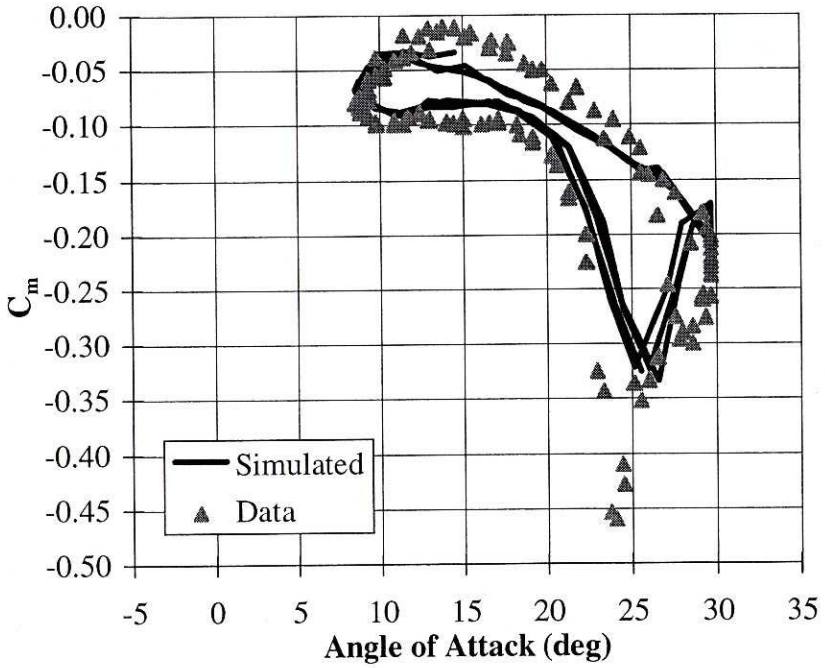

Figure 4.22: NASA LS(1)-0417 moment coefficient versus angle of attack. $\alpha=20+10\sin\omega t$, k=0.081, Re=1.0x10^6.

increases, the vortex begins to build at the leading edge when the maximum angle of attack (18 degrees) is reached. As the airfoil begins to move to a lower angle of attack, the vortex suddenly reaches the trailing edge and dissipates quickly. Directly after the effect of the vortex has disappeared (from approximately 16 degrees to 13 degrees), the model slightly overpredicts the nose down pitching moment. Figure 4.16 also does an excellent job of simulating the data, but also overpredicts the nose down C_M immediately after the effects of the vortex have passed (from 12 degrees to 7 degrees).

Although the simulations at a mean angle of attack of 14 degrees do not simulate the data as well as those previously discussed, they are still fairly good. The simulated prediction in Figure 4.17 does an excellent job of predicting the data from 4 degrees until the primary vortex reaches the trailing edge of the airfoil at 18 degrees. Because the data points are very scattered at angles of attack greater than 20 degrees, it is difficult to determine how accurately the simulation is at these high angle of attacks. The simulation does duplicate the data well as the angle of attack decreases from its maximum value of 24 degrees to its minimum value of 4 degrees. As the reduced frequency is increased to 0.052 and 0.079 in Figures 4.18 and 4.19, the data become more repeatable. The simulations for these two cases are very similar. They both accurately represent the data except they underpredict the maximum magnitude of the vortex. Figure 4.18 predicts a maximum nose down C_M of -0.23 whereas the data indicate -0.28. Figure 4.19 predicts a maximum nose down C_M of -0.30 whereas the data indicate -0.39.

Figures 4.20 through 4.22 represent cases for a mean angle of attack is 20 degrees. When the reduced frequency is 0.027 (Figure 4.20), the data underpredicts the nose down pitching moment from the minimum angle of attack at 9 degrees until the

primary vortex begins to detach from the airfoil at 17 degrees. The simulation predicts the beginning stages of the vortex contribution well. However, the simulation shows the primary vortex fully separating at 20 degrees and two very minor vortices (each having contributions of less than 0.02) occurring before reaching the maximum angle of attack at 30 degrees. The data, on the other hand, show values approximately 0.05 less than those of the simulation as the airfoil pitches from 20 to 30 degrees. When the reduced frequency is increased to 0.055 (Figure 4.21), the model performs well except it underpredicts the magnitude of the primary vortex contribution after it reaches the trailing edge of the airfoil by 0.05. The simulation also slightly overpredicts the data as the angle of attack decreases from 20 degrees to13 degrees. Figure 4.22 is similar to Figure 4.21 in that it also overpredicts the data as the angle of attack decreases. Figure 4.22 also underpredicts the nose down pitching moment. In this case, the maximum nose down C_M is off by 0.12. Because of this large discrepancy at the vortex peak, it was believed the simulation needed a finer time step in order to more closely represent the large contribution of the vortex. Hence, angle of attack versus time input information for this simulation was matched to a sine wave and the frequency of data points was approximately multiplied by four. This finer time step resulted in four times as many data points over the same time period. This resulted in nearly an identical simulation as is illustrated in Figure 4.23. Therefore, the finer time step had a minimal effect on the simulation and is does not account for underpredicting the strength of the vortex contribution at the trailing edge of the airfoil.

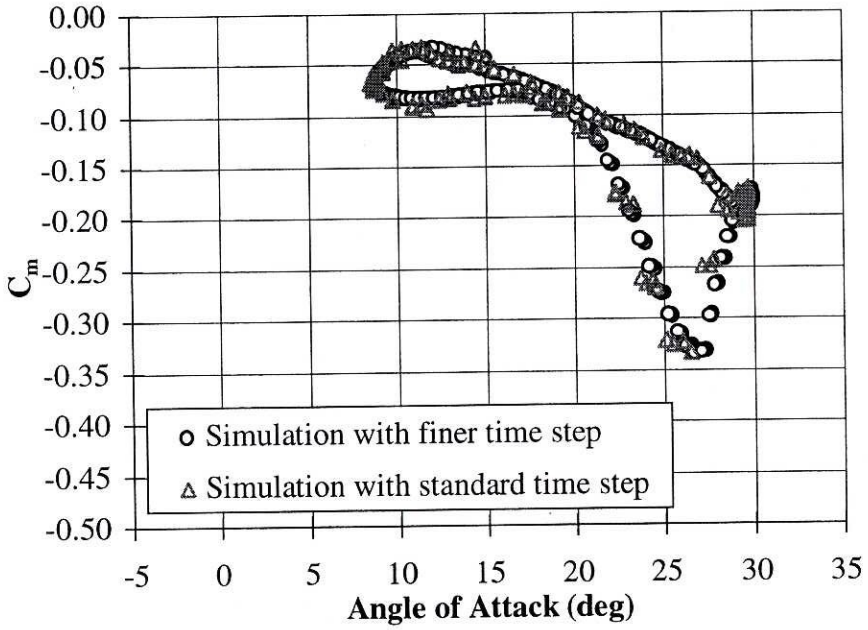

Figure 4.23: NASA LS(1)-0417 MOD moment coefficient versus angle of attack. The simulation shows virtually no difference with a finer time step.

NREL S809 Airfoil

Figures 4.24 through 4.32 compare predicted to measured values of C_M for the NREL S809 airfoil during dynamic conditions. The test conditions were similar to those for the NASA LS(1)-0417: comparisons were made at three different mean angles of attack: 8 degrees, 14 degrees and 20 degrees with an amplitude of oscillation of 10 degrees. Each of the three aforementioned oscillatory cases was analyzed at three different reduced frequencies: 0.03, 0.06 and 0.09, resulting in nine different comparisons.

For a mean angle of attack of 8 degrees, the results are fair. Figure 4.24 represents the case with the lowest reduced frequency, k = 0.026. This plot shows very little dynamic behavior and represents the data well except it underpredicts the nose down C_M prior to the vortex contribution by as much as 0.02. In addition, the simulation predicts a primary vortex (which peaks at 17 degrees) where the data show no vortex. For the higher reduced frequency cases (Figures 4.25 and 4.26), the simulations misrepresent the data in similar ways. They both do very well as the angle of attack is increased from -2 to 10 degrees. At 10 degrees, there appears to be a vortex contribution that reaches the trailing edge at 15 degrees. However, both the simulations show no vortex contribution until 16 degrees. The simulation also predicts that the vortex effect is stronger (by 0.03 to 0.05) than the data indicate. As the airfoil decreases in angle of attack from its maximum value of 18 degrees, the simulations are very accurate until about 15 degrees where both simulations overpredict the nose down C_M by as much as 0.03. The simulations become more accurate again as the airfoil pitches from 9 degrees back to the minimum angle of -3 degrees.

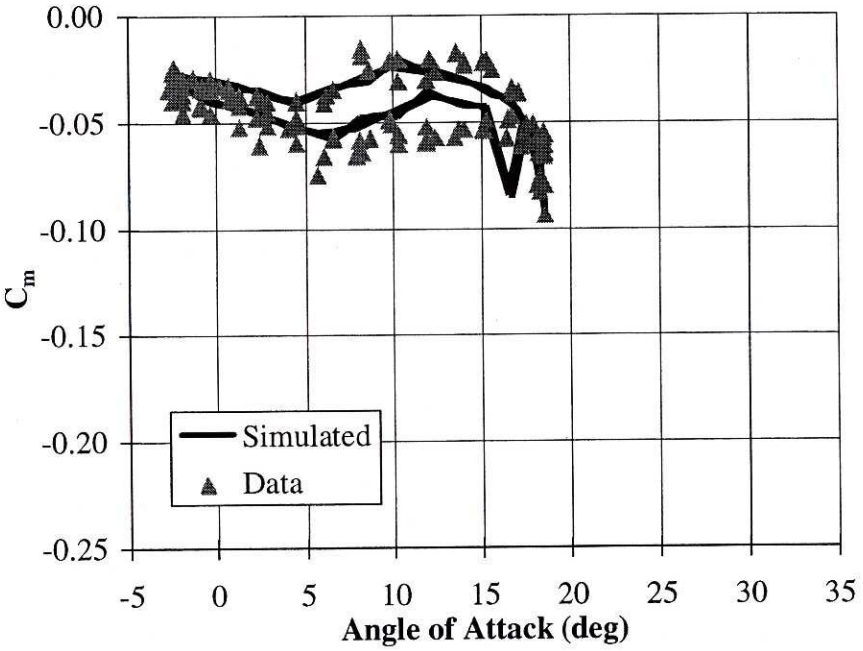

Figure 4.24: NREL S809 moment coefficient versus angle of attack. $\alpha=8+10\sin\omega t$, k=0.026, Re=1.0x10^6.

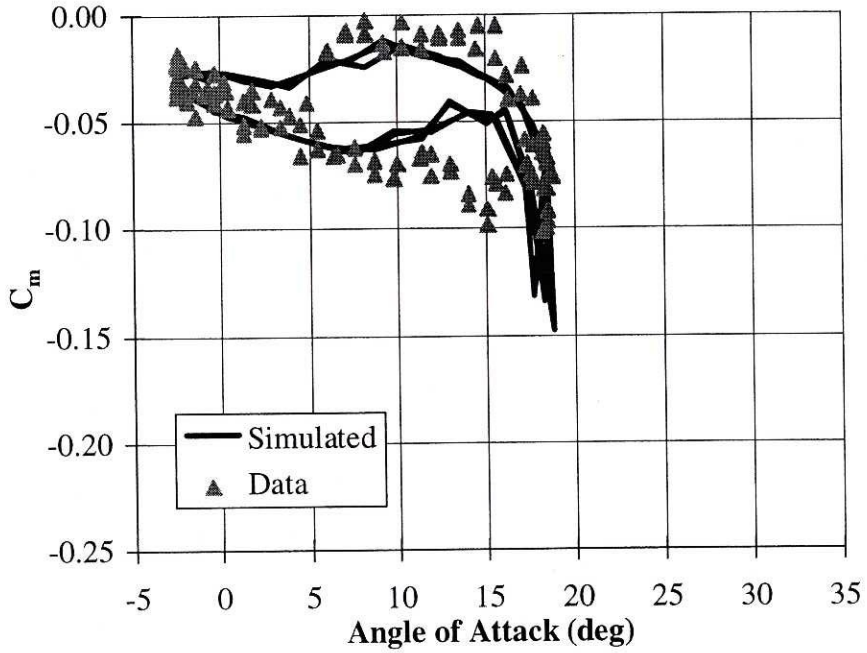

Figure 4.25: NREL S809 moment coefficient versus angle of attack. $\alpha=8+10\sin\omega t$, k=0.053, Re=1.0x10^6.

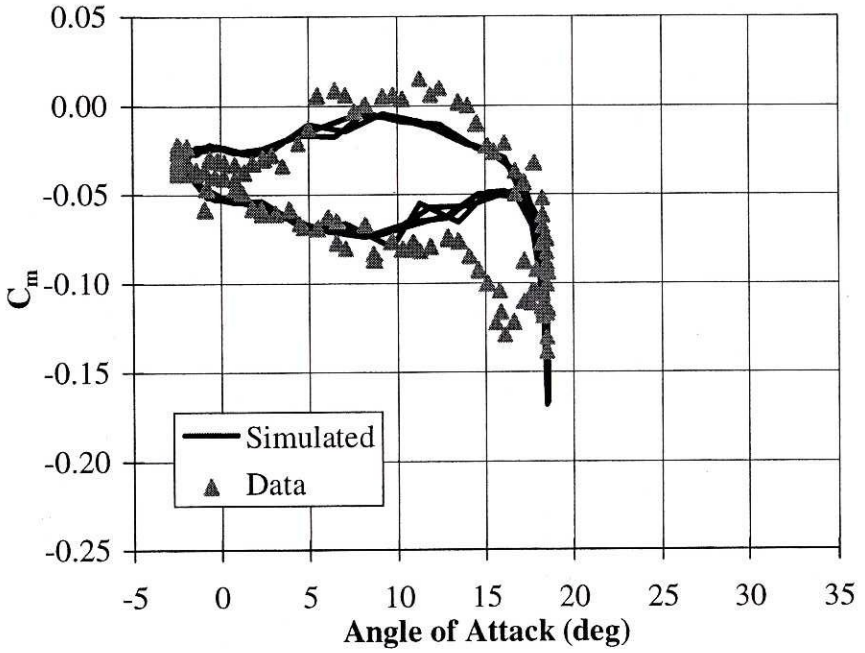

Figure 4.26: NREL S809 moment coefficient versus angle of attack. $\alpha=8+10\sin\omega t$, $k=0.077$, $Re=1.0\times10^6$.

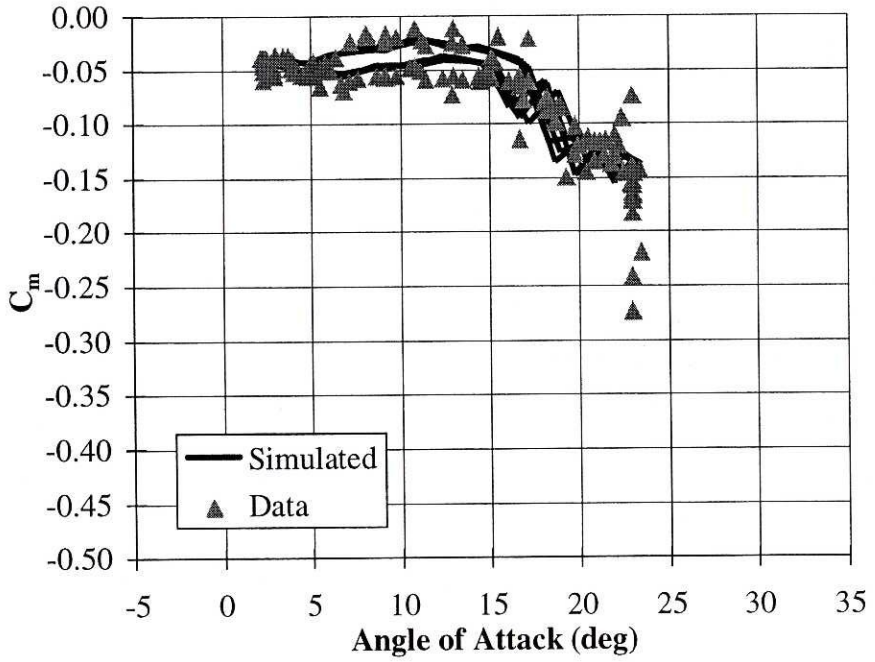

Figure 4.27: NREL S809 moment coefficient versus angle of attack. $\alpha=14+10\sin\omega t$, $k=0.026$, $Re=1.0\times10^6$.

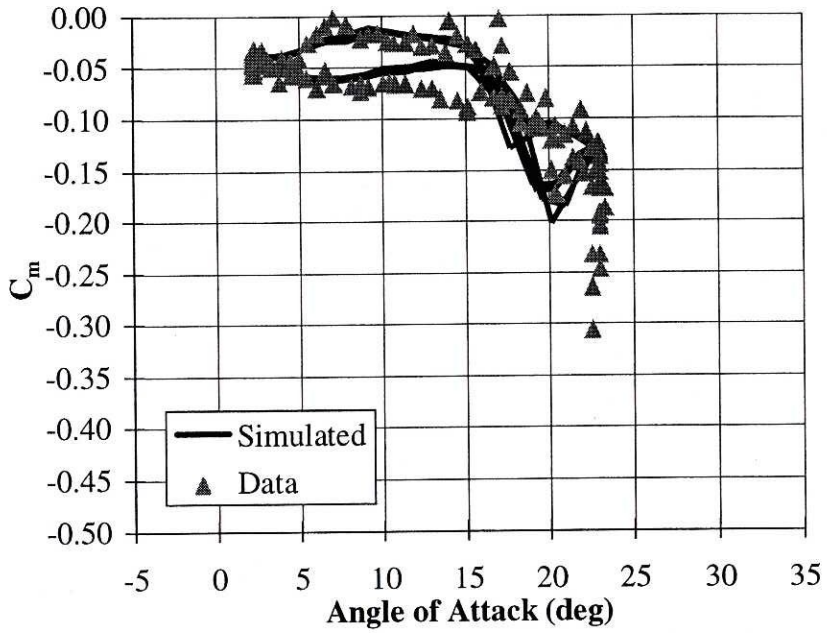

Figure 4.28: NREL S809 moment coefficient versus angle of attack. $\alpha=14+10\sin\omega t$, k=0.053, Re=1.0x10^6.

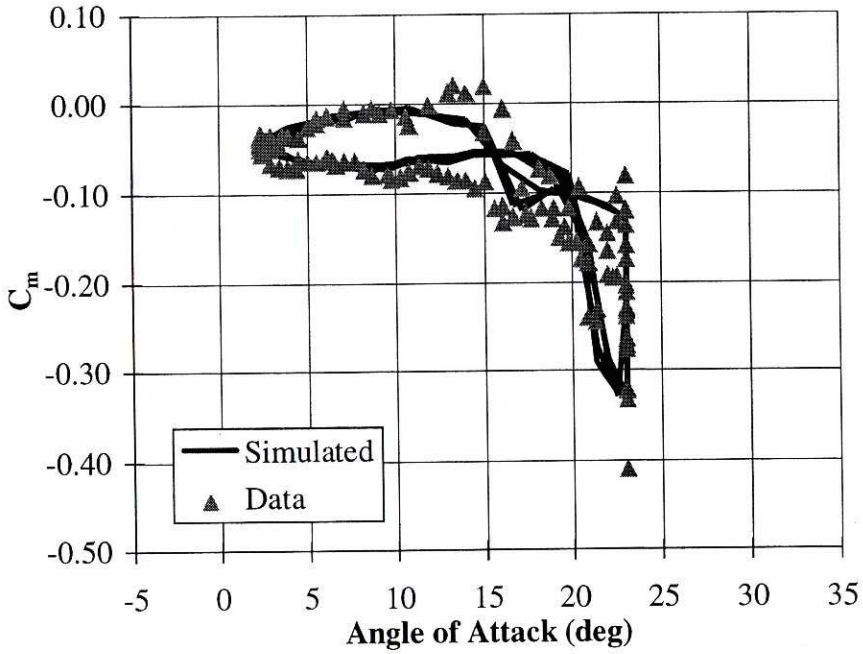

Figure 4.29: NREL S809 moment coefficient versus angle of attack. $\alpha=14+10\sin\omega t$, k=0.080, Re=1.0x10^6.

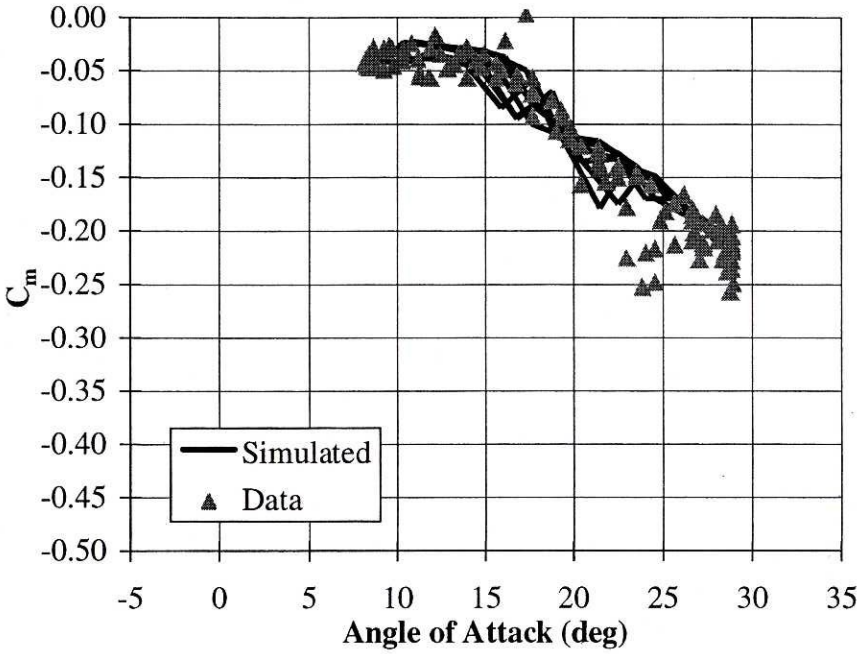

Figure 4.30: NREL S809 moment coefficient versus angle of attack. $\alpha=20+10\sin\omega t$, k=0.025, Re=1.0x10^6.

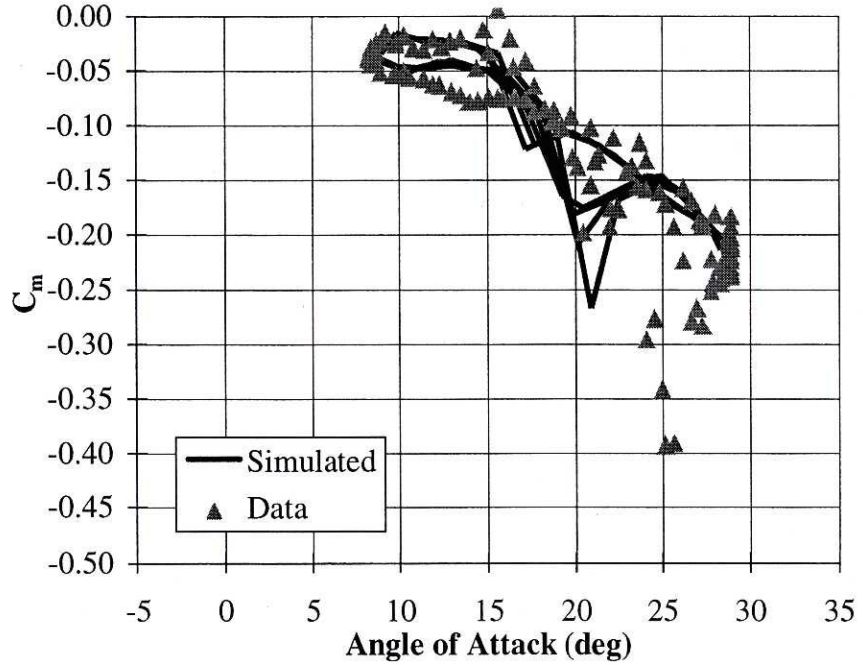

Figure 4.31: NREL S809 moment coefficient versus angle of attack. $\alpha=20+10\sin\omega t$, k=0.051, Re=1.0x10^6.

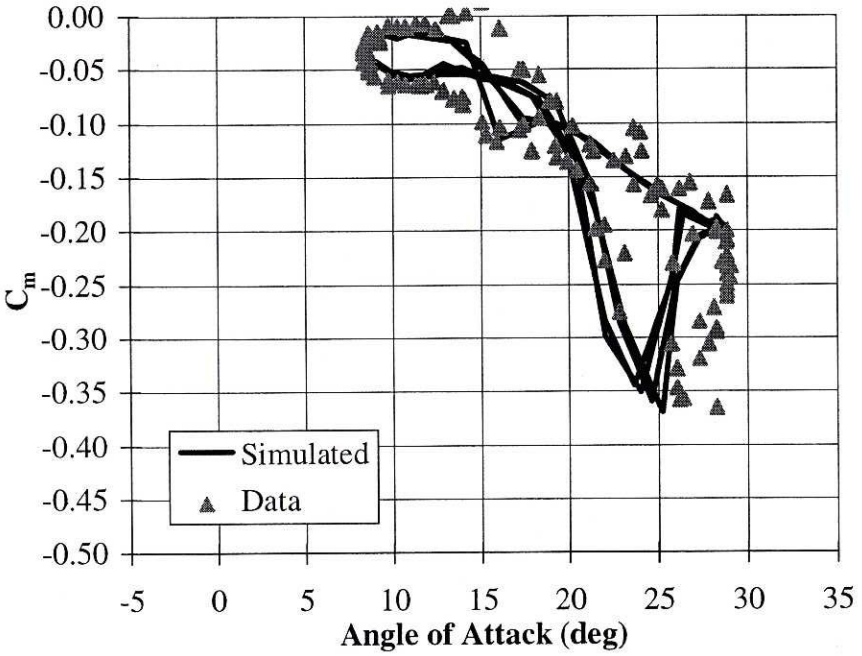

Figure 4.32: NREL S809 moment coefficient versus angle of attack. $\alpha=20+10\sin\omega t$, k=0.078, Re=1.0x10^6.

Figures 4.27 through 4.29 represent the cases where the mean angle of attack is 14 degrees. Figure 4.27 (with k = 0.026) does an excellent job of simulating the data except it is off by a maximum of 0.12 at the maximum angle of attack, 24 degrees. At this angle, the data show a large vortex contribution but the simulation shows none. Figure 4.28 begins well as the pitch moves from 3 degrees to 10o degrees. Beginning at 10 degrees, the data appear to display a small primary vortex that reaches the trailing edge at 15 degrees. The data display a secondary vortex that begins to build at 16 degrees, reaches the trailing edge of the airfoil at 20 degrees and is fully separated at 23 degrees. The simulation predicts this vortex very well. However, the simulation misses badly at 24 degrees where the data display a very large vortex contribution of 0.015, which separates quickly. Figure 4.29 is the best simulation for this mean angle of attack. The simulation is very good as the airfoil pitches from 3 degrees to 12 degrees. At 12 degrees, the data reveal vortex effects. However, the model does not display vortex effects until 17 degrees. This discrepancy causes the model to underpredict the nose down C_M by up to 0.05 in this region. From 20 degrees until the maximum angle of 24 degrees, the simulation matches the data very well (except for one outlying data point at 24 degrees). The simulation is good as the angle of attack decreases from 24 degrees all the way back to the minimum angle of 3 degrees.

Figures 4.30 through 4.32 represent cases where the mean angle of attack is 20 degrees. For the two lowest values of reduced frequencies (0.025 and 0.051) the simulations err in a similar fashion. They both predict the pitch angle for vortex detachment well but underpredict the magnitude and time duration of the major vortex contribution. Figure 4.30 predicts the vortex reaching the trailing edge three degrees

earlier, with a C_M 0.07 less and full vortex separation 5 degrees earlier than the data indicate. Figure 4.31 predicts the vortex reaching the trailing edge 4 degrees earlier, with a C_M 0.13 less and full vortex separation 5 degrees earlier than the data indicate. One reason for this discrepancy could be that the data are experiencing two very closely spaced vortices in these regions while the model is only predicting the first (lower forced) of these vortices. When the reduced frequency is 0.078 (Figure 4.32) the prediction represents the data better than in the two previous cases. The shape of the curve is off a bit but the maximum and minimum C_M values are almost perfect. The data appear to have two closely spaced vortices which (when combined) are nearly identical in magnitude to the single vortex predicted by the model. The simulation, however, fully separates at 25 degrees but the data continue to have vortex contribution until 28 degrees. The simulation is good as the airfoil pitches from 28 degrees back to its minimum value of 8 degrees.

COMBINED EXPERIMENT ROTOR DATA

COMPARISON RESULTS

This section compares YawDyn C_M output to C_M test data from the Combined Experiment Rotor (CER) wind turbine.

Several data sets were collected for the CER, which was tested at the National Wind Technology Center (NWTC) in Boulder, CO. Each data set is 600 seconds long and contains hundreds of channels of information recorded at a sample rate of 520 Hertz. These data sets were then zero phase distortion low-pass filtered at 13 Hz and decimated by a factor of 17. The resulting files have 30.6 (520/17=30.6) data points per second and no frequencies higher than 13 Hz. This new data file is more manageable and the high frequency "noise" is filtered out. The C_M, angle of attack data (which were both recorded at five different stations along the span of the blade) and wind data were separated from the larger data set. The wind data were used as inputs into YawDyn models of the CER turbine. The output of the YawDyn model contains pitching moment coefficient predictions at span-wise blade locations that correspond with those of the data set. The intent of the model is to accurately predict the pitching moment coefficients.

Three data sets with different mean hub height wind speeds were studied for this research. Data sets 35, 74 and 24 have mean hub height wind speeds of 7.0, 9.0 and 15.1 m/s respectively. The following discussion uses examples from data set 74 (which operates in fixed yaw). Data sets 35 and 24 compare very similarly with their respective

YawDyn simulations. A final simulation comparison from data set 24 is illustrated at the end of this chapter.

Figures 5.1 and 5.2 show angle of attack vs. pitching moment for data set 74 at the 50% and 80% blade stations, respectively, and their corresponding YawDyn simulation. The Beddoes and Leishman model, which is incorporated into this work, predicts C_M fairly well except for the excess scatter in the YawDyn prediction. (Note that the majority of the model's values are in the black region that surrounds the static values. This is also the case for other C_M vs. α plots in this chapter.) When analyzing the pitching moment coefficient vs. time plots (see Figures 5.3 and 5.4) it is obvious that the C_M spikes occur once per revolution. This effect is due to the blade passing through the tower's shadow. The tower shadow is defined in the YawDyn Users Guide (Hansen, 1997). For this model of the CER the tower shadow half-width is 0.4 meters and the deficiency is 25%.

Another observation to note from Figures 5.3 and 5.4 is that the model's C_M spikes are much larger than those in the experimental data. (Also, note that the small spikes in the data are approximately 180 degrees out of phase with the YawDyn predictions. This is a result of the model operating at a perfectly constant speed of 71.9 revolutions per minute while the actual CER runs at a nearly constant rpm that fluctuates between approximately 71.7 and 72.3 rpm. Therefore, the model and the test data are virtually always out of sync.) One possible explanation is that the angle of attack data that comes out of YawDyn, and is used to calculate C_M, is not accurate. However, this is not the case, the angle of attack predictions are reasonable.

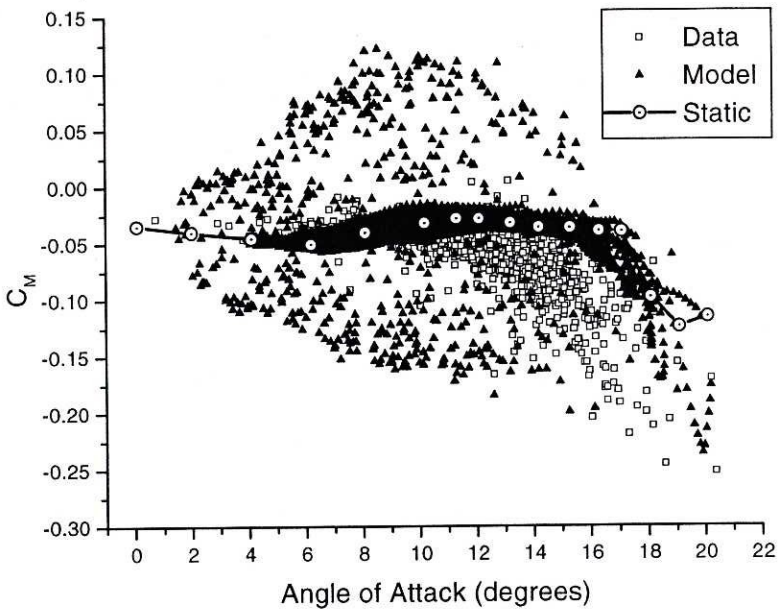

Figure 5.1: Pitching moment coefficient vs. angle of attack at the 50% blade station for the CER data set 74, YawDyn model and static.

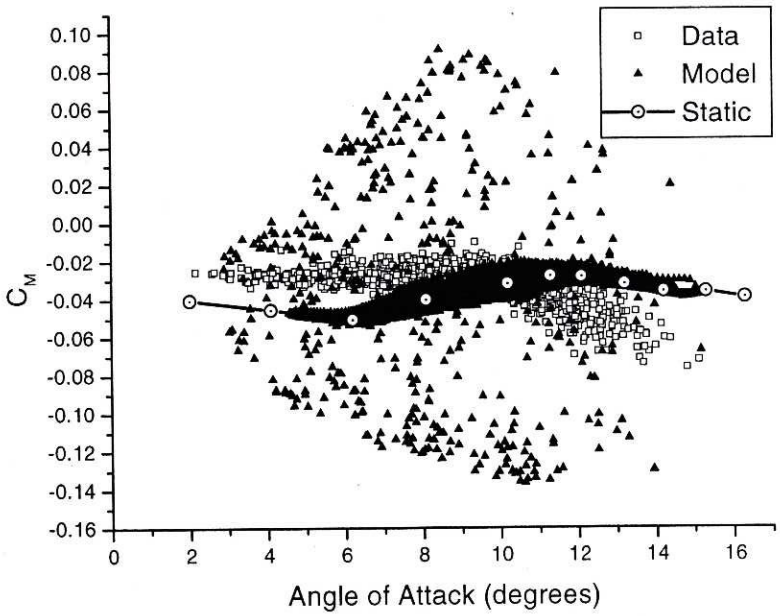

Figure 5.2: Pitching moment coefficient vs. angle of attack at the 80% blade station for the CER data set 74, the YawDyn model and static.

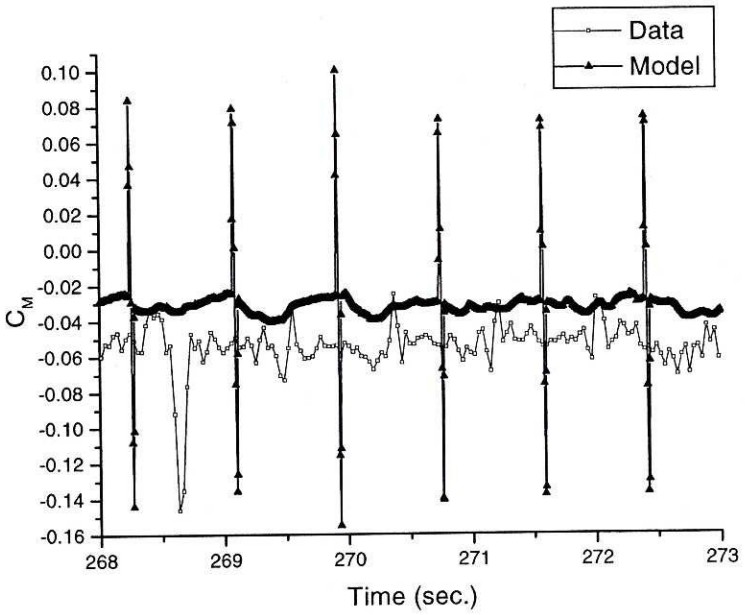

Figure 5.3: Pitching moment coefficient vs. time at the 50% blade station for the CER data set 74 and the YawDyn model.

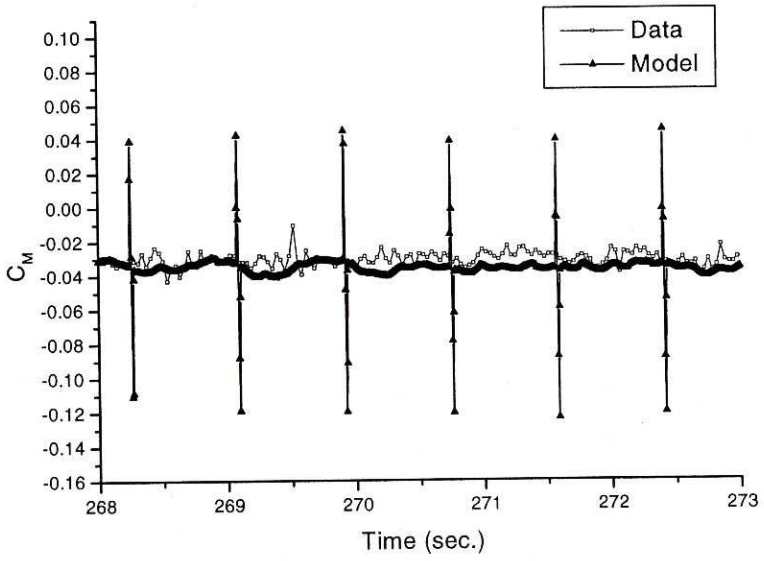

Figure 5.4: Pitching moment coefficient vs. time at the 80% blade station for the CER data set 74 and the YawDyn model.

Figures 5.5 and 5.6 show data and YawDyn model angle of attack vs. time. These figures illustrate the consistency of the tower shadow in the model and its inconsistency in the data. On average, the model reasonably predicts the angle of attack for these situations and others that were analyzed. In fact, when the angle of attack data are used as input into the DynStall program (which was used in a similar way to compare the models to the OSU wind tunnel data) the C_M spikes were still greater in magnitude than those from the test data. This indicates that the model used to calculate C_M does not give satisfactory results when the blade passes through the tower's shadow.

The tower shadow effectively reduces the wind speed by 25% while the rotor continues to spin at a nearly constant 72 +/- 0.3 rpm. Thus, the angle of attack at any given blade location while in the shadow is significantly different than it is outside of the tower's shadow. This is evident from Figures 5.5, 5.6 and Figure 5.7. Figure 5.7 illustrates how local wind speed (which equals the wind speed multiplied by one minus the induction factor) and rotational speed, $R\omega$, combine to form a resultant velocity and angle of attack, α. Since the angle of attack changes so quickly and radically in this region, the values of C_{MI} and C_{MQ} (which come out of the YawDyn model) are greatly magnified due to encountering the tower shadow. (The Methods section of this document explains the dependency that the change in the angle of incidence and the change in pitching rate have on C_{MI} and C_{MQ}, respectively.)

Figure 5.8 is a magnified view of the 50% blade location and illustrates how the four components of pitching moment coefficient (C_{MI} , C_{MQ} , C_{MF} , C_{MV}) respond when encountering the tower's shadow. According to the model, C_{MI} exhibits a very large

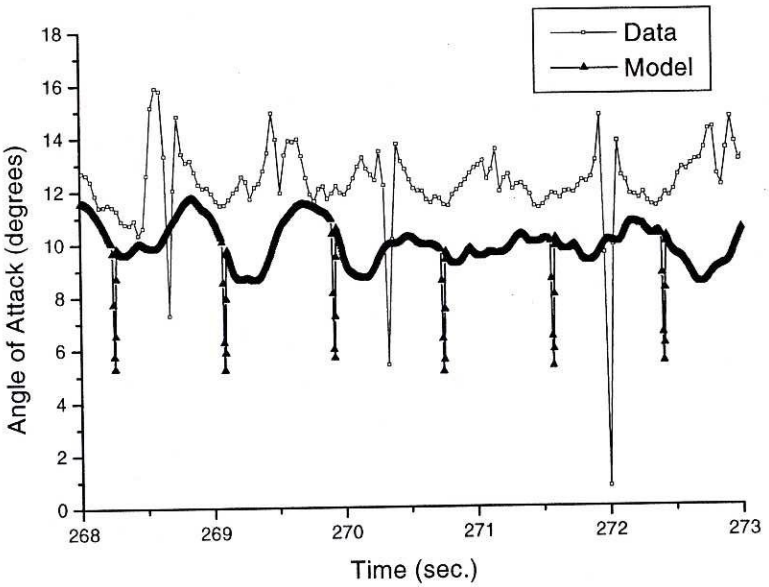

Figure 5.5: Angle of attack vs. time at the 50% blade station for the CER data set 74 and the YawDyn model.

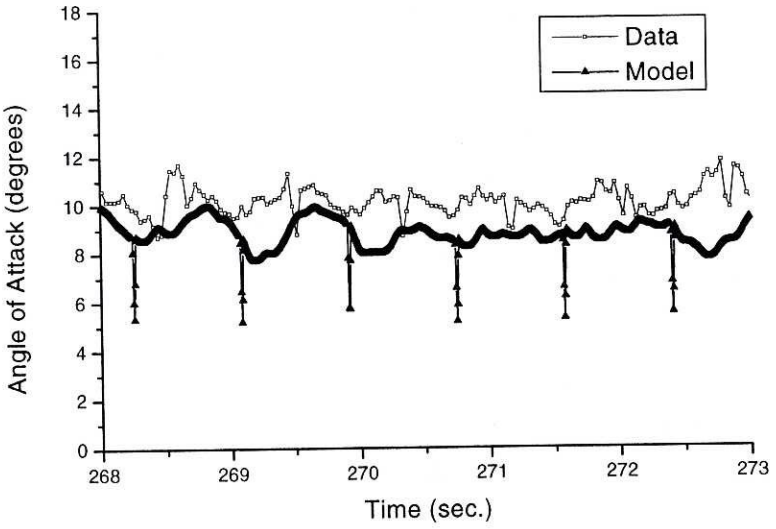

Figure 5.6: Angle of attack vs. time at the 80% blade station for the CER data set 74 and the YawDyn model.

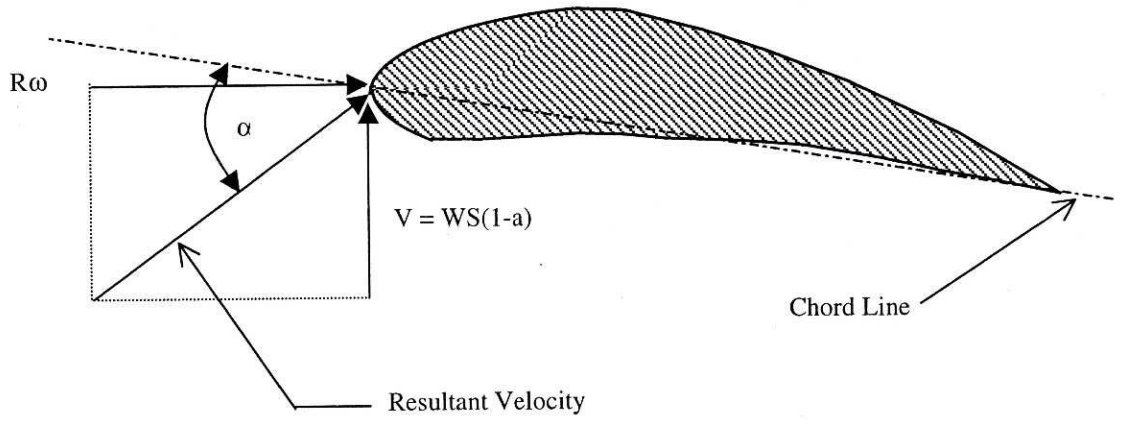

Figure 5.7: Illustration of resultant velocity and angle of attack for an airfoil.

spike. C_{MQ} is also affected but to a lesser extent. C_{MF} is lightly disturbed and since there is no vortex shedding in this angle of attack range, C_{MV} remains constant at zero.

Tyler and Leishman (1991) refer to very fast changes in angle of attack that occur as a result of a sharp increase (or decrease) in the relative wind speed as 'plunge'. They say that modeling plunge is different than modeling 'pitch'. Pitch occurs as an airfoil oscillates (about its spanwise axis) through air that flows at a fairly constant wind speed. The phenomenon of pitch is emulated by the OSU wind tunnel tests and is modeled in the research described in this thesis. It is likely that plunge is occurring as the down wind blade enters and exits the tower's shadow. This may explain why the current model is not accurate in this region.

Devising a model that accurately predicts the phenomenon of plunge is beyond the scope of this research. However, in order to increase the accuracy of the current model, a saturation function was applied to the reduced time rate of change of angle of attack, PRP. This lessens the effects of the tower shadow on the pitching moment coefficient by reducing the magnitude of the spikes exhibited in C_{MI} and C_{MQ}. PRP is defined as:

$$PRP = (d\alpha/dt)\, c/V \tag{15}$$

Figure 5.9 illustrates how the saturation function limits the adjusted value of PRP (referred to as APRP) as PRP exceeds the absolute value of 0.03. The value of APRP is used to calculate an adjusted value of $(d\alpha/dt)$, $(d\alpha/dt)_A$ such that:

$$(d\alpha/dt)_A = APRP\ (V/c) \tag{16}$$

$(d\alpha/dt)_A$ is used instead of $(d\alpha/dt)$ in the equations needed to calculate C_{MI} and C_{MQ}.

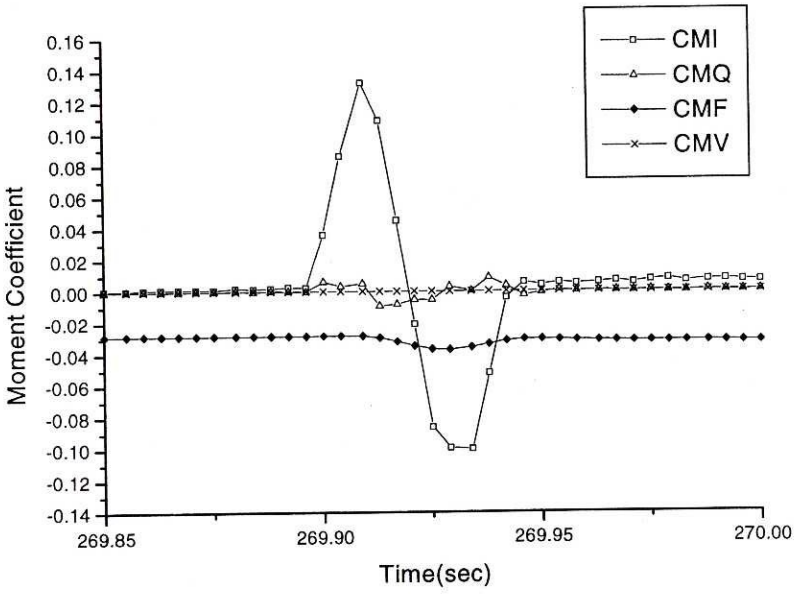

Figure 5.8: The reaction of the four components of the pitching moment coefficient when encountering the tower's shadow.

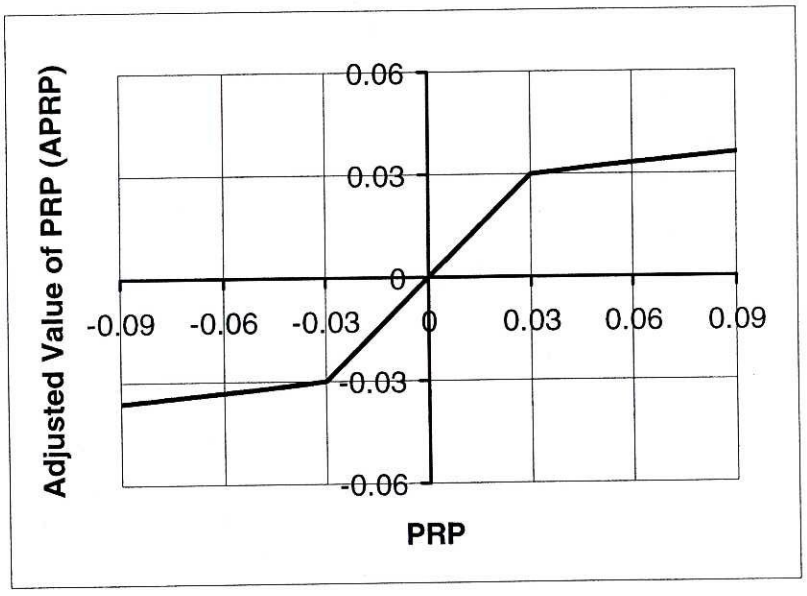

Figure 5.9: The reduced time rate of change of angle of attack, PRP vs. the adjusted value, APRP.

A value of 0.03 was chosen as the point where the saturation function is engaged because this value has virtually no effect on the model for predicting OSU wind tunnel test data and moreover, it predicts the CER test data with greater accuracy.

Figure 5.10 illustrates the reduction of the C_{MI} and C_{MQ} spikes as a result of the introduction of the saturation function. Figures 5.11 and 5.12 show similar taming of the pitching moment coefficient, C_M. The C_M spikes in this figure are up to 0.1 less than the model without the saturation function. Figure 5.13 and 5.14 show the same data as Figure 5.1 and 5.2 and are now being compared to a YawDyn model that employs the aforementioned saturation function.

Figure 5.15 also illustrates that the model predicts the data accurately for data set 24 (which has a mean wind speed of 15.1 m/s and operates in free yaw).

Conclusion

While the model prediction is much better than it was previously, the model still over predicts the scatter of the C_M in most cases. This leads to greater pitching moment coefficients than the data suggests. However, a conservative model is adequate for this research since the purpose is to investigate if pitching moments are significant enough to effect parameters such as angle of attack, lift, drag, power output, and flap moments. If a conservative model (such as the one presented here) has a negligible effect on these parameters, then it can be postulated that pitching moments are not needed in wind turbine models. On the other hand, if pitching moments are shown to be significant in predicting any of the aforementioned parameters then future research can be devoted to devising a more accurate model.

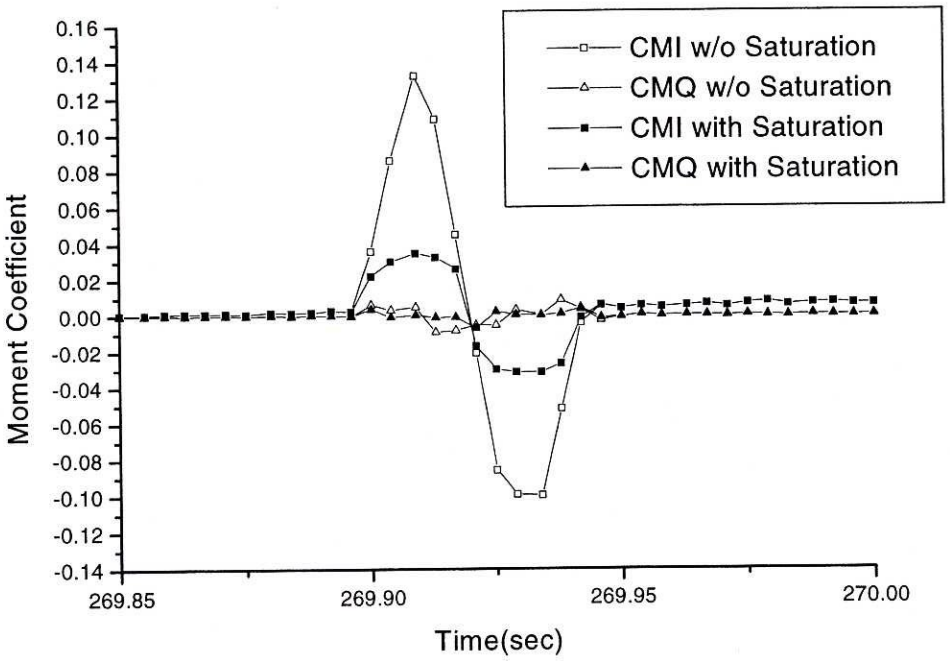

Figure 5.10: C_{MI} and C_{MQ} without and with the saturation function.

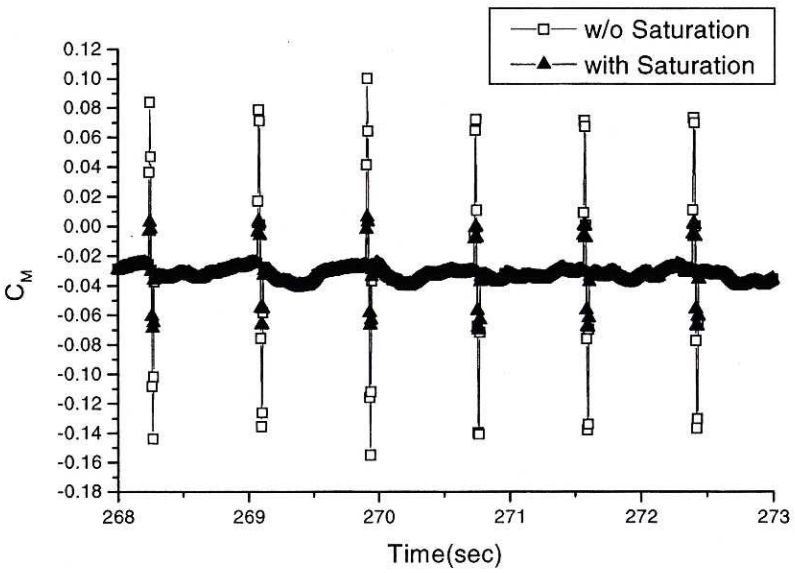

Figure 5.11: Pitching moment coefficient vs. time at the 50% blade station without and with the saturation function.

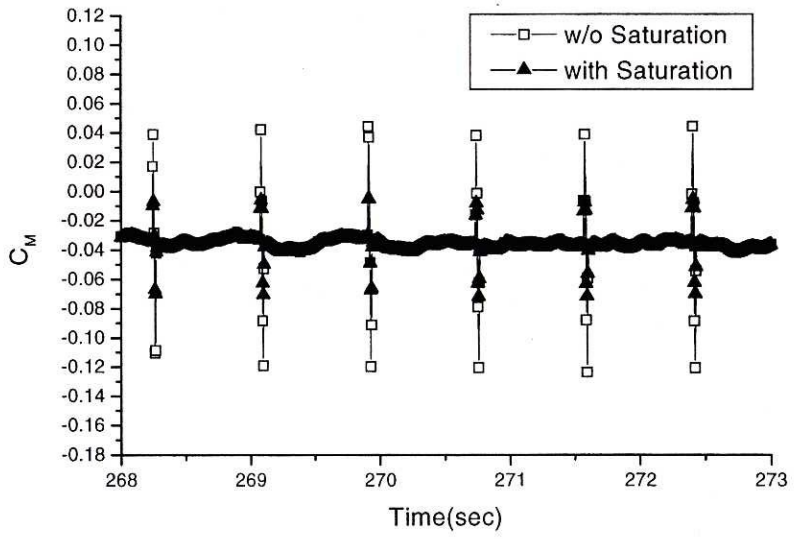

Figure 5.12: Pitching moment coefficient vs. time at the 80% blade station without and with the saturation function.

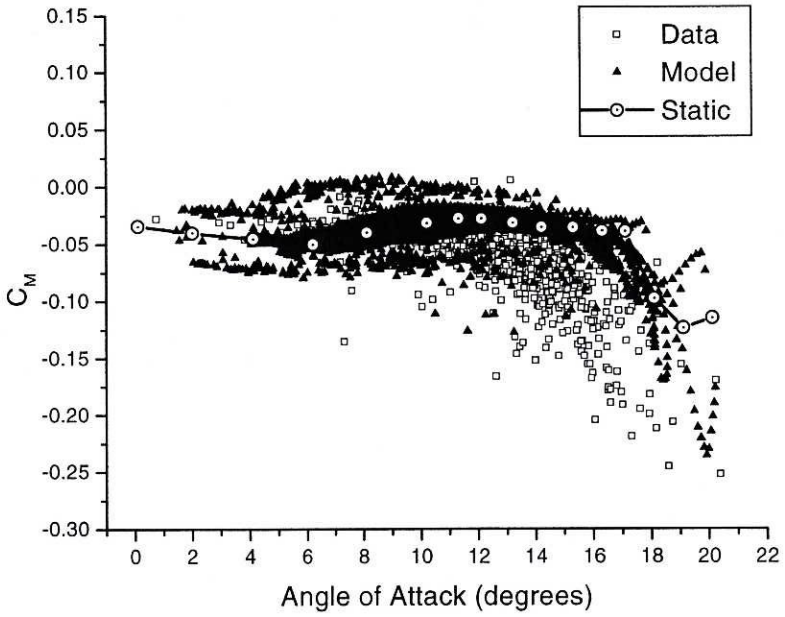

Figure 5.13: Pitching moment coefficient vs. angle of attack at the 50% blade station for the CER data set 74, YawDyn model (with saturation function) and static.

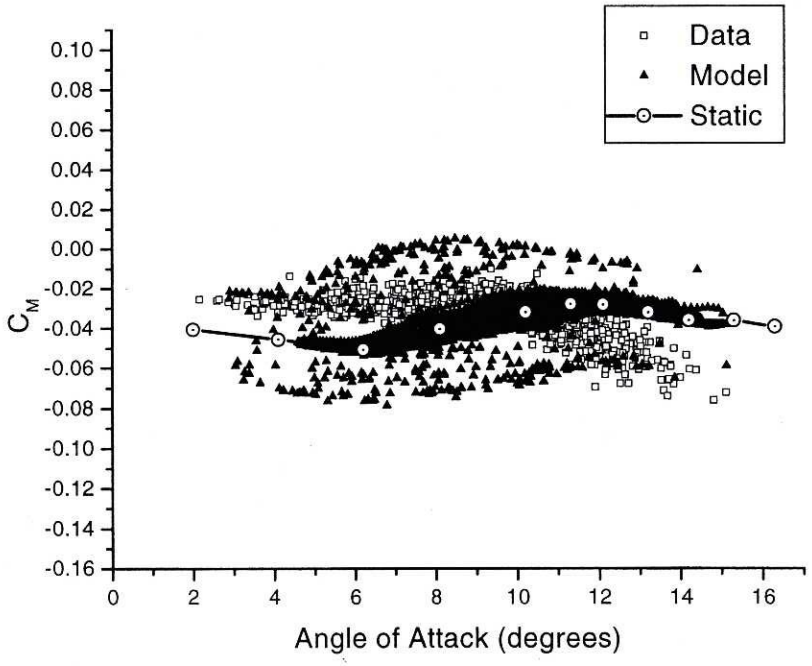

Figure 5.14: Pitching moment coefficient vs. angle of attack at the 80% blade station for the CER data set 74, YawDyn model (with saturation function) and static.

CONCLUSION

The goals of this research have been accomplished. Dynamic pitching moments were added to the AeroDyn subroutines, which are part of the ADAMS, YawDyn and DynStall computer models. The AeroDyn subroutines calculate aerodynamic forces that are present on wind turbine blades. The AeroDyn subroutines, which incorporate the Beddoes-Leishman model for unsteady aerodynamics and dynamic stall, were able to successfully predict dynamic pitching moment coefficient values for conditions that occur with wind turbine blades. However, in order to increase the accuracy of the model, some changes were made to the Beddoes-Leishman methods including the following:

1. The static separation point, f, was calculated from equation 9 instead of the empirical equation used by Beddoes and Leishman. This allows for representation of separation point values throughout the entire 360 degree range of angles of attack.
2. An approximate value of the dynamic angle of attack, α'', was calculated from equation 13. It was then used to retrieve the corresponding C_{MF} from a "look-up table." Beddoes and Leishman recommend using a polynomial relationship (which is a function of f'' and C_N). However, this method only works for a small range of angles of attack.
3. A saturation function was added to the model to control the values of C_{MI} and C_{MQ} when the blades were encountering a sudden change in pitch and pitch

rate (such as in the vicinity of the tower's shadow). Without the saturation function, C_{MI} would display large spikes under this circumstance.

The resulting model was able to predict dynamic C_M values recorded during 2-D wind tunnel experiments at OSU for three different airfoils at Reynold's numbers of 1.0 and 1.5 million at reduced frequencies up to 0.09. The model also predicted C_M data that were gathered during field tests on the CER wind turbine at NREL's NWTC.

Finally, an ADAMS model of the CER was run with a pitching hinge at each of the blade roots. The stiffness of the hinge was varied in order to see how sensitive it was to the blade's pitching motion. Results indicated that in light (e.g., 12m/s), steady winds the pitching natural frequency of the blades needs to be very soft (near 1 p) in order for the pitching moment to play a significant role in causing torsional blade motion. However, as the wind becomes stronger (e.g., 20m/s average wind speed) and turbulent, a blade with a 7.5 p pitching frequency is noticeably influenced by the inclusion of the pitching moment data. Pitching moments affect the angle of attack, pitch angle, power and root flap moment of a blade. Therefore, it is important to consider the contributions of pitching moments when similar conditions exist. It is also important (even with stiff blades) to include pitching moments in the aerodynamic calculations if the blade has a sloppy pitch control system, therefore allowing the blade to easily pitch at its root. When this situation occurs, even a small pitching moment can pitch the blade a significant amount.

Topics for Future Work

More work can be done on the pitching moment calculations to increase their accuracy and reliability, including the following:

1. Test more airfoils.
2. Revisit the time constant values for a larger number of airfoils and 2-D test data at higher reduced frequencies.
3. Replace the saturation function with the ability of the model to incorporate the effects of plunge.
4. When wind tunnel data on the CER wind turbine becomes available, compare simulations to this data.

This research would add further to the reliability of the dynamic pitching moment calculation.

REFERENCES

Ancona, D.F., Goldman, P.R. and Thresher, R.W., 1996, "Wind Program Technological Developments in the United States," World Renewable Energy Congress, Denver, CO.

AWEA, 1996, news release from AWEA, August 14, 1996.

Batchelor, G.K., 1988, *An Introduction to Fluid Dynamics*, Cambridge University Press, New York, NY, p.350.

Cadogan, J.B., Parsons, B., Cohen, J.M. and Johnson, B.L., 1996, "Characterization of Wind Technology Progress," NREL in-house report.

Carr, W.L., 1988 "Progress in the Analysis and Prediction of Dynamic Stall," *Journal of Aircraft*, Vol. 25, No. 1, pp. 6-17.

Gipe, Paul, 1995, *Wind Energy Comes of Age*, John Wiley and Sons, Inc., New York, NY, pp. 9-33.

Gregorek, G.M. and Reuss, R.L., 1994, personal communication and computer data files.

Hansen, A.C., 1997, "User's Guide to the Wind Turbine Dynamics Computer Programs YawDyn and AeroDyn for ADAMS," NREL document XAF-4-14076-02.

Leishman, J.G. and Beddoes, T.S., 1986, "A Generalized Model For Airfoil Unsteady Behavior and Dynamic Stall Using the Indicial Method," *Proceedings of the 42nd Annual Forum of the American Helicopter Society*, Washington, D.C., pp. 243-266.

Leishman, J.G. and Beddoes, T.S., 1989, "A Semi-Empirical Model for Dynamic Stall," *Journal of the American Helicopter Society*, Vol. 34, No. 3, pp. 3-17.

Leishman, J.G., 1988, "Validation of Approximate Indicial Aerodynamic Functions for Two-Dimensional Subsonic Flow," *Journal of Aircraft*, Vol.25, No. 10, pp. 914-922.

Leishman, J.G., 1989, "Modeling Sweep Effects on Dynamic Stall," *Journal of the American Helicopter Society*, Vol.34, No. 3, pp. 18-29.

McCroskey, W.J., 1981, “The Phenomenon of Dynamic Stall,” NASA Technical Memorandum, TM81264.

Pierce, K. and Hansen A.C., 1995, “Prediction of Wind Turbine Rotor Loads Using the Beddoes-Leishman Model for Dynamic Stall,” *Journal of Solar Energy Engineering*, Vol. 117, pp.200-204.

Pierce, K., 1996, *Wind Turbine Load Prediction Using the Beddoes-Leishman Model for Unsteady Aerodynamics and Dynamic Stall*, Master’s of Science Thesis, Department of Mechanical Engineering, University of Utah Department of Mechanical Engineering, Salt Lake City, UT.

Quarton, D.C., 1996, “Calculation of Wind Turbine Aeroelastic Behaviour - The Garrad Hassan Approach,” IEA Experts Meeting, April 1996, Technical University of Denmark, pp. 3-12.

San Martin, R.L., 1989, “Environmental Emissions from Energy Technology Systems: The Total Fuel Cycle,” U.S. Department of Energy, Washington D.C.

Spera, David, 1994, *Wind Turbine Technology Fundamental Concepts of Wind Turbine Engineering*, ASME Press, New York, NY, pp. 33-38.

Stoddard, F.S. and Nelson, V.C., 1988, “Causes and Effects of Live Aeroelastic Twist of Wind Turbine Blades,” *Wind Power ’88 Proceedings*, pp. 223-233.

Thresher, R.W., Hock, S.M., Dodd, H.M. and Cohen, J.M., 1994, “Advanced Technology for the Year 2000: Utility Applications,” NREL in-house report, Golden, CO.

Thwaits, B., 1960, *Incompressible Aerodynamics*, Oxford University Press, New York, NY, pp. 168-170.

Tyler, J.C. and Leishman, J.G., 1991, “An Analysis of Pitch and Plunge Effects on Unsteady Airfoil Behavior,” Presented at the 47th Annual Forum of the American Helicopter Society, Phoenix, AZ.

Wilson, R.E., Freeman, L.N., Walker, S.N. and Harman, C.R., 1996, “Final Report of the FAST Advanced Dynamics Code,” Department of Mechanical Engineering, Oregon State University, Corvallis, OR.